University of Vermont
ScholarWorks @ UVM

7-26-2012

Electromagnetic Precursors in Complex Layered Media

Christopher Palombini
University of Vermont

Follow this and additional works at: http://scholarworks.uvm.edu/graddis

ELECTROMAGNETIC PRECURSORS IN COMPLEX LAYERED MEDIA

A Dissertation Presented

by

Christopher L. Palombini

to

The Faculty of the Graduate College

of

The University of Vermont

In Partial Fullfillment of the Requirements
for the Degree of Doctor of Philosophy
Specializing in Electrical Engineering

October, 2012

Abstract

The dynamical evolution of an ultrawideband electromagnetic pulse as it propagates through a temporally dispersive and attenuative medium is a classical problem in electromagnetic wave theory with considerable practical importance dating back to seminal works conducted in 1914. With the use of modern asymptotic theory and numerical techniques, propagation of canonical pulses into complex (attenuative and dispersive) media have been analyzed and recently extended to nonlinear materials. The materials of interest for this research are modeled after realistic biological tissues. The mathematically rigorous and more accurate physical model of electromagnetic energy transfer into the biological materials modeled will be used as input to the FitzHugh-Nagumo circuit equivalent model for an excitable neuron. This detailed analysis will provide a new point of view to working groups and standardization committees in the field of non-ionizing radiation safety that is based on so-called athermal effects.

Acknowledgements

I never would have been able to finish my dissertation without the continued support of my family and friends. I would like to express my deepest gratitude to my advisor, Dr. Kurt E. Ouhgstun, for his ineffable guidance and patience throughout this research, and to the rest of my committee members, in particular Dr. Jeff Frolik. Finally, I would like to thank my brother, Chip, while his support at times can best be described as *unconventional* it has been, and always will be, a necessary component of all my professional endeavors.

Table of Contents

List of Tables

List of Figures

Notation

Notation	Description
$x(t)$	Scalar time domain
$x\left(\mathbf{r}, t\right)$	Scalar space-time domain
$\mathbf{x}(t)$	Vector time domain
$\mathbf{x}\left(\mathbf{r}, t\right)$	Vector space-time domain
$\hat{\mathbf{n}}$	Unit vector
$\tilde{x}(\omega)$	Temporal Fourier transform of scalar
$\tilde{\tilde{x}}(\mathbf{k}, \omega)$	Spatio-Temporal Fourier transform of scalar
$\tilde{\mathbf{x}}(\omega)$	Temporal Fourier transform of vector
$\tilde{\tilde{\mathbf{x}}}(\mathbf{k}, \omega)$	Spatio-Temporal Fourier transform of vector
$\hat{x}(t)$	Time domain representation of frequency domain function
$\Re\{\cdot\}$	Real component of complex function
$\Im\{\cdot\}$	Imaginary component of complex function

Table 1: Commonly used notation.

Chapter 1

Introduction

1.1 Motivation

Researches have been actively interested in the interactions of electromagnetic fields and biological tissues for some time. The original discovery of X-rays in the late 1800's (Röntgen 1895) and their applications to diagnostic radiology revolutionized medicine. However, this *new kind of ray* that Röntegen had discovered is now known to be ionizing and has since been shown to cause damage to living tissues. Exposure limits to ionizing radiation such as Röntegen's X-rays have been established by the United States Department of Labor under Occupational Safety and Health Administration (OSHA) standard 1910.1096 for general industry. However, OSHA does not have specific standards for non-ionizing radiation for the regions of the electromagnetic spectrum including radiofrequency and microwave radiation but does acknowledge that research is ongoing.

The interactions of non-ionizing radiation with biological tissues are of large concern today and much is to be studied about the athermal, anything but heating, effects of such interactions. It is largely believed that non-ionizing radiation is harmless below exposures were heating occurs (Adair 2003) but the research provided assumes a continuous, monochromatic signal with no mention of transient phenomena or pulsed fields associated with radar and mobile communications. Pulsed fields and transient phenomena are of

central importance to biological response to applied fields since action potential threshold response is dependent on the rate of rise of the applied voltage (Cole 1955) and it has been shown that exposure to stimuli can cause (Carpenter, Sage, et al. 2007):

1. Direct molecular effects

   - DNA damage

   - Membrane perturbations

   - Protein function alterations

2. Indirect molecular effects

   - Cell signal transduction

   - Gene expression

3. Phenotypic effects

   - Cell apoptosis

   - Cell cycle perturbation

   - DNA repair

   - Differentiation and development

   - Carcinogenesis

   - Growth

This dissertation examines membrane perturbations leading to membrane breakdown, and cell signal transduction. A neuron is an example of an excitable cell that creates an *action potential* when its membrane voltage is perturbed beyond a threshold, as discussed in chapter 4. These action potentials are a voltage signal that propagates down an axon allowing the cell to communicate with other neurons.

The current limits for non-ionizing radiation are set by the IEEE C95.1 Standard for Safety Levels With Respect to Human Exposure to Radio Frequency Electromagnetic Fields,

3kHz to 300GHz and are illustrated in Fig. 1.1. This standard is based solely on the thermal
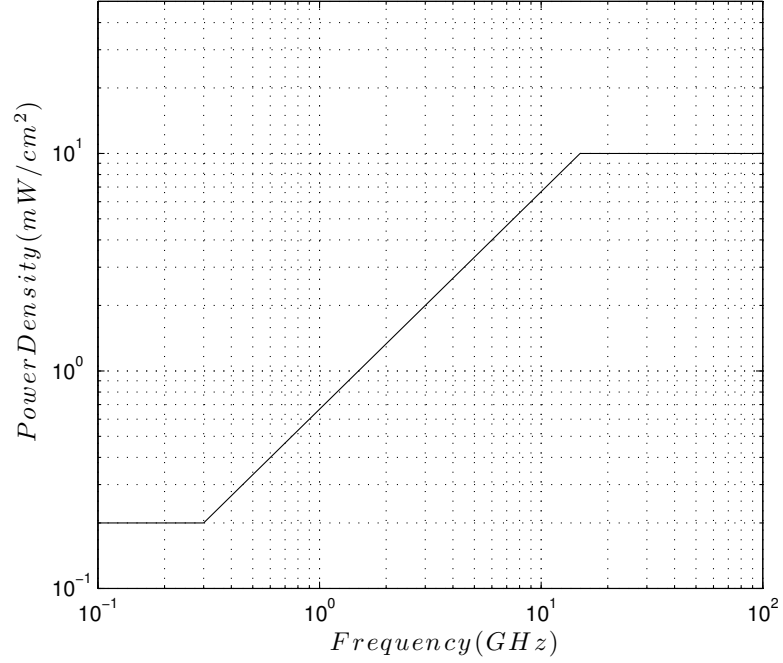
Figure 1.1: IEEE C95.1 standard for non-ionizing radiation.

interactions provided by specific absorption rates (SAR) defined as

$$SAR = \frac{\sigma}{\varrho}|E_{RMS}|^2 \text{ W/kg,} \tag{1.1}$$

where σ is the conductivity of the tissue, ϱ is the mass density and E_{RMS} is the root mean square value of the electric field. The specific absorption rate expresses how much power is absorbed by the tissue in Watts/kg. For frequencies up to 10GHz field strengths of 1W/cm^2 for 100 seconds will burn the skin. However, as frequencies are increased more energy is absorbed closer to the surface, resulting in skin burns from a power density of only 200mW/cm^2 for 100 seconds, for frequencies in the tens of gigahertz (Taylor and Giri 1994).

Far from being a theoretical concept Brillouin precursors are being utilized in recent ultrawideband imaging technologies and in USAF research on improved airborne surveillance (Slesin 2002c). Despite evidence for the existence of Brillouin precursors being of

3

biological significance, however, they were rejected for consideration by the IEEE's standard setting committee. The committee's reason was because there was no "evidence in the peer-reviewed scientific literature supporting Brillouin precursors as being biologically important at radio frequencies" (Slesin 2002b). Physicist Robert Adair went further in claiming that Brillouin precursors were far too weak to ever effect biology and that Albanese and Oughstun were practicing voodoo science. Adair also stated that the claims of possible hazards from Brillouin precursors were "damaging to the Air Force and in its role in defense of the United States – *my* country – and *my* Air Force" (Slesin 2002a). Independent research (Maisch 2010) has concluded

> It can be argued that on one level Adair is correct about the danger posed
> by work of Albanese and Oughstun on Brillouin Precursors. If their alleged
> bioeffect on the human body was established by further research/replication
> studies and peer reviewed publishing it would invalidate the whole concept of
> safety through SAR calculations that lay at the foundations of both IEEE C95.1
> and International Commission on Non-Ionizing Radiation Protection (ICNIRP).

Additionally, since Brillouin precursors carry energy further into dispersive materials and would provide pulses for biological imaging as well as therapy.

In a January 11, 2001, letter from Senator Edward M. Kennedy to the Secretary of the Air Force, F. Whitten Peters, Kennedy asked that the Air Force fund an independent study through the National Research Council of the National Academies "to examine the health effects of the PAVE PAWS system." This recent study (Barnes 2005) conducted by The National Research Council of the National Academies was requested by Senator Edward Kennedy and has explored possible health effects of exposure to PAVE PAWS (Precision Acquisition Vehicle Entry Phased Array Warning System) a low-level phased-array radio frequency energy radar system located at Cape Cod Air Force Station in Cape Cod, Massachusetts. The report describes physical mechanisms for radiofrequency effects on biological systems and begins with noting the depth of penetration into typical biological

4

materials being 3-4 cm but up to 16 cm in bone at 433MHz. What the report fail to mention is the reflection coefficients for these materials and the possible biological significance of precursor fields. However, the committee did acknowledge that precursors can be formed at radio and microwave frequencies in water, a large component of biological tissues.

The newly completed ten year INTERPHONE study (Cardis, Deltour, Vrijheid, Combalot, Moissonnier, Tardy, Armstrong, Giles, Brown, Siemiatycki, et al. 2010) shows that there is an increased risk of malignant tumors in the tissues of the nervous system by 40% with 1640 hours or more of use on the side of the head used most for communications with mobile devices. The report concludes

> Overall, no increase in risk of glioma or meningioma was observed with use of mobile phones. There were suggestions of an increased risk of glioma at the highest exposure levels, but biases and error prevent a causal interpretation. The possible effects of long-term heavy use of mobile phones require further investigation.

this succinct communication further stresses the necessity for additional research.

In contrast to this longterm study a separate experimental trial (Volkow, Tomasi, Wang, Vaska, Fowler, Telang, Alexoff, Logan, and Wong 2011) was conducted in which the glucose metabolism of the brain in 47 healthy participants was monitored while a cell phone was either in the on or off state. The subjects of the study were placed in a fMRI (functional magnetic resonance imaging), which was used to measure glucose metabolism throughout the brain. Glucose metabolism is an indication of neuron activity as the cells requires the energy provided by the glucose to pump ions across their membranes. Additionally, the subjects in the study did not know if the mobile communication device was in the on or off state. Their results

> Whole-brain metabolism did not differ between on and off conditions. In contrast, metabolism in the region closest to the antenna (orbitofrontal cortex and temporal pole) was significantly higher for on than off conditions (35.7 vs

$33.3 \mu mol/100$ g per minute; mean difference, 2.4 [95% confidence interval, $0.67-$ 4.2]; $P = .004$). The increases were significantly correlated with the estimated electromagnetic field amplitudes both for absolute metabolism ($R = 0.95, P < .001$) and normalized metabolism ($R = 0.89; P < .001$).

show statistical evidence that there is an intimate coupling between between radio frequency fields transmitted by mobile communication devices operating inside current FCC standards and human physiology.

1.2 Historical Overview

1.2.1 Quantitative Physiology

The earliest experiments and theory on the role of electricity in biological systems were the works of Luigi Galvani who stimulated the muscle in frog legs with electricity. The experimental setup is shown in Fig. 1.2. His first successful forced contraction of the frog leg occurred when he touched the nerve with a pair of scissors during a lightning storm in 1786. Galvani reassured himself that electricity was responsible for these muscular contractions by repeated experimentation and eventually published his findings in 1791 as *De viribus electricitatis in motu musculari commentarius* ("Commentary on the Force of Electricity on Muscular Motion").

Hodgkin and Huxley, along with others, generated a series of papers (Hodgkin, Huxley, and Katz 1952; Hodgkin and Huxley 1952d; Hodgkin and Huxley 1952a; Hodgkin and Huxley 1952c; Hodgkin and Huxley 1952b) from their empirical studies of the giant squid axon for which they received the 1963 Noble Prize in Physiology or Medicine. This well known work was instigated by theoretical work (Bernstein and Tschermak 1906) that was presented almost half a century earlier. With the understanding that the cellular membrane created ion gradients across its barrier and with the knowledge that the potassium concentration inside the cell was relatively higher than in the extracellular fluid, Bernstein
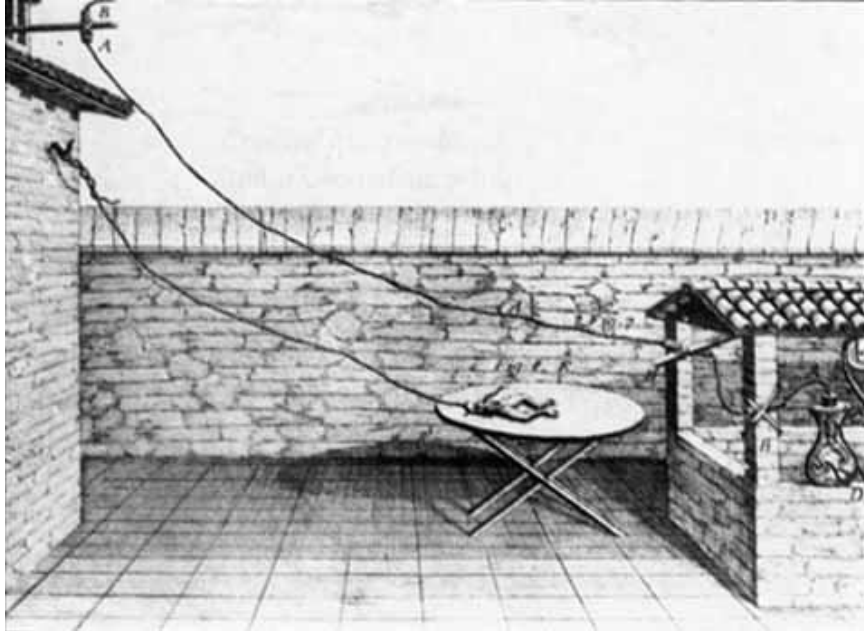
Figure 1.2: Galvani's frog leg experiment.

was able to theoretically predict that the resting membrane potential of a cell would be around $-70mV$ using Nernst's theory. Bernstein also knew that during active cellular communications, potassium concentrations approached equilibrium. He assumed this was true because of some form of breakdown in the cellular membrane, increasing permeability to all ion species and hypothesized that the membrane voltage would tend to 0.

It was not until over 30 years later that the membrane potential was directly measured (Curtis and Cole 1940). Not only did the membrane potential approach 0 during the generation of an action potential but there was a significant transient overshoot in which the membrane became hyperpolarized. This overshoot could not be explained by Berstein's hypothesis together with qualitative reasoning for the changes in the permeability of the cellular membrane. Electrodes for measuring transient behavior in the squid giant axon saw incredible improvement during this time period along with the development of the *space clamp technique* (Marmont 1949). In this procedure, Marmont was able to virtually eliminate longitudinal resistance of the axoplasm by threading a silver wire in the interior of the axon, effectively shorting the internal resistance. The result of this is that a patch of

the axon was at a potential equilibrium, thereby allowing for an uncorrupted measurement of the axial membrane current.

Based upon their own experimental works, Hodgkin and Huxley then formulated an analytical description of the membrane potential

$$C_m \frac{dV}{dt} = -g_{Na}(V - V_{Na}) - g_K(V - V_K) - g_K(V - V_L) + I_{app}. \tag{1.2}$$

Here C_m is the membrane capacitance, g_{Na} is the sodium conductance, V is the transmembrane potential, V_{Na} is the potential due to sodium, g_K is the potassium conductance, V_K is the potential due to potassium, g_L is the leakage conductance, V_L is the potential due to leakage, and I_{app} is the externally applied current. The conductances can be summed to form an effective conductance as $g_{eff} = g_{Na} + g_K + g_K$ and by taking the inverse of this quantity the time constant for the parallel RC circuit representing the membrane is given by $\tau_m = C_m R_m$ (Keener and Sneyd 1998).

In order to determine the complex dynamics of these species specific conductances Hodgkin and Huxley employed the the *voltage clamp technique*. This clamp imposes a new biased transmembrane voltage on the cell in a step like fashion and measures the transmembrane current being supplied that is necessary to keep the voltage offset. This new empirical data created a new hypothesis and about the kinetics of the ionic currents. From these data Hodgkin and Huxley were able to determine the analytical forms of conductances and the behavior of their associated ion gates.

The Hodgkin-Huxley model for action potential propagation is quite complex and was reduced from a four dimensional phase space to a two dimensional phase space (Fitzhugh 1960; Fitzhugh 1961; Fitzhugh 1969). The slow variable, the membrane voltage, has a linearly increasing nullcline in the fast-slow phase plane while the fast variable, the capacitor current, is nonlinear with a cubic shape. Shortly after FitzHugh published his work Nagumo, an electrical engineer from Japan, built the circuit (Nagumo, Arimoto, and Yoshizawa 1962) shown in Fig. 1.3 that FitzHugh had quantitatively described. This model is now known as the FitzHugh-Nagumo model. The circuit consists of capacitor C_m, a nonlinear current-

voltage element $F(V)$ represented by a tunnel diode, a passive resistance R, inductor L and battery V_0. With the use of Kirchhoff's circuit laws the circuit is completely described as

$$C_m \frac{dV}{dt} + F(V) + i = -I_0, \tag{1.3}$$

$$L\frac{di}{dt} + Ri = V - V_0, \tag{1.4}$$

where Nagumo used $C_m = 0.01\mu$F, $L = 4$mH, $V_0 = 100$mV, and R=500Ω.
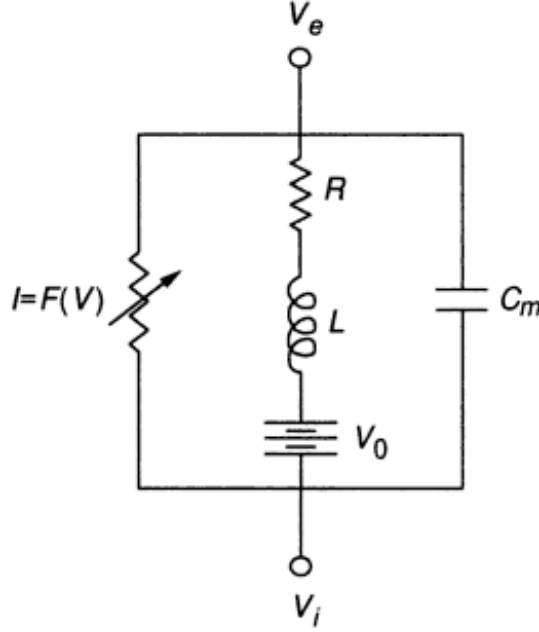
Figure 1.3: Nagumo circuit for an excitable neuron.

1.2.2 Electromagnetics

The dynamical evolution of an ultrawideband, that is the rise or fall time of the pulse exceeds the relaxation time of the media, electromagnetic pulse as it propagates through a temporally dispersive and attenuative medium is a classical problem (Sommerfeld 1914; Brillouin 1914; Brillouin 1960; Stratton 1941; Jackson 1999; Oughstun and Sherman 1994; Oughstun 2006a; Oughstun 2009a) in electromagnetic wave theory with considerable practical importance (Bertoni, Carin, and Felsen 1993; Carin and Felsen 1995; Baum, Carin, and Stone 1997; Heyman, Mandelbaum, and Shiloh 1999; Smith and Cloude 2002; Mokole,

Kragalott, and Gerlach 2003), most recently being applied to airborne surveillance and ground penetrating radar (Slesin 2002c), with seminal work conducted in 1914. These initial works due to Brillouin and Sommerfeld showed the evolution of forerunners or precursor fields. This early work has been expanded on with modern asymptotic and numerical techniques due to Oughstun and Sherman (Oughstun and Sherman 1989; Oughstun and Sherman 1990; Oughstun 1991; Oughstun and Sherman 1994; Oughstun and Sherman 1988). The more recent description of the propagated field has corrected erroneous conclusions of Brillouin and Sommerfeld that the amplitudes of these precursor fields are negligible in comparison to the main signal component of the field. The plot in Fig. 1.4 shows an input ultrawideband pulse Heaviside step function sine wave. The pulse was propagated
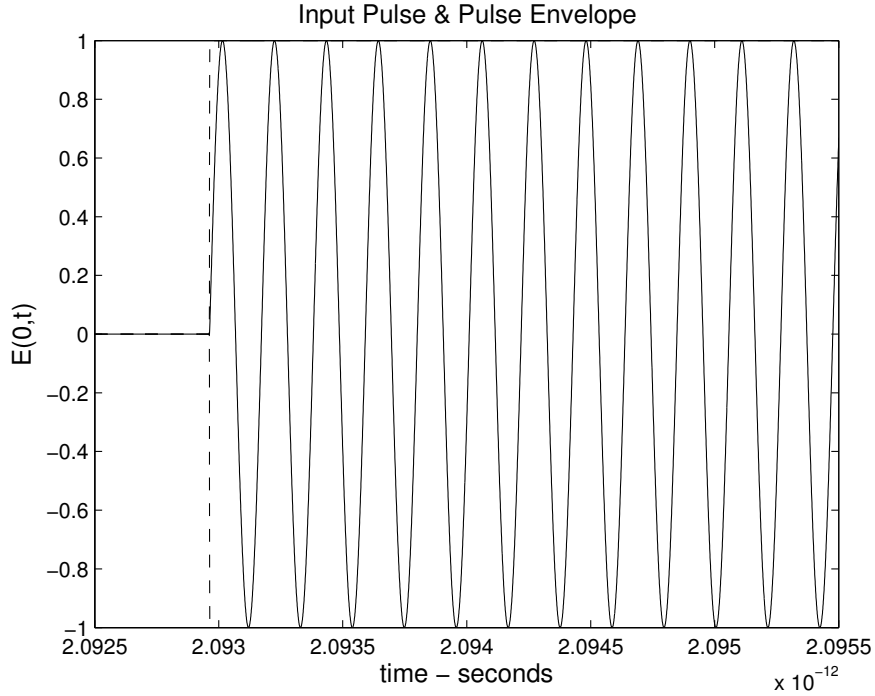
Figure 1.4: Step function (dashed) modulated pulse of $f(t) = \sin(\omega_c t)$ (solid) with $\omega_c = 3 \times 10^{16}$r/s with turn on time equal to 10% of the carrier frequency period.

through a single resonance Lorentz model dielectric with model parameters $\omega_0 = 4 \times 10^{15}$r/s, $\delta_0 = 0.28 \times 10^{16}$r/s,$b_0 = \sqrt{20} \times 10^{16}$r/s which were the values chosen by Brillouin (Brillouin 1914; Brillouin 1960). The propagated pulse, Fig. 1.5, shows the formation of both a Som-

10

merfeld and Brillouin precursor field as well as the absence of the steady state signal. These precursor fields are characteristic of the lossy, dispersive medium that the pulse propagates through, with the input pulse providing the requisite energy for their formation.
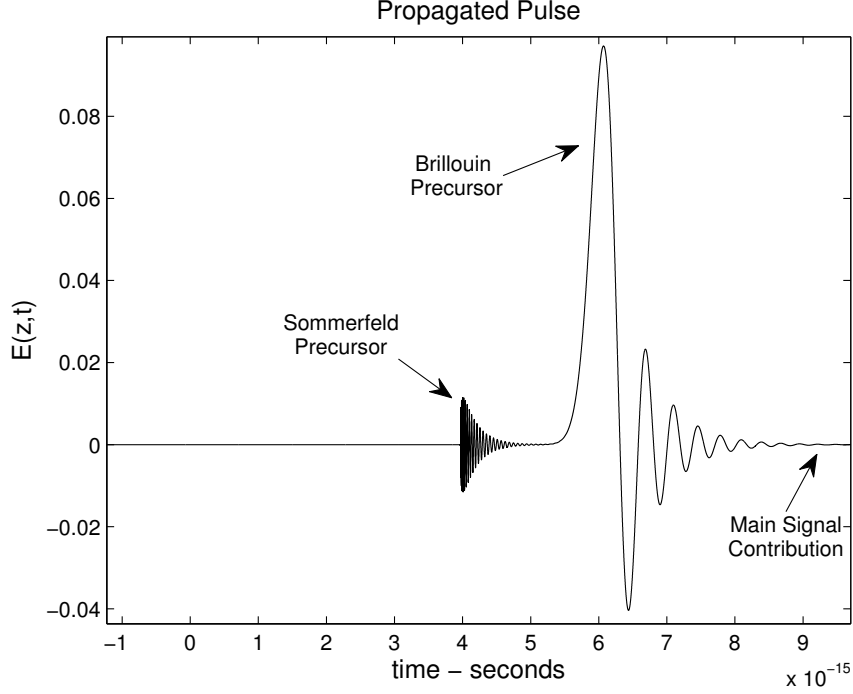
Figure 1.5: Propagated field structure at $z = 20z_d \sim 1.19\mu m$ showing both Sommerfeld and Brillouin precursor fields as well as the absence of the main signal.

In a medium that is nondispersive all spectral components of the input field would propagate at the same phase velocity and attenuate at the same rate, that is the shape of the field would be unaltered as it moved through this nondispersive medium only decaying in amplitude. However, in a causal, dispersive medium each spectral component is absorbed at its own rate increasing with distance into the material so that the relative energy of each spectral component changes with propagation distance. Additionally, each monochromatic component of this initial pulse propagates through the medium with its own phase velocity causing a change in the phasal relation of each of the monochromatic spectral components. It is these two simple, physical and necessary effects that dynamically modify the input field as it propagates through a dispersive medium. These two effects are not independent

11

but rather coupled in a very intimate manner by the requirement of causality (Toll 1956; Nussenzveig 1972). When the initial pulse incident on the medium is sufficiently wideband, that is has a sufficiently rapid rise-time, fall-time or amplitude change, these physical traits of the dispersive, attenuative medium are manifested into the formation of these precursor fields with the initial pulse providing the requisite energy (Oughstun 2006a).

Electromagnetic pulse propagation in dispersive, attenuative media continues to be an area of much interest to not only academia but also industry. For example, dispersion effects play a central role in the development of modern optical communication networks. Accurate analysis of propagation of pulses used in optical communications often requires the inclusion of nonlinear terms (Agrawal 1989). As the data rates of optical systems continue to increase with commercially available products achieving rates over 300 Tbps the temporal pulse widths will exceed the characteristic optical relaxation times and these precursor fields will dominate the propagated signal (Oughstun 2006a).

Biological tissues are known to be highly dispersive with most tissues showing a similar dispersion curve to that of water. Dispersion in water, as well as biological tissues, is due to orientational polarization (Bohren and Huffman 1983) for frequencies $f < 300GHz$. For higher frequencies $f > 300GHz$ resonance polarization will dominate. Orientational polarization is described by the Debye model (Debye 1929) or its Rocard-Powles extension (McConnel 1980). Brillouin precursor fields do dominate the evolution of an electromagnetic pulse propagating through Debye like materials (Oughstun 2005) but have been ignored in analysis of bioelectromagnetics until this point.

Recent work in bioelectromagnetics (Foster 2000) makes the statement that precursors "do not have any apparent biological significance". Foster does admit that biological tissues are dispersive and that (ultra)wideband pulses experience an evolution leading to an overall change in the profile of the pulse due to the complicated phasal and attenuative relations. Other researchers have created (Chen and Wang 1994) an *anatomically correct* voxel based whole body model for calculating specific absorption rate (SAR) using numerical

12

techniques. This model is compromised of $45,000$ cells and the input is an ultrawideband half-cycle $40MHz$ sine wave with $1kV/m$ peak with a $12.5nS$ turn on time. The model found maximum induced currents of $3.9A$, $3.0A$ and $1.6A$ in the ankles, heart and neck, respectively. However, the numerical simulation did not result in the creation of precursor fields but this is excepted as the authors inappropriately ignored the known material dispersion by fixing their values at the carrier frequency of $40MHz$. Even with exclusion of precursor fields, which carry more energy into these materials, Chen found that 33% of the external field is transmitted into the whole body model.

1.3   Thesis Overview

This thesis provides a theoretical description of the dynamical evolution of an ultrawideband electromagnetic pulse as it propagates through a temporally dispersive and attenuative medium. Through the use of modern asymptotic theory and numerical techniques, propagation of canonical pulses into complex media are analyzed and extended to nonlinear materials. The materials of interest for this research are modeled after realistic biological tissues. The mathematically rigorous and physically accurate model description of electromagnetic energy transfer into the biological materials modeled are used to determine necessary field strengths for membrane breakdown and excitation. This detailed analysis provides a new point of view to working groups and standardization committees in the field of non-ionizing radiation safety that is based on so-called athermal effects.

Chapter 2 provides a necessary introduction to the mathematics and language used to describe electromagnetics. It begins with Maxwell's equations and the necessary material (constitutive) relations then proceeds to describe the electrical properties of materials. After this the boundary conditions are presented for an electromagnetic plane wave propagating across a boundary of two materials with differing refractive indices. The chapter concludes with the describing of precursor formation in dispersive dielectrics. In all chapters after this the language is slightly different as each is its own independent paper.

Chapter 3 shows the reflection and transmission of ultrawideband electromagnetic pulses through multilayered biological media consisting of three biological tissue layers representing skin, fat and muscle. The frequency dependent reflection and transmission coefficients of the multilayer stack are computed using the transfer matrix method. Each of the three tissues is modeled as a homogeneous, isotropic, linear, dispersive, attenuative, dielectric with frequency dispersion described by a multiple relaxation Rocard-Powles-Debye model fit to experimental data. This chapter also provides the dynamical evolution of an ultrawideband electromagnetic pulse incident upon a planar layered system of lossy, temporally dispersive, biological tissues. The frequency dispersion of each biological medium is described by the Rocard-Powles-Debye model with a static conductivity σ_0. The transmitted field structure consists of multiple pulses due to the series reflections inside the layered system, each dominated by leading and trailing edge Brillouin precursors. The peak amplitude of the transmitted pulse in the substrate decays algebraically and not exponentially as described by Beer's Law.

Chapter 4 includes the analysis of an ultrawideband pulse incident on an anatomically realistic system of layered biological tissues is presented. The analysis demonstrates what portion of the incident energy can be transmitted through the layered system into the biological substrate. Embedded in the substrate of muscle is an idealized biological, spherical cell whose dispersive material properties are taken to be that of water. The cell's dynamics are taken to be that modeled by the Fitzhugh-Nagumo model for an excitable neuron.

Chapter 5 demonstrates that optical precursors persist when the field strengths require the inclusion of nonlinear terms. It has been previously suggested, although not formally, that nonlinearities would extinguish precursor fields reducing their significance in the propagated field. It is important to realize that this work is carried out in the optical domain, far above the microwave and radio frequencies the rest of this dissertation is concerned with. This is because nonlinearities are much more significant in optical frequencies compare to the lower microwave frequencies. This chapter also reiterates the contributions of

this research and outlines future work.

Appendix A appears as published (Palombini and Oughstun 2011) showing the formulation of layered, dispersive, lossy biological materials and the resultant frequency dependent Fresnel coefficients.

Appendix B is the abstract which has been accepted at the 2012 IEEE International Symposium on Antennas and Propagation and USNC-URSI National Radio Science Meeting discussing the use of precursor fields to detect low observables.

Appendix C shows a derivation of the Fresnel reflection and transmission coefficients for lossy materials.

Appendix D provides a succinct overview of the Lorentz gauge and the Hertz potential. This is included since the Hertz potential is utilized as a solution to the wave equation in spherical coordinates.

Chapter 2

Fundamental Electromagnetic Formalism

2.1 Macroscopic Maxwell's Equations

The macroscopic Maxwell equations relate the interdependence of the electric field $\mathbf{E}\left(\mathbf{r}, t\right)$ and magnetic field $\mathbf{B}\left(\mathbf{r}, t\right)$ through a set of coupled equations given (in differential form) by

$$\nabla \cdot \mathbf{D}\left(\mathbf{r}, t\right) = \rho\left(\mathbf{r}, t\right), \tag{2.1}$$

$$\nabla \cdot \mathbf{B}\left(\mathbf{r}, t\right) = 0, \tag{2.2}$$

$$\nabla \times \mathbf{E}\left(\mathbf{r}, t\right) = -\frac{\partial}{\partial t}\mathbf{B}\left(\mathbf{r}, t\right), \tag{2.3}$$

$$\nabla \times \mathbf{H}\left(\mathbf{r}, t\right) = \mathbf{J}\left(\mathbf{r}, t\right) + \frac{\partial}{\partial t}\mathbf{D}\left(\mathbf{r}, t\right), \tag{2.4}$$

where $\mathbf{D}\left(\mathbf{r}, t\right)$ is the electric displacement vector $(coloumb/m^2)$, $\rho\left(\mathbf{r}, t\right)$ is the charge density $(coloumb/m^3)$, $\mathbf{E}\left(\mathbf{r}, t\right)$ is the electric field intensity vector $(volt/m)$, $\mathbf{B}\left(\mathbf{r}, t\right)$ is the magnetic induction vector $(tesla)$, $\mathbf{H}\left(\mathbf{r}, t\right)$ is the magnetic field intensity vector $(ampere/m)$ and $\mathbf{J}\left(\mathbf{r}, t\right)$ is the vector current density $(ampere/m^2)$. The two divergence relations Eqs. (2.1)-(2.2) are known as Gauss's law for the electric and magnetic fields, respectively, and the pair of curl relations Eqs. (2.3)-(2.4) are known, respectively, as Faraday's law and Ampére's

law as generalized by Maxwell (Maxwell 1873) through the inclusion of the displacement current $\partial/\partial t \mathbf{D}(\mathbf{r}, t)$.

By the law of conservation of charge, the charge density $\rho(\mathbf{r}, t)$ and current density $\mathbf{J}(\mathbf{r}, t)$ (which describes the flow of charge) are related by the *equation of continuity*

$$\nabla \cdot \mathbf{J}(\mathbf{r}, t) + \frac{\partial}{\partial t}\rho(\mathbf{r}, t) = 0. \tag{2.5}$$

The equation of continuity is contained in Maxwell's equations, as can be seen by substitution of the divergence of Eq. (2.4) into Eq. (2.1). This set of field equations is connected to physical measurements through the Lorentz force relation (Lorentz 1906),

$$\mathbf{F}(\mathbf{r}, t) = q\left(\mathbf{E}(\mathbf{r}, t) + \mathbf{v}(\mathbf{r}, t) \times \mathbf{B}(\mathbf{r}, t)\right), \tag{2.6}$$

where $\mathbf{F}(\mathbf{r}, t)$ is the force acting on a point charge q moving with velocity $\mathbf{v}(\mathbf{r}, t)$, in vacuum.

2.2   Constitutive Relations in Linear Electromagnetics

The macroscopic Maxwell's equations are completed by the the constitutive (material) relations relating the *induced fields* $\mathbf{D}(\mathbf{r}, t)$, $\mathbf{H}(\mathbf{r}, t)$ and $\mathbf{J}_c(\mathbf{r}, t)$ to the *primitive fields* $\mathbf{E}(\mathbf{r}, t)$ and $\mathbf{B}(\mathbf{r}, t)$. For all materials considered here the magnetic field effects are entirely negligible in comparison to effects produced by the electric field, that is $\mu \sim \mu_0$. Along with the additional assumption that the field strengths in question are sufficiently small that nonlinear terms unless explicitly stated to the contrary (as in Chapter 5) can be appropriately ignored then each material response may be expressed in the form of the general constitutive relation

$$\mathbf{G}(\mathbf{r}, t) = \int_{-\infty}^{\infty} d^3r' \int_{-\infty}^{t} dt' \hat{\underline{\zeta}}(\mathbf{r}', t', \mathbf{r}, t) \cdot \mathbf{F}(\mathbf{r}', t'), \tag{2.7}$$

where the volume integration is taken over all space the and the upper limit t in the temporal integral is bounded by causality. Here $\hat{\underline{\zeta}}(\mathbf{r}', t', \mathbf{r}, t)$ denotes the dielectric permittivity response tensor $\hat{\underline{\epsilon}}(\mathbf{r}', t', \mathbf{r}, t)$ when $\mathbf{F}(\mathbf{r}, t) = \mathbf{E}(\mathbf{r}, t)$, the inverse of the magnetic permeability

response tensor $\underline{\hat{\mu}}(\mathbf{r}', t', \mathbf{r}, t)$ when $\mathbf{F}(\mathbf{r}, t) = \mathbf{B}(\mathbf{r}, t)$, or the electric conductivity response tensor $\underline{\hat{\sigma}}(\mathbf{r}', t', \mathbf{r}, t)$ when $\mathbf{F}(\mathbf{r}, t) = \mathbf{E}(\mathbf{r}, t)$ and $\mathbf{G}(\mathbf{r}, t) = \mathbf{J}_c(\mathbf{r}, t)$, where $\mathbf{J}_c(\mathbf{r}, t)$ is the macroscopic conduction current density. The linear properties of the material are then determined by the analytical properties of each of the material tensors.

A material is said to be *spatially locally linear*, with regard to a specific property, if and only if $\underline{\hat{\zeta}}(\mathbf{r}', t', \mathbf{r}, t) = \underline{\hat{\zeta}}(\mathbf{r}', t', \mathbf{r}, t)\delta(\mathbf{r} - \mathbf{r}')$. Physically the statement of spatial local linearity says that every molecule is uncoupled from every other molecule in the material. A material is said to be *spatially homogeneous* if and only if its properties do not vary with position within the material as $\underline{\hat{\zeta}}(\mathbf{r}', t', \mathbf{r}, t) = \underline{\hat{\zeta}}(\mathbf{r} - \mathbf{r}', t', t)$. If this property is not satisfied then the material is said to be *spatially inhomogeneous*. Similarly, a material is said to be *temporally homogeneous* if and only if its properties do not vary with time as $\underline{\hat{\zeta}}(\mathbf{r}', t', \mathbf{r}, t) = \underline{\hat{\zeta}}(\mathbf{r}', \mathbf{r}, t - t')$. If this mathematical property is not satisfied then the material is said to be *temporally inhomogeneous*.

The spatiotemporal Fourier transform of Eq. (2.7) for a spatially and temporally homogeneous medium then yields, with application of the convolution theorem

$$\tilde{\tilde{\mathbf{G}}}(\mathbf{k}, \omega) = \tilde{\tilde{\underline{\zeta}}}(\mathbf{k}, \omega) \cdot \tilde{\tilde{\mathbf{F}}}(\mathbf{k}, \omega), \tag{2.8}$$

here the spatiotemporal Fourier transform of $\mathbf{F}(\mathbf{r}, t)$ is given by,

$$\tilde{\tilde{\mathbf{F}}}(\mathbf{k}, \omega) = \int_{-\infty}^{\infty} d^3r \int_{-\infty}^{\infty} dt \mathbf{F}(\mathbf{r}, t) e^{-\imath(\mathbf{k}\cdot\mathbf{r} - \omega t)} \tag{2.9}$$

with inverse transform,

$$\mathbf{F}(\mathbf{r}, t) = \frac{1}{(2\pi)^4} \int_{-\infty}^{\infty} d^3k \int_{-\infty}^{\infty} d\omega \tilde{\tilde{\mathbf{F}}}(\mathbf{k}, \omega) e^{\imath(\mathbf{k}\cdot\mathbf{r} - \omega t)}. \tag{2.10}$$

A *temporally dispersive* medium is one whose material tensor $\tilde{\tilde{\underline{\zeta}}}(\mathbf{k}, \omega)$ is explicitly dependent upon the temporal angular frequency ω, a property which is observed in all physically realizable materials. As a consequence, a material that is said to be nondispersive possess an instantaneous response to an electromagnetic stimulus and consequently is nonphysical (excluding vacuum).

18

The response tensor for a material that is locally linear, spatially inhomogeneous and temporally dispersive becomes $\hat{\underline{\zeta}}(\mathbf{r}', t', \mathbf{r}, t) = \hat{\underline{\zeta}}(\mathbf{r}, t - t')\delta(\mathbf{r} - \mathbf{r}')$. This leads to the constitutive relation for a locally linear, spatially homogeneous, spatially nondispersive, temporally dispersive material is seen to be given completely by $\tilde{\mathbf{G}}(\mathbf{r}, \omega) = \underline{\zeta}(\omega) \cdot \tilde{\mathbf{F}}(\mathbf{r}, \omega)$ in which there is no dependence of the position in the material.

The final material property to be considered is that of *isotropy*. A material is said to be *isotropic* if and only if the components of the response tensor satisfy the relation $\hat{\zeta}_{ij}(\mathbf{r}', t', \mathbf{r}, t) = \hat{\zeta}(\mathbf{r}', t', \mathbf{r}, t)\delta_{ij}$ where δ_{ij} is the Kronecker delta function and where $\hat{\zeta}(\mathbf{r}', t', \mathbf{r}, t)$ is independent of the indices i, j. If the material does not satisfy the relation above it is then said to be *anisotropic*.

The system response for a spatially homogeneous, isotropic, locally linear, temporally dispersive material is given by the convolution

$$\mathbf{G}(\mathbf{r}, t) = \int_{-\infty}^{t} \hat{\zeta}(t - t')\mathbf{F}(\mathbf{r}, t')dt', \tag{2.11}$$

with the temporal Fourier transform $\tilde{\mathbf{G}}(\mathbf{r}, \omega) = \zeta(\omega)\tilde{\mathbf{F}}(\mathbf{r}, \omega)$. The output field $\mathbf{G}(\mathbf{r}, \mathbf{t})$ is strictly dependent on the past behavior of the input field $\mathbf{F}(\mathbf{r}, t')$ and the past behavior of the material response tensor $\hat{\zeta}(t')$. Because of this, it is appropriate to express $\mathbf{F}(\mathbf{r}, t')$ in a Taylor series expansion about the time t' as

$$\mathbf{F}(\mathbf{r}, t') = \sum_{n=1}^{\infty} \frac{1}{n!} \frac{\partial^n}{\partial t^n} \mathbf{F}(\mathbf{r}, t)(t' - t)^n, \tag{2.12}$$

which is valid assuming that $\mathbf{F}(\mathbf{r}, t')$ and all of its derivates with respect to time exist for each $t \leq t'$. Substitution of the above Taylor series expansion into the constitutive relation given in Eq. (2.11) results in the expansion

$$\mathbf{G}(\mathbf{r}, t') = \sum_{n=1}^{\infty} \frac{1}{n!} \hat{\zeta}^{(n)} \left(\frac{\partial^n}{\partial t^n} \mathbf{F}(\mathbf{r}, t) \right)(t' - t)^n, \tag{2.13}$$

where

$$\hat{\zeta}^{(n)} \equiv \frac{(-1)^n}{n!} \int_0^{\infty} \hat{\zeta}(\tau)\tau^n d\tau \tag{2.14}$$

19

is proportional to the nth moment of the material response tensor. Upon taking the temporal Fourier transform of Eq. (2.13), the temporal Fourier transform of the material response function is found to be given by the Maclaurin series

$$\zeta(\omega) = \sum_{n=0}^{\infty} \hat{\zeta}^{(n)}(-\imath\omega)^n. \tag{2.15}$$

This expression shows that the real part of $\zeta(\omega)$ is an even function of ω whereas the imaginary part is an odd function of ω. The above expression for $\zeta(\omega)$ also provides the material expansion coefficients as

$$\hat{\zeta}^{(n)} = \frac{\imath^n}{n!} \frac{\partial^n}{\partial\omega^n}\zeta(\omega)\Big|_{\omega=0}, \tag{2.16}$$

as shown in (Oughstun 2006a).

2.3 Causality and Dispersion Relations

Causality at its roots is the simple principle stating that the effect cannot precede the cause. This fundamental statement is the most basic form of causality known as *primitive causality* (Nussenzveig 1972; Toll 1956). A more modern statement is the *principle of relativistic causality* which states that no signal can propagate with a velocity greater than the speed of light in vacuum c. These two principles are necessary when developing models for material dispersion dealing with ultrashort pulses.

Following the analysis by Hu (Hu 1989), given that the material response tensor satisfies the conditions given in Eq. (2.11), then the material response can be represented as a linear system with input signal $f_{in}(t)$ having temporal Fourier transform $\tilde{f}_{in}(\omega)$, and output signal $f_{out}(t)$ having temporal Fourier transform $\tilde{f}_{out}(\omega)$ that are related through the system transfer function $\chi(\omega)$ as

$$\tilde{f}_{out}(\omega) = \chi(\omega)\tilde{f}_{in}(\omega). \tag{2.17}$$

With primitive causality imposed, the causal impulse response function can be constructed as

$$\hat{\chi}(t) = U(t)\hat{\Psi}(t), \tag{2.18}$$

20

where $U(t) = 0$ for $t < 0$ and $U(t) = 1$ for $t > 0$ is the Heaviside unit step function and where $\hat{\Psi}(t) \equiv \hat{\chi}(t)$ for $t > 0$. The temporal Fourier transform of the Heaviside unit step function can be shown to be $\tilde{U}(\omega) = \mathcal{P}\left\{\frac{i}{\omega}\right\} + \pi\delta(\omega)$, where $\mathcal{P}$ denotes that the Cauchy principle value is to be taken.

Since $U(t) = 0$ for $t < 0$ the behavior of $\hat{\Psi}(t)$ for $t < 0$ can be freely chosen. There are two obvious choices, the first being $\hat{\Psi}(-|t|) = \hat{\Psi}(t)$, thereby making it an even function of t and resulting in a purely real Fourier spectrum $\Psi(\omega) = 2\Re\left\{\chi(\omega)\right\}$, so that

$$\Im\left\{\chi(\omega)\right\} = -\frac{1}{\pi}\mathcal{P}\int_{-\infty}^{\infty}\frac{\Re\left\{\chi(\omega')\right\}}{\omega' - \omega}d\omega', \tag{2.19}$$

where $\Re\{\cdot\}$ denotes the real part of the expression is to be taken, and $\Im\{\cdot\}$ denotes the imaginary party of the expression is to be taken. For the second choice, let $\hat{\Psi}(-|t|) = -\hat{\Psi}(t)$ so that $\hat{\Psi}(t)$ is an odd function of t and its Fourier spectrum is purely imaginary $\Psi(\omega) = 2i\Im\left\{\chi(\omega)\right\}$, so that

$$\Re\left\{\chi(\omega)\right\} = \frac{1}{\pi}\mathcal{P}\int_{-\infty}^{\infty}\frac{\Im\left\{\chi(\omega')\right\}}{\omega' - \omega}d\omega'. \tag{2.20}$$

This pair of relations shows that the real and imaginary parts of the impulse response function form a Hilbert transform pair in a causal system. Taken together, these two equations together are known as the *Plemelj formulae* (Plemelj 1908) or the *disperion relations* and can be generalized as Titchmarsh's theorem (Nussenzveig 1972; Titchmarsh 1939; Oughstun 2006a):

Titchmarsh's Theorem. *Any square-integrable function $\chi(\omega)$ with inverse Fourier transform $\hat{x}(t)$ that satisfies one of the following four conditions satisfies all four of them:*

1. $\hat{\chi}(t) = 0 \; \forall \; t < 0$

2. $\chi(\omega') = \lim_{\omega'' \to 0^+}\left\{\chi(\omega' + i\omega'')\right\}$ *for almost all ω', where $\chi(\omega)$ is holomorphic[1] in the upper-half of the complex $\omega = \omega' + i\omega''$ plane and is square-integrable over any line parallel to the ω'-axis in the upper-half plane.*

---

[1]A function f of the complex variable z is said to be *holomorphic* in an open set if it has a derivative at each point in that set, that is it is analytic.

3. $\Re\left\{\chi(\omega)\right\}$ and $\Im\left\{\chi(\omega)\right\}$ satisfy the first Plemelj formula Eq. (2.19).

4. $\Re\left\{\chi(\omega)\right\}$ and $\Im\left\{\chi(\omega)\right\}$ satisfy the second Plemelj formula Eq. (2.20).

2.3.1 The Dielectric Permittivity

For a spatially homogeneous, isotropic, locally linear, temporally dispersive medium, the constitutive relation Eq. (2.11) for the electric displacement vector is

$$\mathbf{D}\left(\mathbf{r}, t\right) = \int_{-\infty}^{t} \hat{\epsilon}(t - t')\mathbf{E}(\mathbf{r}, t')dt', \tag{2.21}$$

having temporal Fourier transform

$$\tilde{\mathbf{D}}\left(\mathbf{r}, \omega\right) = \epsilon(\omega)\tilde{\mathbf{E}}\left(\mathbf{r}, \omega\right), \tag{2.22}$$

where $\epsilon(\omega)$ is the temporal Fourier transform of the dielectric response function $\hat{\epsilon}(t)$. For a *simple polarizable dielectric*

$$\mathbf{D}\left(\mathbf{r}, t\right) = \epsilon_0 \mathbf{E}\left(\mathbf{r}, t\right) + \mathbf{P}\left(\mathbf{r}, t\right), \tag{2.23}$$

the electric susceptibility $\chi_e(\omega)$ is related to the dielectric permittivity as

$$\epsilon(\omega) = \epsilon_0\left(1 + \chi_e(\omega)\right), \tag{2.24}$$

$$= \epsilon'(\omega) + \imath\epsilon''(\omega), \tag{2.25}$$

such that the electric displacement vector in the Fourier domain is given by

$$\tilde{\mathbf{D}}\left(\mathbf{r}, \omega\right) = \epsilon_0\left(1 + \chi_e(\omega)\right)\tilde{\mathbf{E}}\left(\mathbf{r}, \omega\right). \tag{2.26}$$

In addition the material relation for the macroscopic polarization density is

$$\mathbf{P}\left(\mathbf{r}, t\right) = \epsilon_0 \int_{-\infty}^{t} \hat{\chi}_e(t - t')\mathbf{E}(\mathbf{r}, t')dt', \tag{2.27}$$

with temporal Fourier transform

$$\tilde{\mathbf{P}}\left(\mathbf{r}, \omega\right) = \epsilon_0\chi_e(\omega)\tilde{\mathbf{E}}\left(\mathbf{r}, \omega\right). \tag{2.28}$$

The material transfer functions for the macroscopic polarization density and electric displacement vector share the spectral symmetry relation

$$\chi_e^*(\omega) = \chi_e(\omega), \tag{2.29}$$

$$\epsilon^*(\omega) = \epsilon(-\omega), \tag{2.30}$$

provided ω is purely real. Because it describes the fundamental response, Titchmarsh's theorem applies to the electric susceptibility $\hat{\chi}_e(t)$. The dispersion relations for the dielectric permittivity are given by

$$\Re\{\epsilon(\omega) - \epsilon_0\} = \frac{1}{\pi}\mathcal{P}\int_{-\infty}^{\infty} \frac{\Im\{\chi(\omega')\}}{\omega' - \omega}d\omega', \tag{2.31}$$

$$\Im\{\epsilon(\omega)\} = -\frac{1}{\pi}\mathcal{P}\int_{-\infty}^{\infty} \frac{\Re\{\chi(\omega')\}}{\omega' - \omega}d\omega'. \tag{2.32}$$

These two equations are collectively known as the *Kramers–Kronig relations* (Kramers 1927; Kronig 1926).

2.3.2   The Electric Conductivity

For a spatially homogeneous, isotropic, locally linear, temporally dispersive conducting or semiconducting material, the constitutive relation Eq. (2.11) for the current conduction density vector becomes

$$\mathbf{J}_c(\mathbf{r}, t) = \int_{-\infty}^{t} \hat{\sigma}(t - t')\mathbf{E}(\mathbf{r}, t')dt' \tag{2.33}$$

having the temporal Fourier Transform

$$\tilde{\mathbf{J}}_c(\mathbf{r}, \omega) = \sigma(\omega)\tilde{\mathbf{E}}(\mathbf{r}, \omega), \tag{2.34}$$

where

$$\sigma(\omega) = \int_{-\infty}^{\infty} \hat{\sigma}(t)e^{\imath\omega t}dt, \tag{2.35}$$

is the *electric conductivity*. Because $\mathbf{J}_c(\mathbf{r}, t)$ and $\mathbf{E}(\mathbf{r}, t)$ are purely real vector fields the symmetry relation

$$\sigma^*(\omega) = \sigma(-\omega^*) \tag{2.36}$$

holds for complex $\omega = \omega' + \imath\omega''$.

The electric conductivity enters the dispersive material properties through the temporal Fourier transform of the macroscopic form of Ampére's law Eq. (2.4) in a semiconducting material, given by

$$\nabla \times \tilde{\mathbf{H}}(\mathbf{r}, \omega) = \tilde{\mathbf{J}}(\mathbf{r}, \omega) - \imath\omega\tilde{\mathbf{D}}(\mathbf{r}, \omega), \tag{2.37}$$

where $\tilde{\mathbf{J}}(\mathbf{r}, \omega) = \tilde{\mathbf{J}}_{ext}(\mathbf{r}, \omega) + \tilde{\mathbf{J}}_c(\mathbf{r}, \omega)$ with $\tilde{\mathbf{J}}_{ext}(\mathbf{r}, \omega)$ describing any externally applied current source. The substitution of $\tilde{\mathbf{D}}(\mathbf{r}, \omega) = \epsilon(\omega)\tilde{\mathbf{E}}(\mathbf{r}, \omega)$ into this result then yields

$$\nabla \times \tilde{\mathbf{H}}(\mathbf{r}, \omega) = \tilde{\mathbf{J}}_{ext}(\mathbf{r}, \omega) - \imath\omega\epsilon_c(\omega)\tilde{\mathbf{E}}(\mathbf{r}, \omega), \tag{2.38}$$

where

$$\epsilon_c(\omega) \equiv \epsilon(\omega) + \imath\frac{\sigma(\omega)}{\omega} \tag{2.39}$$

is called the *complex permittivity* of the material. Note that the permittivity $\epsilon(\omega) = \epsilon'(\omega) + \imath\epsilon''(\omega)$ and conductivity $\sigma(\omega) = \sigma'(\omega) + \imath\sigma''(\omega)$ are complex functions.

2.4 The Debye Model of Orientational Polarization

The relaxation equation due to Debye (Debye 1929)

$$\frac{d}{dt}\mathbf{p}(\mathbf{r}, t) + \frac{1}{\tau_m}\mathbf{p}(\mathbf{r}, t) = a\mathbf{E}_{\text{eff}}(\mathbf{r}, t), \tag{2.40}$$

describes the microscopic orientational polarization due to permanent molecular dipole moments $\mathbf{p}(\mathbf{r}, t)$, where a is a constant in time and where τ_m is the characteristic exponential relaxation time of the molecular dipole moment in the absence of any externally applied field $\mathbf{E}_{ext}(\mathbf{r}, t)$, and where the effective electric field from the dipole is $\mathbf{E}_{\text{eff}}(\mathbf{r}, t) = \mathbf{E}_{ext}(\mathbf{r}, t) + 1/(3\epsilon_0)\mathbf{P}(\mathbf{r}, t)$. The dipolar relaxation time is given by

$$\tau_m = \frac{\zeta}{2K_B T}, \tag{2.41}$$

through rotational Brownian motion theory (McConnel 1980), where K_B is Boltzmann's constant, T is the absolute temperature, and where ζ is a constant describing the resistance

to dipolar rotation in the medium. The temporal frequency transform of the spatial average of Eq. (2.40) then yields

$$\langle\langle \tilde{\mathbf{p}}\left(\mathbf{r},\omega\right)\rangle\rangle = \frac{a\tau_m}{1 - \imath\omega\tau_m} \left\langle\left\langle \tilde{\mathbf{E}}_{\text{eff}}\left(\mathbf{r},\omega\right)\right\rangle\right\rangle, \tag{2.42}$$

with $\langle\langle\cdot\rangle\rangle$ denoting the spatial average. The spatial average of a microscopic function $f\left(\mathbf{r},t\right)$ of position and time is defined as

$$\langle\langle f\left(\mathbf{r},t\right)\rangle\rangle \equiv \int w(\mathbf{r}')f(\mathbf{r}-\mathbf{r}',t)d^3r', \tag{2.43}$$

where $w(\mathbf{r})$ is a real-valued, positive, sufficiently well-behaved function that is nonzero only in some nonvanishing region of space surrounding the point $\mathbf{r} = \mathbf{0}$. This "weighting" function is normalized to unity over all of space as

$$\int_{-\infty}^{\infty} w(\mathbf{r})d^3r = 1, \tag{2.44}$$

and varies sufficiently slowly such that the local series approximation

$$w(\mathbf{r}+\mathbf{d}) \approx w(\mathbf{r}) + (\mathbf{d}\cdot\nabla)w(\mathbf{r}) + \frac{1}{2}(\mathbf{d}\cdot\nabla)^2 w(\mathbf{r}), \tag{2.45}$$

is well satisfied for $d = |\mathbf{d}|$ of the order of molecular sizes.

The molecular polarizability for the Debye model is then seen to be

$$\alpha(\omega) = \frac{a\tau_m}{1 - \imath\omega\tau_m}. \tag{2.46}$$

The electric susceptibility is then given by

$$\chi_e(\omega) = \frac{1}{\epsilon_0}\frac{N a\tau}{1 - \imath\omega\tau}, \tag{2.47}$$

where $\tau \equiv \tau_m/(1 - (1/3\epsilon_0)N a\tau_m)$, and N is the number density of the molecular species, so that the dielectric permittivity is

$$\epsilon(\omega) = \epsilon_0 + \frac{N a\tau}{1 - \imath\omega\tau}. \tag{2.48}$$

By evaluating this expression at $\omega = 0$, one finds that $a = \frac{\epsilon_s - \epsilon_0}{N\tau}$, where $\epsilon_s = \epsilon(0)$ is the static permittivity. With this identification, the single relaxation Debye model for permittivity becomes

$$\epsilon(\omega) = \epsilon_0 \left(1 + \frac{\epsilon_{sr} - 1}{1 - \imath\omega\tau} \right), \tag{2.49}$$

where $\epsilon_{sr} = \epsilon_s/\epsilon_0$ is the relative static permittivity.

A generalization of this expression is required to capture polarization mechanisms at higher frequencies $(\omega >> 1/\tau)$ and is given as

$$\epsilon(\omega)/\epsilon_0 = \epsilon_\infty + \frac{\epsilon_{sr} - \epsilon_\infty}{1 - \imath\omega\tau}, \tag{2.50}$$

where $\epsilon_\infty \geq 1$ is the high frequency limit of the relative dielectric permittivity. This expression can be further generalized to account for multiple relaxation modes and for any polarization mechanisms at higher frequencies as

$$\epsilon(\omega)/\epsilon_0 = \epsilon_\infty + \sum_j \frac{a_j}{1 - \imath\omega\tau_j}, \tag{2.51}$$

where a_j is the strength of the jth relaxation mode and is conserved as $\sum_j a_j = \epsilon_{sr} - \epsilon_\infty$, and τ_j is the relaxation time of the jth relaxation mode.

The Debye model as expressed in Eq. (2.51) has a nonvanishing absorption coefficient at high frequencies $\omega >> 1/\tau_1$, where the relaxation times τ_j are ordered in decreasing value. A first order correction to the Debye model of orientational polarization is provided by Rocard (Rocard 1933) and Powles (Powles 1948) as

$$\alpha(\omega) = \frac{a\tau_m}{(1 - \imath\omega\tau_m)(1 - \imath\omega\tau_{mf})}, \tag{2.52}$$

where $\tau_{mf} = I/\zeta$ is the associated friction time, with I the moment of inertia of the polar molecule and ζ the frictional appearing in Eq. (2.41). With this correction factor, the single mode Rocard-Powles-Debye model for permittivity becomes

$$\epsilon(\omega) = \epsilon_0 \left(1 + \frac{\epsilon_{sr} - 1}{(1 - \imath\omega\tau)(1 - \imath\omega\tau_f)} \right), \tag{2.53}$$

26

where τ is still the relaxation time as appears in Eq. (2.50) and τ_f is the effective friction time. Again, this expression can be generalized as in Eq. (2.50) to become

$$\epsilon(\omega)/\epsilon_0 = \epsilon_\infty + \frac{\epsilon_{sr} - \epsilon_\infty}{(1 - \imath\omega\tau)(1 - \imath\omega\tau_f)}, \tag{2.54}$$

and further expanded to include multiple relaxation modes and additional higher frequency effects as

$$\epsilon(\omega)/\epsilon_0 = \epsilon_\infty + \sum_j \frac{a_j}{(1 - \imath\omega\tau_j)(1 - \imath\omega\tau_{jf})}. \tag{2.55}$$

For a material with a nonzero static conductivity the above model can be extended as

$$\frac{\epsilon_c(\omega)}{\epsilon_0} = \epsilon_\infty + \sum_{j=1}^{N} \frac{a_j}{(1 - \imath\omega\tau_j)(1 - \imath\omega\tau_{fj})} + \imath\frac{\sigma_0}{\omega\epsilon_0}, \tag{2.56}$$

where ϵ_∞ is the high frequency limit of the relative permittivity of the model, $\epsilon_0 \approx 8.854 \times 10^{-12} F/m$ is the permittivity of free space, τ_j is the jth relaxation time, τ_{fj} is the associated j^{th} friction time, a_j is strength of the jth relaxation mode, and $\sigma_0 \equiv \sigma(0)$ is the static conductivity of the (semi-)conducting medium.

Biological materials are semiconducting with a frequency dependent dielectric permittivity $\epsilon(\omega)$ and electric conductivity $\sigma(\omega)$. These two aspects combine in electromagnetic theory to form the complex permittivity,

$$\epsilon_c(\omega) \equiv \epsilon(\omega) + \imath\frac{\sigma(\omega)}{\omega}, \tag{2.57}$$

where $\epsilon(\omega) = \epsilon'(\omega) + \imath\epsilon''(\omega)$ and $\sigma(\omega) = \sigma'(\omega) + \imath\sigma''(\omega)$. Upon combining real and imaginary parts of $\epsilon(\omega)$ and $\sigma(\omega)$, the complex permittivity may be expressed as

$$\epsilon_c(\omega) = \left(\epsilon'(\omega) - \frac{\sigma''(\omega)}{\omega} \right) + \imath \left(\epsilon''(\omega) + \frac{\sigma'(\omega)}{\omega} \right). \tag{2.58}$$

This form of the complex permittivity is appropriate for analyzing empirical data where all of the measured loss is improperly assumed to be conductive (Gabriel, Lau, and Gabriel 1996) with an effective conductivity $\sigma_{eff}(\omega) = \sigma'(\omega) + \omega\epsilon''(\omega)$ and effective permittivity $\epsilon_{eff}(\omega) = \epsilon'(\omega) - \sigma''(\omega)/\omega$.

2.5 Select Material Examples

2.5.1 Triply-Distilled H_2O

A material of particular interest that has been well studied from low frequencies up through optical frequencies is that of triply-distilled ($\sigma_0 = 0$) water at 25^oC. Casual models of the dielectric material dispersion have been shown to fit experimental data well, for frequencies from static ($\omega=0$r/s) in to the infrared ($\omega \sim 10^{12}$r/s), using a composite model for the material dispersion. For this low frequency band Oughstun (Oughstun 2006a) provides best-fit parameters for a double relaxation time Rocard-Powles-Debye model of water

$$\frac{\epsilon(\omega)}{\epsilon_0} = \epsilon_\infty + \sum_{j=1}^{2} \frac{a_j}{(1 - \imath\omega\tau_j)(1 - \imath\omega\tau_{fj})}, \qquad (2.59)$$

with parameters given in Table 2.1 here. The resultant frequency dispersion is illustrated in Fig. 2.1 along with collected experimental data provided by the United States Air Force Office of Scientific Research (AFOSR).

j	a_j	τ_j (sec)	τ_{fj} (sec)
1	74.1	8.44×10^{-12}	4.62×10^{-14}
2	3	4.77×10^{-14}	6.53×10^{-14}

Table 2.1: Rocard-Powles-Debye model parameters for triply-distilled water at 25^oC.
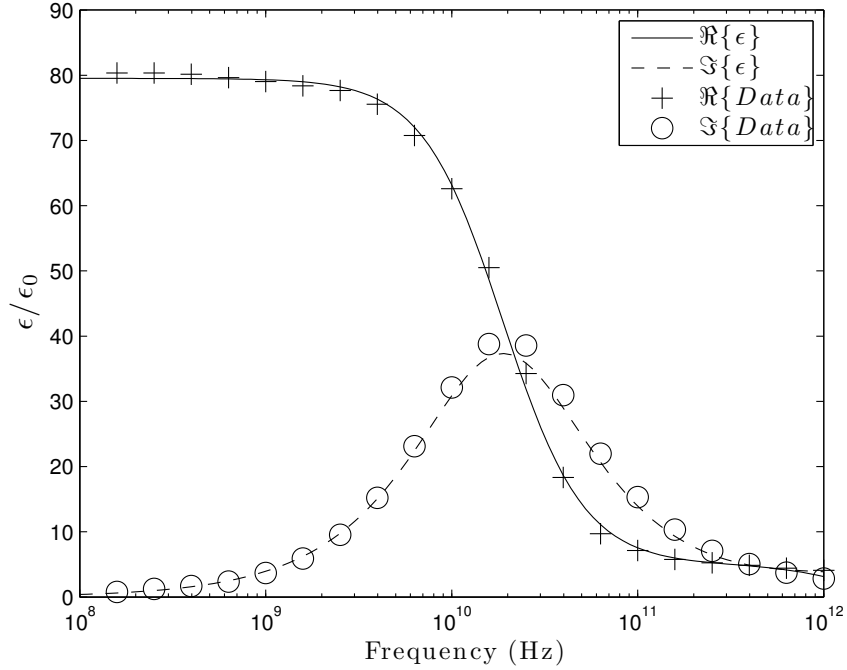
Figure 2.1: Real (solid) and imaginary (dashed) parts of the relative dielectric permittivity described by the Rocard-Powles-Debye model for water compared with experimental data.

2.5.2   Biological Tissues

The following semi-conducting Rocard-Powles-Debyle models for the biological tissues of skin, fat and muscle are based on experimental data (Gabriel, Lau, and Gabriel 1996) from 10Hz to 20GHz. To cover such a large frequency domain required the use of three separate impedance analyzers. For 10Hz to 10MHz the authors used an HP4192A impedance analyzer, for 300kHz to 3GHz an HP8753C was utilized and for the high frequency measurements from 130MHz to 20GHz an HP8720 was used. The samples were interfaced to the measurement equipment by use of an open-ended co-axial probe. The techniques and instrumentation used in this study gave random reproducibility of 1% across the entire frequency range. Uncertainty in the data is higher at frequencies below 1kHz where electrode polarization may have been undercorrected allowing for a factor of two or three in errors of the permittivity values below 100Hz.

29

Skin

The best-fit Rocard-Powles-Debyle model for skin is comprised of four relaxation modes $(N = 4)$ as

$$\frac{\epsilon(\omega)}{\epsilon_0} = \epsilon_\infty + \sum_{j=1}^{4} \frac{a_j}{(1 - \imath\omega\tau_j)(1 - \imath\omega\tau_{fj})} + \imath\frac{\sigma_0}{\omega\epsilon_0}. \tag{2.60}$$

The high frequency relative permittivity for dry skin is found to be $\epsilon_\infty = 15$ and the static conductivity to be $\sigma_0 = 3 \times 10^{-5} S/m$; the remaining model parameters are given in Table 2.2. Notice that the $j = 1$ and $j = 3$ modes provide the dominant structure of the frequency dispersion model fit depicted in Fig. 2.2, where the relative dielectric permittivity $\epsilon(\omega)$ and electric conductivity $\sigma(\omega)$ plotted there are the effective permittivity $\epsilon_{eff}(\omega)$ and conductivity $\sigma_{eff}(\omega)$ as expressed in Eq. (2.58).

j	a_j	τ_j (sec)	τ_{fj} (sec)
1	600	1×10^{-6}	1×10^{-14}
2	75	1×10^{-4}	1×10^{-12}
3	550	1×10^{-8}	1×10^{-12}
4	28	1×10^{-10}	1×10^{-13}

Table 2.2: Rocard-Powles-Debye model parameters for dry skin.

Fat

The best-fit Rocard-Powles-Debyle model for fat is composed of seven relaxation modes $(N = 7)$ as

$$\frac{\epsilon(\omega)}{\epsilon_0} = \epsilon_\infty + \sum_{j=1}^{7} \frac{a_j}{(1 - \imath\omega\tau_j)(1 - \imath\omega\tau_{fj})} + \imath\frac{\sigma_0}{\omega\epsilon_0}. \tag{2.61}$$

The higher number of terms that are required to describe the frequency dispersion of this biological medium is due to the relatively small value of the Debye relaxation time combined with several faster relaxation times exhibited in the data. The high frequency permittivity
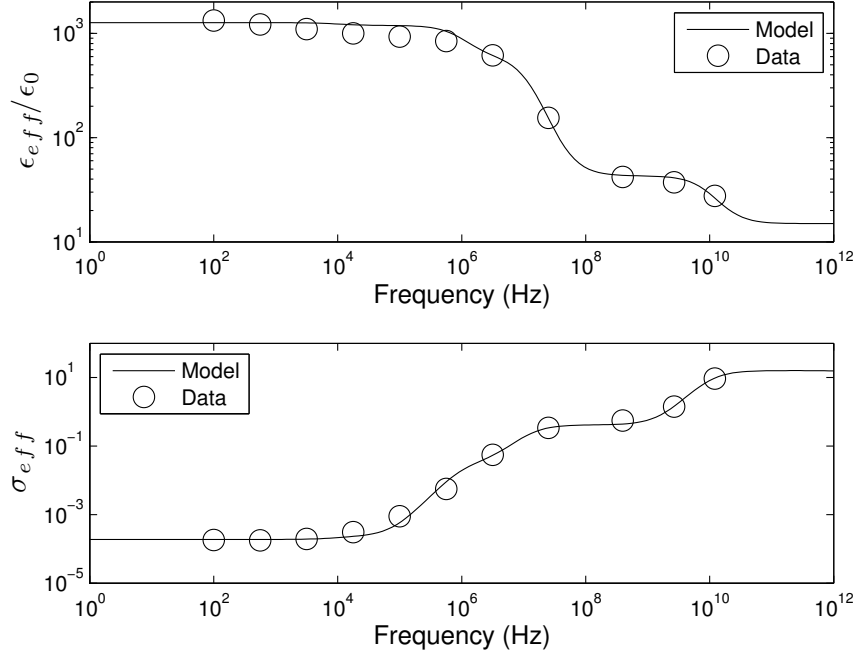
Figure 2.2: Comparison of Rocard-Powles-Debye model (solid curve) and empirical data (circles) of the relative complex dielectric permittivity of dry skin.

for fat was found to be $\epsilon_\infty = 3$ and the static conductivity to be $\sigma_0 = 1 \times 10^{-3} S/m$; the remaining model parameters are given in Table 2.3. The frequency dispersion for fat is illustrated in Fig. 2.3, where the relative dielectric permittivity $\epsilon_{eff}(\omega)$ and electric conductivity $\sigma_{eff}(\omega)$ plotted are the effective permittivity and conductivity as expressed in Eq. (2.58).

Muscle

The best-fit Rocard-Powles-Debyle model for muscle is composed of four relaxation modes $(N = 4)$ as

$$\frac{\epsilon(\omega)}{\epsilon_0} = \epsilon_\infty + \sum_{j=1}^{4} \frac{a_j}{(1 - \imath\omega\tau_j)(1 - \imath\omega\tau_{fj})} + \imath\frac{\sigma_0}{\omega\epsilon_0}. \tag{2.62}$$

The high frequency permittivity for fat was found to be $\epsilon_\infty = 28.3$ and the static conductivity to be $\sigma_0 = 3 \times 10^{-2} S/m$; the remaining model parameters are described in Table 2.4. The frequency dispersion for muscle is illustrated in Fig. 2.4, where the relative dielectric permittivity $\epsilon_{eff}(\omega)$ and electric conductivity $\sigma_{eff}(\omega)$ plotted are the effective permittivity

31

j	a_j	τ_j (sec)	τ_{fj} (sec)
1	3×10^7	1×10^{-1}	1×10^{-15}
2	5×10^5	1×10^{-2}	1×10^{-10}
3	1×10^4	1×10^{-3}	1×10^{-10}
4	7×10^2	1×10^{-4}	1×10^{-20}
5	100	1×10^{-5}	1×10^{-15}
6	9	1×10^{-7}	1×10^{-15}
7	3	1×10^{-10}	1×10^{-15}

Table 2.3: Rocard-Powles-Debye model parameters for fat.
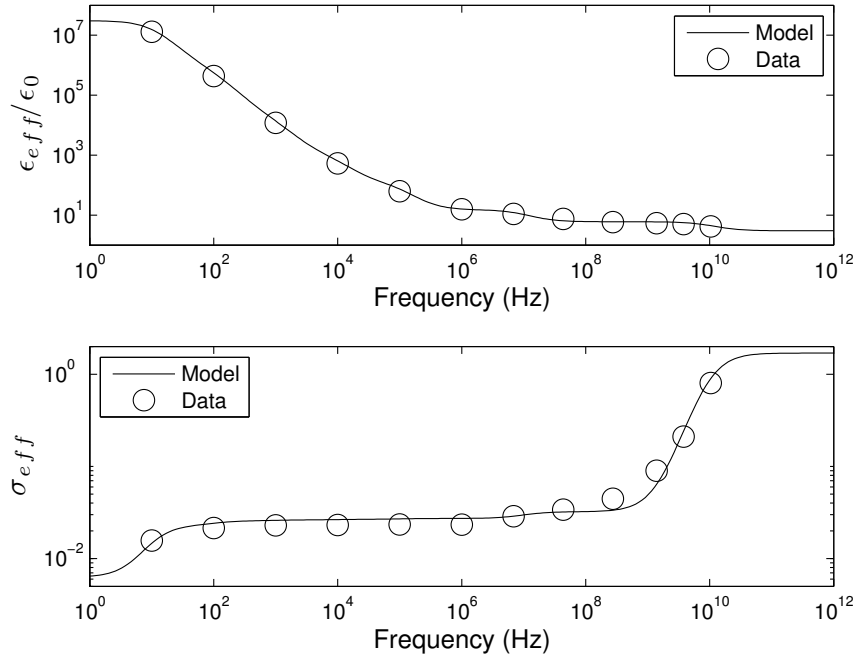
Figure 2.3: Comparison of Rocard-Powles-Debye model (solid curve) and empirical data (circles) of the relative complex dielectric permittivity of fat.

and conductivity as expressed in Eq. (2.58).

j	a_j	τ_j (sec)	τ_{fj} (sec)
1	2.05×10^7	6×10^{-3}	1×10^{-15}
2	1.5×10^4	9×10^{-6}	1×10^{-10}
3	7×10^3	1.5×10^{-6}	1×10^{-10}
4	45	1×10^{-10}	1×10^{-20}

Table 2.4: Rocard-Powles-Debye model parameters for muscle transverse to fibers.

2.5.3 Hypothetical Radar Absorbing Material (H-RAM)

A hypothetical radar absorbing material is constructed to block a specific carrier frequency ω_c such that the dielectric loss $\Im\{k(\omega)\} = \alpha(\omega) = \omega/c \, n_i(\omega)$ has a maximum at ω_c, where $c \, \alpha' = n_i(\omega) + \omega n_i'(\omega) = 0$ with the superscript $'$ denoting the derivate with respect to ω. Because the material is designed to be highly lossy in the neighborhood of ω_c, the material will be highly dispersive in that frequency band as well. The material is nonconducting ($\sigma \equiv 0$) and modeled as a single relaxation Debye-type dielectric

$$\frac{\epsilon(\omega)}{\epsilon_0} = \epsilon_\infty + \frac{a}{(1 - \imath\omega\tau)(1 - \imath\omega\tau_f)}, \tag{2.63}$$

with material parameters given in Table 2.5. The real and imaginary parts of the resultant dielectric frequency dispersion are depicted in Fig 2.5(a) and the corresponding frequency dependent loss in Fig. 2.5(b).

a	τ (sec)	τ_f (sec)
9	1×10^{-9}	1×10^{-11}

Table 2.5: Rocard-Powles-Debye model parameters for H-RAM.
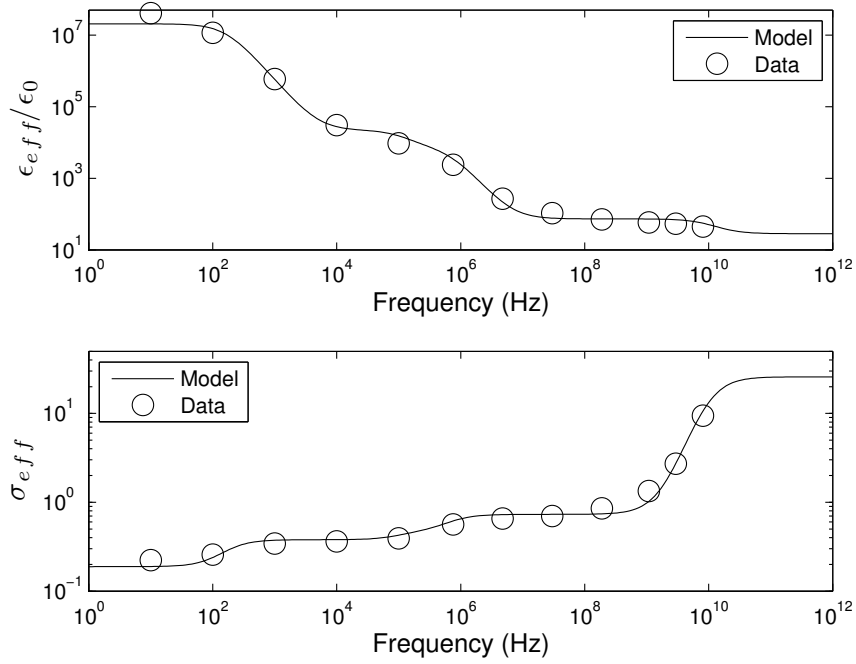
Figure 2.4: Comparison of Rocard-Powles-Debye model (solid curve) and empirical data (circles) of the relative complex dielectric permittivity of muscle transverse to fibers.

2.6 The Electromagnetic Boundary Conditions

Consider a continuous, smooth surface $\mathcal{S}$ forming the boundary between two separate homogeneous, isotropic, locally linear, temporally dispersive materials, across which a rapid change occurs in the material parameters $\epsilon(\omega)$, $\mu(\omega)$, and $\sigma(\omega)$ at almost every frequency[2]. When viewed from the macroscopic level, the changes across $\mathcal{S}$ appear to be discontinuous and accordingly the macroscopic field vectors are considered to change discontinuously across the interface. A more realistic, physical description consists of a thin transition layer of thickness Δl, across which the complex material parameters $\epsilon(\omega)$, $\sigma(\omega)$, and $\mu(\omega)$ change rapidly, but continuously as $\epsilon_1(\omega) \rightarrow \epsilon_2(\omega)$, $\sigma_1(\omega) \rightarrow \sigma_2(\omega)$, and $\mu_1(\omega) \rightarrow \mu_2(\omega)$ where the observation point progresses from medium 1 to medium 2. The rapid but continuous change through this transition layer is assumed to be sufficiently smooth such that both the

---

[2]By almost every frequency it is meant that, because of frequency dispersion there may exist isolated frequency values at which one or more of the material parameters is identical in value in the two media.
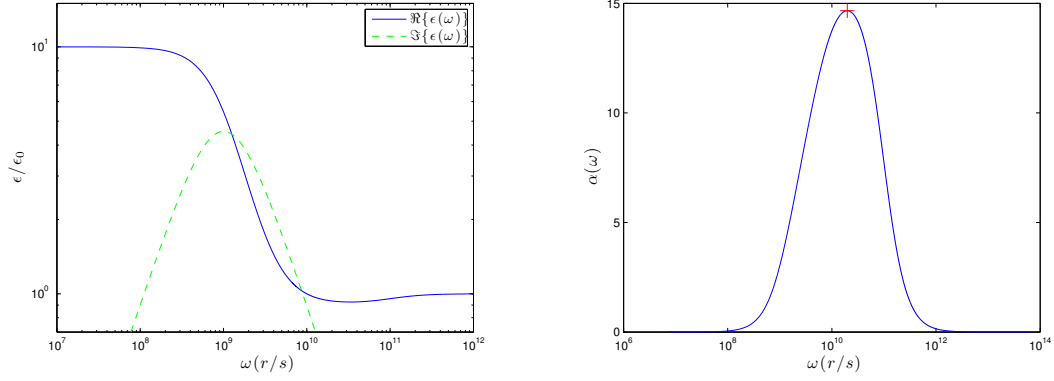
(a) Real (solid curve) and imaginary (dashed curve). (b) Loss factor with ω_c marked with $+$.

Figure 2.5: Rocard-Powles-Debye model of the relative dielectric permittivity and loss factor of H-RAM.

field vectors and their first derivatives are continuous, bounded functions in both time and space. The abrupt, discontinuous change across the interface $\mathcal{S}$ is then constructed from the limiting case as $\Delta l \to 0$ as illustrated in Fig. 2.6 (Oughstun 2006a).

The integral form of Gauss' law in the temporal frequency domain for the electric and magnetic fields are respectively

$$\oint_{\Sigma} \tilde{\mathbf{D}}\left(\mathbf{r}, \omega\right) \cdot d\mathbf{s} = \int_{R} \tilde{\varrho}\left(\mathbf{r}, \omega\right) d^3 r, \tag{2.64}$$

$$\oint_{\Sigma} \tilde{\mathbf{B}}\left(\mathbf{r}, \omega\right) \cdot d\mathbf{s} = 0, \tag{2.65}$$

where the simply-connected closed surface Σ encloses the region R, and where $d\mathbf{s}$ denotes the outward-oriented differential element of surface area on Σ. The Gaussian surface Σ is constructed as a circular cylinder whose generators are normal to the interface $\mathcal{S}$ and whose upper and lower end-caps (each with area Δa) lie respectively in medium 2 and medium 1 such that they are separated by the transition layer of thickness Δl. Let $\tilde{\mathbf{B}}_1\left(\mathbf{r}, \omega\right)$ denote the magnetic field vector at the center of the cylinder base with outward normal unit vector $\hat{\mathbf{n}}_1$, and let $\tilde{\mathbf{B}}_2\left(\mathbf{r}, \omega\right)$ denote the magnetic field vector at the center of the cylinder top with outward normal unit vector $\hat{\mathbf{n}}_2$. In the limit $\Delta l \to 0$ and $\Delta a \to 0$ the magnetic field vectors $\tilde{\mathbf{B}}_1\left(\mathbf{r}, \omega\right)$ and $\tilde{\mathbf{B}}_2\left(\mathbf{r}, \omega\right)$ are evaluated at the same point but on opposite sides of $\mathcal{S}$ such that $\hat{\mathbf{n}}_1 = -\hat{\mathbf{n}}$ and $\hat{\mathbf{n}}_2 = \hat{\mathbf{n}}$, where $\hat{\mathbf{n}}$ is directed from medium 1 to medium 2. In this limit

35
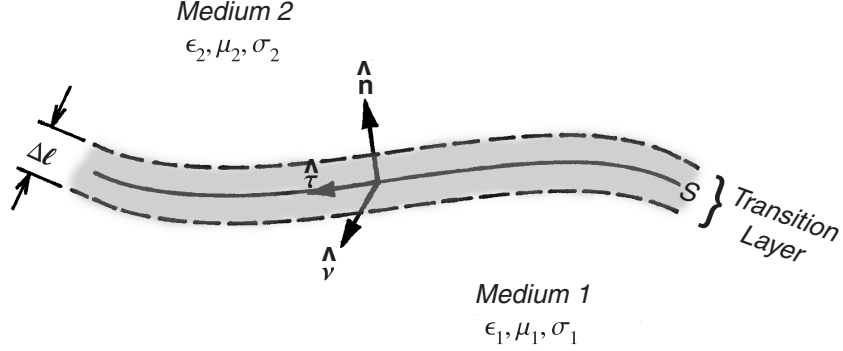
Figure 2.6: Transition layer about the interface $\mathcal{S}$ separating two dispersive, homogeneous, isotropic, locally linear media. At each point on the interface $\mathcal{S}$, the unit vector $\hat{\mathbf{n}}$ is normal to $\mathcal{S}$ and directed from medium 1 into medium 2, and the mutually orthogonal unit vectors $\hat{\tau}$ and $\hat{\nu}$ are tangent to $\mathcal{S}$, where $\hat{\tau} = \hat{\nu} \times \hat{\mathbf{n}}$.

Eq. (2.65) becomes

$$\hat{\mathbf{n}} \cdot \left(\tilde{\mathbf{B}}_2 \left(\mathbf{r}, \omega \right) - \tilde{\mathbf{B}}_1 \left(\mathbf{r}, \omega \right) \right) = 0, \ \mathbf{r} \in \mathcal{S}. \tag{2.66}$$

This result shows that *the normal component of the magnetic induction field vector is continuous across any surface of discontinuity in the material parameters*.

The response of the normal component of the electric displacement vector across the interface $\mathcal{S}$ is determined though a similar analysis of Eq. (2.64) with

$$\hat{\mathbf{n}} \cdot \left(\tilde{\mathbf{D}}_2 \left(\mathbf{r}, \omega \right) - \tilde{\mathbf{D}}_1 \left(\mathbf{r}, \omega \right) \right) = \lim_{\Delta l \to 0} \lim_{\Delta a \to 0} \int_R \tilde{\varrho} \left(\mathbf{r}, \omega \right) d^3 r. \tag{2.67}$$

The physical realization of the limit $\Delta l \to 0$ is that the charge enclosed in the region R approaches $\varrho_s \left(\mathbf{r}, \omega \right) \Delta a$ with $\varrho_s \left(\mathbf{r}, \omega \right)$ being the surface charge density on $\mathcal{S}$, whose

$$\varrho_s \left(\mathbf{r}, \omega \right) \equiv \lim_{\Delta l \to 0} \left\{ \varrho \left(\mathbf{r}, \omega \right) \Delta l \right\}. \tag{2.68}$$

With this identification the boundary condition becomes

$$\hat{\mathbf{n}} \cdot \left(\tilde{\mathbf{D}}_2 \left(\mathbf{r}, \omega \right) - \tilde{\mathbf{D}}_1 \left(\mathbf{r}, \omega \right) \right) = \varrho_s \left(\mathbf{r}, \omega \right), \ \mathbf{r} \in \mathcal{S} \tag{2.69}$$

provided that the limit $\Delta l \to 0$ and the integration over R can be interchanged. This result shows that *the normal component of the electric displacement vector is discontinuous across any surface of discontinuity in the material parameters, with the amount of the discontinuity being proportional to the free surface charge density at that point*.

The integral form of Faraday's and Ampére's laws are respectively given by

$$\oint_C \tilde{\mathbf{E}}(\mathbf{r}, \omega) \cdot d\mathbf{l} = \imath\omega \int_\Sigma \tilde{\mathbf{B}}(\mathbf{r}, \omega) \cdot \hat{\nu} d^2 r, \tag{2.70}$$

$$\oint_C \tilde{\mathbf{H}}(\mathbf{r}, \omega) \cdot d\mathbf{l} = -\imath\omega \int_\Sigma \tilde{\mathbf{D}}(\mathbf{r}, \omega) \cdot \hat{\nu} d^2 r + \int_\Sigma \tilde{\mathbf{J}}(\mathbf{r}, \omega) \cdot \hat{\nu} d^2 r, \tag{2.71}$$

in the temporal frequency domain, where Σ denotes the surface region enclosed by the contour C, and where $\hat{\nu}$ denotes the positive unit normal vector to the surface Σ, the direction of which is determined by the direction of integration about the contour C using the right-hand rule. The contour C is chosen to be an infinitesimally small plane rectangular loop whose sides (of length Δl) are perpendicular to the interface S and whose top and bottom (of length Δs) respectively lie in the upper and lower surfaces of the transition layer about the interface S. Let $\hat{\tau}_1$ and $\hat{\tau}_2$ denote the unit vectors in the direction of circulation about and tangent to the contour C along the lower (medium 1) and upper (medium 2) sides, respectively, of the rectangular contour at the edge of each transition layer. In addition, let $\tilde{\mathbf{E}}_1(\mathbf{r}, \omega)$ denote the electric field vector at the midpoint of the lower side of C in medium 1 with circulation vector $\hat{\tau}_1$, and let $\tilde{\mathbf{E}}_2(\mathbf{r}, \omega)$ denote the electric field vector at the midpoint of the upper side of C in medium 2 with circulation vector $\hat{\tau}_2$. In the limit as both $\Delta l \to 0$ and $\Delta s \to 0$, the electric field vectors $\tilde{\mathbf{E}}_1(\mathbf{r}, \omega)$ and $\tilde{\mathbf{E}}_2(\mathbf{r}, \omega)$ are evaluated at the same point but on opposite sides of the interface S, where as $\hat{\tau}_1 \to -\hat{\tau}$ and $\hat{\tau}_2 \to \hat{\tau}$ where,

$$\hat{\tau} \equiv \hat{\nu} \times \hat{\mathbf{n}} \tag{2.72}$$

defines the unit tangent vector to the surface S at that point. In this limit, Faraday's law Eq. (2.70) becomes

$$\hat{\nu} \cdot \left[\hat{\mathbf{n}} \times \left(\tilde{\mathbf{E}}_2(\mathbf{r}, \omega) - \tilde{\mathbf{E}}_1(\mathbf{r}, \omega) \right) - \imath\omega \lim_{\Delta l \to 0} \tilde{\mathbf{B}}(\mathbf{r}, \omega) \Delta l \right] = 0, \ \mathbf{r} \in S, \tag{2.73}$$

37

after application of the vector indentity $(\hat{\nu} \times \hat{\mathbf{n}}) \cdot \tilde{\mathbf{E}} = \hat{\nu} \cdot (\hat{\mathbf{n}} \times \tilde{\mathbf{E}})$. Because the orientation of the contour C, and hence the direction of the unit vector $\hat{\nu}$, is entirely arbitrary, then

$$\hat{\mathbf{n}} \times \left(\tilde{\mathbf{E}}_2 (\mathbf{r}, \omega) - \tilde{\mathbf{E}}_1 (\mathbf{r}, \omega) \right) = \imath \omega \lim_{\Delta l \to 0} \tilde{\mathbf{B}} (\mathbf{r}, \omega) \, \Delta l, \ \mathbf{r} \in S. \tag{2.74}$$

Finally, because the field vectors and their first derivatives are assumed to be bounded, the right-hand side of this relation vanishes with Δl, resulting in the boundary condition

$$\hat{\mathbf{n}} \times \left(\tilde{\mathbf{E}}_2 (\mathbf{r}, \omega) - \tilde{\mathbf{E}}_1 (\mathbf{r}, \omega) \right) = 0, \ \mathbf{r} \in S. \tag{2.75}$$

Hence, *the tangential component of the electric field intensity vector is continuous across any surface of discontinuity in the material parameters.*

In order to analyze the behavior of the tangential component of the magnetic intensity vector across a surface S of discontinuity in the material parameters, a similar analysis is applied to Ampére's law Eq. (2.71), which results in the limiting expression

$$\hat{\mathbf{n}} \times \left(\tilde{\mathbf{H}}_2 (\mathbf{r}, \omega) - \tilde{\mathbf{H}}_1 (\mathbf{r}, \omega) \right) = \lim_{\Delta l \to 0} \tilde{\mathbf{J}} (\mathbf{r}, \omega) \, \Delta l - \imath \omega \lim_{\Delta l \to 0} \tilde{\mathbf{D}} (\mathbf{r}, \omega) \, \Delta l, \ \mathbf{r} \in S. \tag{2.76}$$

Because $\tilde{\mathbf{D}} (\mathbf{r}, \omega)$ and its first derivatives are bounded, the second term on the right-hand side of this expression vanishes in the limit as $\Delta l \to 0$. However, the first term on the right-hand side of this expression does not necessarily vanish as it is proportional to the current $\mathcal{J} = \mathbf{J} (\mathbf{r}, t) \cdot \hat{\nu} \Delta s \Delta l$ flowing through the rectangular loop C. In the limit as $\Delta l \to 0$, the current $\mathcal{J}$ approaches the limiting value $\mathbf{J}_S (\mathbf{r}, t) \cdot \hat{\mathbf{n}} \Delta s$, where

$$\tilde{\mathbf{J}}_S (\mathbf{r}, \omega) \equiv \lim_{\Delta l \to 0} \tilde{\mathbf{J}} (\mathbf{r}, \omega) \tag{2.77}$$

is the temporal frequency spectrum of the surface current density on the interface S between the two media. With this identification, the above boundary condition becomes

$$\hat{\mathbf{n}} \times \left(\tilde{\mathbf{H}}_2 (\mathbf{r}, \omega) - \tilde{\mathbf{H}}_1 (\mathbf{r}, \omega) \right) = \tilde{\mathbf{J}}_S (\mathbf{r}, \omega), \ \mathbf{r} \in S. \tag{2.78}$$

Hence, *the presence of a surface current on the interface S across which the material parameters change discontinuously, results in a discontinuous change in the tangential component*

of the magnetic field intensity vector, the amount of the discontinuity being proportional to the surface current density at that point.

Notice that surface charge and current densities are not independent, but rather are related through the equation of continuity given in Eq. (2.5). In the limit as $\Delta l \to 0$, the temporal Fourier transform of Eq. (2.5) becomes

$$\nabla \cdot \tilde{\mathbf{J}}_S\left(\mathbf{r}, \omega\right) - \imath \omega \tilde{\varrho}_S\left(\mathbf{r}, \omega\right) = 0. \tag{2.79}$$

Because of this relationship, it is necessary only to apply the boundary conditions given in Eqs. (2.75) and (2.78) on the tangential components of the electric and magnetic field vectors, the boundary conditions given in Eqs. (2.66) and (2.69) then being automatically satisfied (Oughstun 2006a).

2.7   Conclusions

This chapter introduces the terminology and provides adequate background necessary for comprehension of the following chapters. The presentation of the constitutive relations for a spatially homogeneous, isotropic, locally linear and temporally dispersive material is necessary in order to understand how electromagnetic radiation interacts with matter. The material descriptions presented here will be used throughout the remaining chapters to provide numerical examples of this interaction.

Chapter 3

Reflection and Transmission of Pulsed Electromagnetic Fields Through Multilayered Media

3.1 Introduction

The interaction of non-ionizing radiation with biological tissue remains a problem of great concern as much remains to be understood about the athermal effects of such interactions. It is largely believed that non-ionizing radiation is harmless below exposure levels where heating first occurs (Adair 2003). However, this conclusion assumes a continuous, monochromatic signal without any mention of either transient phenomena or pulsed fields that are typically associated with both radar and mobile communications. Pulsed fields and their associated transient phenomena are of central importance in the proper analysis of the biological response to applied external fields since the action potential threshold response in biological cellular signaling is dependent on the rise time (submillisecond) of the incident field (Cole 1955). In addition, it has been shown that exposure to such stimuli can cause both molecular effects as well as phenotypic effects that are a visible manifestation of

genetics (Barnes 2005).

The recently published study conducted by The National Research Council of the National Academy of Sciences (Barnes 2005) has explored possible health effects of pulsed, low-level phased-array radio frequency energy exposure due to the PAVE-PAWS (Precision Acquisition Vehicle Entry-Phased Array Warning System) radar system located at Cape Cod Air Force Station at Otis Air Force Base in Massachusetts. The study raises several important questions regarding the possible health effects of such non-ionizing radiation, describing physical mechanisms for radio frequency effects on biological systems. However, what the report fails to address are the effects of multiple reflection and transmission through layered biological materials. Results presented here, based on empirical data, suggest penetration depths much greater than that previously described by simple theoretical results.

The specific absorption rate threshold set by the Federal Communications Commission (FCC) on hand-held mobile phones is $1.6W/kg$, as measured over any one gram of tissue. Recently published research (Volkow, Tomasi, Wang, Vaska, Fowler, Telang, Alexoff, Logan, and Wong 2011) has shown that mobile communication devices operating within these radio-frequency limits increase glucose metabolism in the region of the brain closest to the antenna but admits that "the finding is of unknown clinical significance". This then raises concern about the efficacy of this safety standard when applied to ultrawideband (uwb) pulsed fields.

The analysis presented in this and later chapters provides a mathematically rigorous, physical model description of the propagation of pulsed electromagnetic fields into realistic biological tissues in order to investigate the possible indirect molecular effects such fields have on cellular signaling. The first step in this formulation is a systematic description of the interaction a plane wave encounters at a boundary between a lossless nondispersive medium and a lossy dispersive medium as well as when both media are lossy and dispersive. Recent work (Roy 2003) provides some explanation of how a uniform plane wave in a lossless media incident on a boundary with a lossy media results in the transmission of a nonuniform

plane wave in the second media. However, this work does not consider dispersive media and does not include insight as to how pulsed energy is reflected and transmitted at such an interface.

Finally, it is now known that when electromagnetic signals that are ultrawideband with respect to the material dispersion propagate through a dispersive medium, electromagnetic precursors emerge in the propagated signal (Oughstun 2005). Of particular importance is the fact that increased energy transmission, on the scale of multiple orders of magnitude, occurs due to this precursor field formation. Such pulses may then be used for biological imaging and therapy and are the impetus for this research.

3.2 Transfer Matrix Formulation for Multilayered Dispersive Absorptive Media

The transfer matrix method (Yeh 1988) is used here for the description of reflection from and transmission through a system of N parallel plane stacked layers illustrated in Fig. 3.1. The jth layer has thickness Δz_j with dispersive properties described by complex index of refraction $n_j(\omega)$ in the temporal frequency domain. It has been shown (Pereyra and Robledo-Martinez 2009) that this approach is equivalent to the Fresnel formulation leading to the Airy formula but is less cumbersome to deal with when there is more than one sandwiched layer.

The analysis begins with the electromagnetic boundary conditions for the tangential components of the fields [see Eqs. (2.75) and (2.78)] at the planar interface separating medium j from medium $j + 1$, $j = 0, 1, 2..., N$, given by

$$\hat{\mathbf{n}} \times \left(\tilde{\mathbf{E}}_{j+1}(\mathbf{r}, \omega) - \tilde{\mathbf{E}}_j(\mathbf{r}, \omega) \right) = 0, \tag{3.1}$$

$$\hat{\mathbf{n}} \times \left(\tilde{\mathbf{H}}_{j+1}(\mathbf{r}, \omega) - \tilde{\mathbf{H}}_j(\mathbf{r}, \omega) \right) = \tilde{\mathbf{J}}_s(\mathbf{r}, \omega), \tag{3.2}$$

across a planar interface with unit normal vector $\hat{\mathbf{n}}$ directed from the incident (j) to the transmitted $(j + 1)$ medium. The coupled equations for the electric field vectors at the
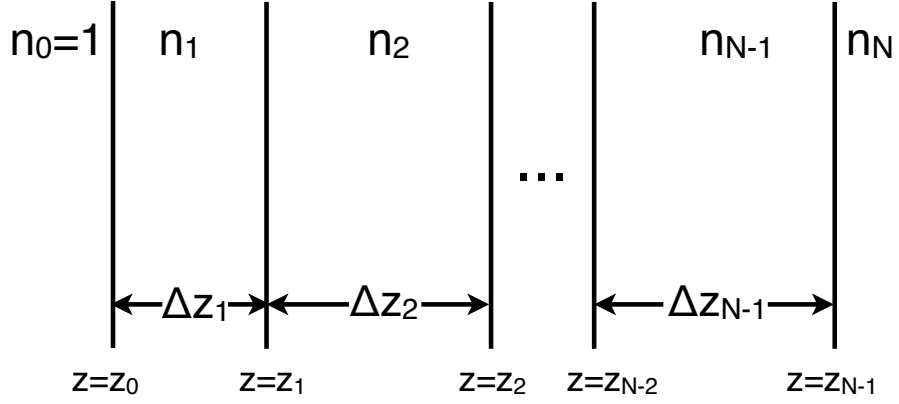
Figure 3.1: Parallel plane layered media with n_j the refractive index and Δz_j the thickness of the jth layer, $j = 1, 2, ..., N - 1$.

interface are then given by

$$\left(\tilde{\mathbf{E}}_j + \tilde{\mathbf{E}}'_j\right) \cdot \hat{\nu} = \left(\tilde{\mathbf{E}}_{j+1} + \tilde{\mathbf{E}}'_{j+1}\right) \cdot \hat{\nu}, \tag{3.3}$$

$$\left(\tilde{\mathbf{E}}_j - \tilde{\mathbf{E}}'_j\right) \cdot \hat{\nu} n_j = \left(\tilde{\mathbf{E}}_{j+1} - \tilde{\mathbf{E}}'_{j+1}\right) \cdot \hat{\nu} n_{j+1} + \tilde{\mathbf{J}}_s, \tag{3.4}$$

where $\hat{\nu}$ is the unit tangent vector to the surface, and where $\tilde{\mathbf{E}}_j$ and $\tilde{\mathbf{E}}'_j$ respectively denote the right (transmitted) and left (reflected) moving wave in the jth layer. The surface current density $\tilde{\mathbf{J}}_s(\mathbf{r}, \omega)$ is confined to a transition layer of thickness Δl which spans each interface and extends an equal distance into each medium. Over this transition layer the frequency dependent conductivity is varied with some interpolating function in order to continuously connect the two layers.

3.2.1 Single Layer Case

For the case of a single layer of finite thickness Δz the system of equations can be solved analytically. The principle time-harmonic field components within the incident medium traveling in the z direction are

$$E_i = E_0 e^{i(k_0 z - \omega t)}, \qquad\qquad H_i = \frac{k_0}{\omega \mu_0} E_i, \tag{3.5}$$

$$E_r = E_1 e^{-i(k_0 z + \omega t)}, \qquad\qquad H_r = -\frac{k_0}{\omega \mu_0} E_r, \tag{3.6}$$

43

where the subscript i denotes the incident field and the subscript r denotes the reflected field, and where $k_0 = n_0\omega/c$ is the wavenumber in the incident medium. The first $(j = 1)$ layer $0 \leq z \leq \Delta z$ will contain both a right and left moving wave, where the left moving wave is indicated with a superscript $'$ as

$$E_m = \left(E_2 e^{\imath k_1 z} + E_2' e^{-\imath k_1 z} \right) e^{-\imath \omega t}, \tag{3.7}$$

$$H_m = \frac{k_1}{\omega \mu_1} \left(E_2 e^{\imath k_1 z} - E_2' e^{-\imath k_1 z} \right) e^{-\imath \omega t}, \tag{3.8}$$

where $k_1 = n_1\omega/c$ is the wavenumber in the layer. The fields in the substrate layer $z \geq \Delta z$ will only have a right moving component as it is semi-infinite and are given by

$$E_t = E_3 e^{\imath(k_2 z - \omega t)}, \tag{3.9}$$

$$H_t = \frac{k_2}{\omega \mu_2} E_t, \tag{3.10}$$

where the subscript t denotes the transmitted field, and where $k_2 = n_2\omega/c$ is the wavenumber in this medium. It will be convenient at this point to introduce the *complex intrinsic impedance* of the homogeneous, isotropic, temporally dispersive medium, which is defined as the magnitude ratio of the electric field intensity to the magnetic field intensity as

$$\eta_j(\omega) = \frac{E_j}{H_j} \tag{3.11}$$

$$= \left[\frac{\mu_j(\omega)}{\epsilon_{c_j}(\omega)} \right]^{1/2}. \tag{3.12}$$

Additionally, impedance ratios between the jth and k^{th} layer are defined here as

$$\eta_{jk}(\omega) = \frac{\eta_j(\omega)}{\eta_k(\omega)}. \tag{3.13}$$

Notice that $\eta_{jk} = \eta_{kj}^{-1}$.

Application of the boundary condition for the tangential component of the electric field given in Eq. (2.75) at the interface between the first and second media at $z = 0$, results in

$$\left(E_0 e^{\imath k_0 z} + E_1 e^{-\imath k_0 z} \right) e^{-\imath \omega t} = \left(E_2 e^{\imath k_1 z} + E_2' e^{-\imath k_1 z} \right) e^{-\imath \omega t}, \tag{3.14}$$

where E_0 is the amplitude of the incident electric field, E_1 is the amplitude of the reflected field, E_2 is the amplitude of the right moving wave in the second layer, and E_2' is the amplitude of the left moving in that layer. Upon canceling the common $e^{-\iota\omega t}$ dependence, evaluating this expression at $z = 0$ relates the electric field amplitudes as

$$E_0 + E_1' = E_2 + E_2'. \tag{3.15}$$

Application of the same boundary condition at the interface separating the second and third medium at $z = \Delta z$ results in

$$\left(E_2 e^{\iota k_1 z} + E_2' e^{-\iota k_1 z} \right) e^{-\iota\omega t} = E_3 e^{\iota k_2 z} e^{-\iota\omega t}, \tag{3.16}$$

where E_3 is the amplitude of the transmitted field in the third medium occupying the half-space $z > \Delta z$. After canceling the time dependence and substituting $z = \Delta z$, one obtains Stratton's result [(Stratton 1941) pg. 512 Eq. (8)]

$$E_2 e^{\iota k_2 \Delta z} + E_2' e^{-\iota k_2 \Delta z} = E_3 e^{\iota k_3 \Delta z}. \tag{3.17}$$

This result is incorrect as the right-hand side of the equation states that the transmitted wave has already propagated a distance $z = \Delta z$ into medium 3 which is not the case because the wave has just entered the third medium. The correct result here is subtly different, relating the field amplitudes as

$$E_2 e^{\iota k_2 \Delta z} + E_2' e^{-\iota k_2 \Delta z} = E_3, \tag{3.18}$$

where the absence of the $e^{\iota k_3 \Delta z}$ shows that the energy has not yet entered substrate layer but is still at the interface $z = \Delta z$.

Analysis of the magnetic intensity field follows in a similar fashion by starting with the boundary condition given in Eq. (2.78). Application of the boundary conditions at the first interface separating the first and second medium results in the set of relations

$$H_1 = H_2, \tag{3.19}$$

$$H_i + H_r = H_m, \tag{3.20}$$

$$\frac{1}{\eta_0(\omega)} \left(E_0 e^{\iota k_1 z} - E_i e^{-\iota k_1 z} \right) e^{-\iota\omega t} = \frac{1}{\eta_1(\omega)} \left(E_2 e^{\iota k_1 z} - E_2' e^{-\iota k_1 z} \right) e^{-\iota\omega t}. \tag{3.21}$$

Upon removing the common time dependent factor $e^{i\omega t}$ and evaluating the result at $z = 0$, the above equation relates the field amplitudes as

$$E_0 - E_1 = \eta_{01}(\omega)\left(E_2 - E_2'\right), \tag{3.22}$$

where $\eta_{01}(\omega)$ is the impedance ratio defined in Eq. (3.13). The same boundary condition is used to relate the field amplitudes across the second interface at $z = \Delta z$ separating the second and third mediums as

$$H_2 = H_3, \tag{3.23}$$

$$H_m = H_t, \tag{3.24}$$

$$\frac{1}{\eta_1(\omega)}\left(E_2 e^{ik_1 z} - E_2' e^{-ik_1 z}\right)e^{-i\omega t} = \frac{1}{\eta_2(\omega)}E_3 e^{ik_2(z - \Delta z)}e^{-i\omega t}. \tag{3.25}$$

Upon removing the common time dependent factor $e^{-i\omega t}$ and substituting $z = \Delta z$ results in Stratton's incorrect result [(Stratton 1941) pg. 513 Eq. (8)]

$$E_2 e^{ik_2 \Delta z} + E_2' e^{-ik_2 \Delta z} = \eta_{23}(\omega)E_3 e^{-ik_3 \Delta z}, \tag{3.26}$$

again suggesting that the transmitted wave has already traveled a distance Δz into the third medium. The correct result is

$$E_2 e^{ik_1 \Delta z} + E_1' e^{-ik_1 \Delta z} = \eta_{12}(\omega)E_3. \tag{3.27}$$

The solution of this system of equations for the reflected field E_1 and the transmitted field E_3 in terms of the material properties and incident field amplitude E_0 gives

$$\frac{E_1}{E_0} = \frac{r_{01} + r_{12}e^{ik_1 \Delta z}}{1 + r_{01}r_{12}e^{ik_1 \Delta z}}, \tag{3.28}$$

$$\frac{E_3}{E_0} = \frac{1}{(1 + \eta_{01})(1 + \eta_{12})}\frac{4e^{ik_1 \Delta z}}{1 + r_{01}r_{12}e^{i2k_1 \Delta z}}, \tag{3.29}$$

where r_{01} and r_{12} are, respectively, the Fresnel reflection coefficients for lossy media (Canning 2011) at the first and second interfaces. For normal incidence the corrected (allowing

for material loss) Fresnel reflection and transmission coefficients are respectively given by

$$r_{ij} = \frac{2\mu_j k_i}{\mu_j k_i + \mu_i \left[\Re\{k_j\} + i\Im\{k_j\}\right]}, \tag{3.30}$$

$$t_{ij} = \frac{\mu_j k_i - \mu_i \left[\Re\{k_j\} + i\Im\{k_i\}\right]}{\mu_j k_i + \mu_i \left[\Re\{k_j\} + i\Im\{k_i\}\right]}, \tag{3.31}$$

where $\Re\{k_j\}$ and $\Im\{k_j\}$ respectively denote the real and imaginary components of the propagation factor in the jth medium (see Appendix C for derivation). Notice that Stratton's result [(Stratton 1941) pg. 492 Eq. (14)] is obtained in the lossless medium case when $\Im\{k_i\} = \Im\{k_j\} = 0$.

3.2.2 Multilayer Case

These boundary conditions at the jth interface $\mathcal{S}_j$, separating the jth from the $(j+1)^{th}$ layer can be compactly represented in matrix form as

$$\mathcal{D}_j(\omega) \left[\begin{array}{c} \tilde{\mathbf{E}}_j(\omega) \\ \tilde{\mathbf{E}}'_j(\omega) \end{array} \right] = \mathcal{D}_{j+1}(\omega) \left[\begin{array}{c} \tilde{\mathbf{E}}_{j+1}(\omega) \\ \tilde{\mathbf{E}}'_{j+1}(\omega) \end{array} \right], \tag{3.32}$$

where $\mathcal{D}_j(\omega)$ is the dynamical matrix

$$\mathcal{D}_j(\omega) = \left(\begin{array}{cc} 1 & 1 \\ n_j(\omega) + \sigma & \sigma - n_j(\omega) \end{array} \right). \tag{3.33}$$

In addition, a propagation matrix $\mathcal{P}_j$ may be defined for each layer j of finite thickness Δz_j as

$$\mathcal{P}_j(\omega) = \left(\begin{array}{cc} e^{i\Delta z_j \tilde{\mathbf{k}}_j(\omega)} & 0 \\ 0 & e^{-i\Delta z_j \tilde{\mathbf{k}}_j(\omega)} \end{array} \right). \tag{3.34}$$

The transfer matrix

$$\mathcal{M}(\omega) = \left(\begin{array}{cc} m_{11}(\omega) & m_{12}(\omega) \\ m_{21}(\omega) & m_{22}(\omega) \end{array} \right), \tag{3.35}$$

for the entire N-layer system is then given by

$$\mathcal{M}(\omega) = \mathcal{D}_0^{-1} \left[\prod_{j=1}^{N-1} \mathcal{D}_j \mathcal{P}_j \mathcal{D}_j^{-1} \right] \mathcal{D}_N, \tag{3.36}$$

47

where $\mathcal{D}_0$ is the dynamical matrix for free space and $\mathcal{D}_N$ is that for the substrate material (muscle in the biological case) and will have no left moving wave.

From the transfer matrix $\mathcal{M}$ the inverse problem presents as

$$\mathcal{M}_{inv} = \mathcal{D}_N^{-1} \left[\prod_{j=1}^{N-1} \mathcal{D}_{N-2+j} \mathcal{P}_{N-2+j} \mathcal{D}_{N-2+j}^{-1} \right] \mathcal{D}_0, \tag{3.37}$$

where now the substrate in the forward case is the incident medium in the inverse case, and the incident medium in the forward case is now the substrate in the inverse case. Using the identity that the *transpose of a matrix product* is the product of the transposes in *reverse order* as

$$(\mathcal{ABC})^T = \mathcal{C}^T \mathcal{B}^T \mathcal{A}^T, \tag{3.38}$$

allows to reverse the order of matrix multiplication as

$$\mathcal{M}^T = \mathcal{D}_N^T \left[\prod_{j=1}^{N-1} \mathcal{D}_j \mathcal{P}_j \mathcal{D}_j^{-1} \right]^T (\mathcal{D}_0^{-1})^T. \tag{3.39}$$

The right hand side of the expression in Eq. (3.39) differs from that in Eq. (3.37) by the inverse on the last time $(\mathcal{D}_0^{-1})^T$ and the lack of the inverse on the first term $\mathcal{D}_N^T$. The knowledge of $\mathcal{M}$ solely does not allow for straight forward computation of the inverse problem as no inverse or symmetry relations exist, in general, for the transfer matrix $\mathcal{M}$. This transfer matrix also provides the Fresnel reflection and transmission coefficients as $r = m_{21}/m_{11}$ and $t = 1/m_{11}$, respectively.

The frequency dependence of the Fresnel coefficients for a layered biological system of skin, fat, and substrate muscle, as illustrated in Fig. 3.2, whose dispersive properties are shown in Figs. 2.2–2.4, is illustrated in Fig. 3.3. Notice that the passband in the biological system presented here is centered about $f \simeq 600\text{MHz}$. The reflected $\tilde{\mathbf{E}}_r$ and transmitted $\tilde{\mathbf{E}}_t$ field vectors are then expressed as

$$\tilde{\mathbf{E}}_r(z = 0, \omega) = r(\omega)\tilde{\mathbf{E}}_0 (\mathbf{r}, \omega), \tag{3.40}$$

$$\tilde{\mathbf{E}}_t (z_{N-1}, \omega) = t(\omega)\tilde{\mathbf{E}}_0 (\mathbf{r}, \omega), \tag{3.41}$$
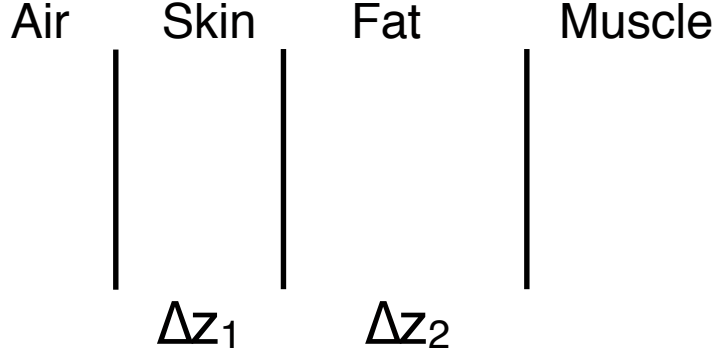
Figure 3.2: Biological multilayer with layer thicknesses Δz_1, Δz_2 and semi-infinite substrate of muscle.

where

$$z_{N-1} = \sum_{j=1}^{N-1} \Delta z_j, \tag{3.42}$$

and where $\tilde{\mathbf{E}}_0 (\mathbf{r}, \omega)$ is the temporal Fourier transform of the incident field $\mathbf{E}_0 (\mathbf{r}, t)$. The reflected field given is present at the air-skin interface while the transmitted field is present at the fat-muscle interface. Upon taking the inverse temporal Fourier transform of Eq. (3.40) one obtains either the time-harmonic reflected

$$\mathbf{E}_r (\mathbf{r}, t) = \frac{1}{2\pi} \int \tilde{\mathbf{E}}_r (\mathbf{r}, \omega) e^{-\imath \omega t} d\omega, \tag{3.43}$$

and the time-harmonic transmitted field as

$$\mathbf{E}_t (\mathbf{r}, t) = \frac{1}{2\pi} \int \tilde{\mathbf{E}}_t (\mathbf{r}, \omega) e^{-\imath \omega t} d\omega. \tag{3.44}$$

The dependence of the dispersion curves for the Fresnel reflection (solid curves) and transmission (dashed curves) coefficients of an anatomical multilayer system with $N = 3$ on the thickness of Δz_2 is illustrated in Fig. 3.4. The propagation distance Δz_2 in the second layer (fat) is varied from $\Delta z_2 = 0$ to $\Delta z_2 = \lambda$ in quarter wavelength increments. As suggested by the preceding analysis, as the propagation distance in the second layer is increased, the pass-band of the multi-layer system is down-shifted.
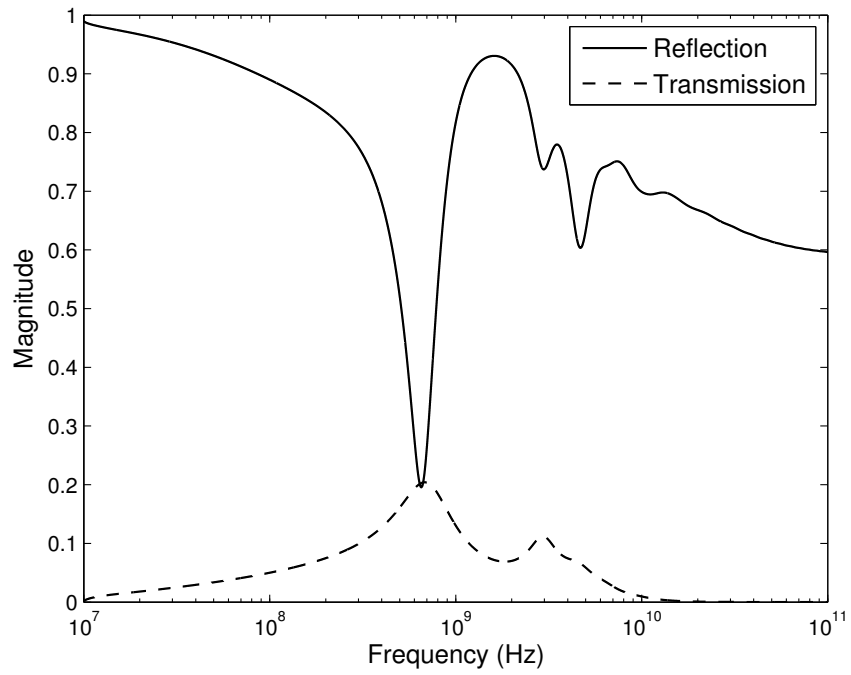
Figure 3.3: Frequency dependence of the complex Fresnel reflection (solid) and transmission (dashed) coefficients for a layered biological system of skin ($\Delta z_1 = 5$mm), fat ($\Delta z_2 = 20$mm) and semi-infinite substrate muscle.
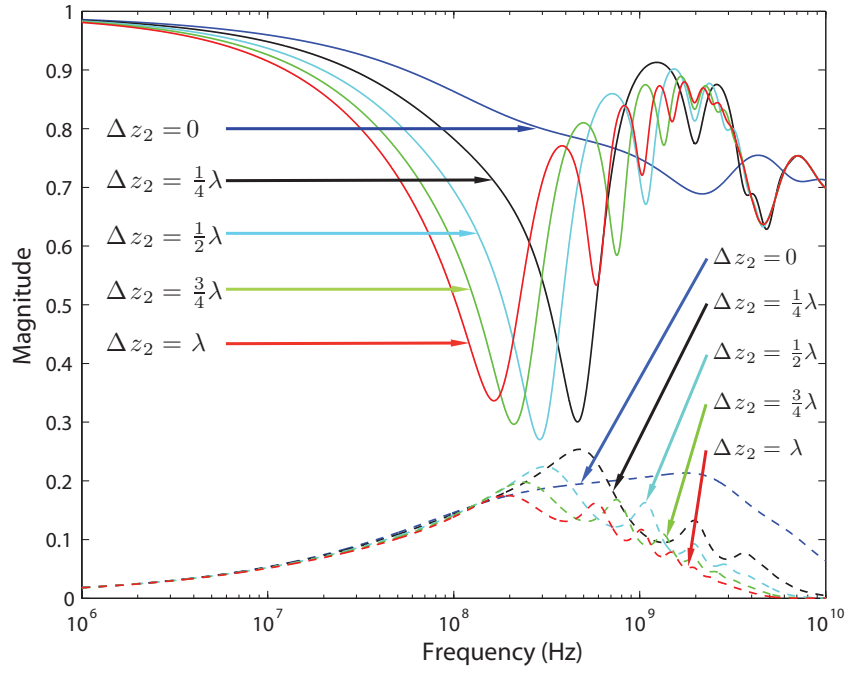
Figure 3.4: Magnitude of the Fresnel reflection, at the air-skin interface, (solid curves) and transmission, at the fat-muscle interface, (dashed curves) coefficients at 1GHz in fat where $\lambda \sim 12.5$cm.

3.3 Quarter-Wave Layer with a Radar Absorbing Material

The effects of material dispersion on the reflected electromagnetic wave field due to an incident ultrawideband pulse on a multilayer dielectric stack is presented for the particular case when the system contains a single layer of finite thickness Δz placed on top of a perfect electric conductor (PEC), as illustrated in Fig. 3.5. The *Salisbury Screen* (Salisbury 1952) shows the first time that this interference pattern was constructed in order to reduce the reflection from a radar system. The nonmagnetic ($\mu = \mu_0$), nonconducting ($\sigma = 0$) dielectric layer is assumed to be highly absorptive, and thus highly dispersive, as might be found
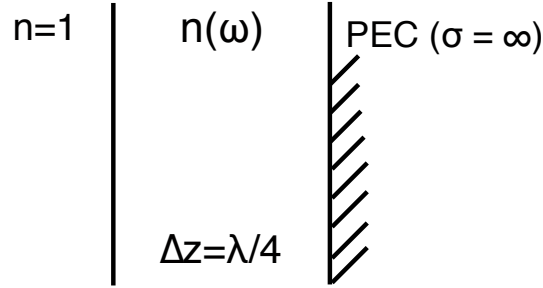
Figure 3.5: Quarter-wave plate ($\Delta z = \lambda/4$) on perfect electric conductor (PEC) substrate.

in a radar absorbing material (RAM), with a frequency dependent complex permittivity $\epsilon(\omega)$ and complex refractive index $n(\omega) = (\epsilon(\omega)/\epsilon_0)^{1/2} = n_r(\omega) + \imath n_i(\omega)$ described by the Rocard-Powles extension (McConnel 1980) of the Debye model (Debye 1929) of orientational polarization. The hypothetical radar absorbing material is designed to have an e^{-1} absorption depth $z_d \equiv c/(\omega_c n_i(\omega_c))$ equal to a wavelength $\lambda = (2\pi c)/(\omega_c n_r(\omega_c))$ at the input pulse carrier frequency $\omega_c = 2\pi f_c$, and the thickness of the layer Δz is nominally chosen at a quarter wavelength at the carrier frequency and varied up to a wavelength, where the incident and reflected pulses are in vacuum. Numerical examples are presented here for an incident rectangular enveloped pulse of time duration T that is chosen to be either ultrashort (a single cycle) or long (many cycles) in order to investigate the effects of destructive interference on the reflected steady-state component. The reflected signal is shown to contain multiple pulses from the repeated reflections inside the dielectric layer

with the multiple reflected pulses connected in time since the layer's thickness is on the order of or less than a wavelength. The Brillouin precursor is known to dominate the signal as twice the layer thickness $2\Delta z$ increases above z_d and may then be used to detect the low observable surface.

The analysis of the *quarter wave plate* is a classic problem in optics (Born and Wolf 1980) with direct application to *antireflection coatings*. The *reflectivity* $\mathcal{R} = |r|^2$ of an interface is a measure of the power reflected from that surface and relates to the energy density

$$\mathcal{U}_{em}(\mathbf{r}, t) = \frac{1}{2}\left(\epsilon E^2(\mathbf{r}, t) + \mu H^2(\mathbf{r}, t)\right). \tag{3.45}$$

where $\tilde{\mathbf{H}}^*(\mathbf{r})$ is the complex conjugate of the magnetic intensity vector. The energy density per unit area incident upon the interface for a time harmonic field at normal incidence in vacuum (satisfied in all cases presented here) is given by

$$\mathcal{U}_i = |A|^2, \tag{3.46}$$

where A is the amplitude of the time harmonic wave and the subscript i denotes incident. The energy densities reflected and transmitted from the boundary are then given, respectively, by (Born and Wolf 1980)

$$\mathcal{U}_r = |R|^2, \tag{3.47}$$

$$\mathcal{U}_r = \epsilon_2(\omega)|T|^2, \tag{3.48}$$

where $\epsilon_2(\omega)$ is the (real-valued) dielectric permittivity in the second medium. When $\epsilon_2(\omega)$ is complex-valued (as required when medium 2 is attenuative) the energy density of the transmitted field looses physical meaning, as such this description is only applicable when the substrate is purely real. The ratios of these quantities

$$\mathcal{R} = \frac{\mathcal{U}_r}{\mathcal{U}_i} = \frac{|R|^2}{|A|^2} = |r|^2, \tag{3.49}$$

$$\mathcal{T} = \frac{\mathcal{U}_t}{\mathcal{U}_i} = \epsilon_2(\omega)\frac{|T|^2}{|A|^2} = \epsilon_2(\omega)|t|^2, \tag{3.50}$$

are respectively known as the *reflectivity* and *transmissivity*.

The reflectivity of the three layer system is most generally expressed as

$$\mathcal{R} = \frac{r_{01}^2 + r_{12}^2 + 2r_{01}r_{12}\cos(2\beta)}{1 + r_{01}^2 r_{12}^2 + 2r_{01}r_{12}\cos(2\beta)}, \tag{3.51}$$

where $\beta = 2\pi/\lambda_0 n_1 \Delta z$ for normal incidence and, for a purely real substrate, $\Im\{\epsilon_2(\omega)\} \equiv 0$. For a system of three layers the reflection coefficients, at normal incidence, for the interface separating the first and second media, and the second and third are respectively

$$r_{01} = \frac{n_0 - n_1}{n_0 + n_1}, \tag{3.52}$$

$$r_{12} = \frac{n_0 - n_2}{n_1 + n_2}, \tag{3.53}$$

where n_0, n_1, and n_2 are refractive indices for the incident, second, and substrate medium respectively. As such, the reflectivity for the system is expressed as

$$\mathcal{R} = \left(\frac{n_0 n_2 - n_1^2}{n_0 n_2 + n_1^2}\right)^2. \tag{3.54}$$

When the middle layer has a thickness given by

$$\Delta z = \frac{\lambda_0}{2\cos\theta_1}, \; \frac{2\lambda_0}{2\cos\theta_1}, \; \frac{3\lambda_0}{2\cos\theta_1}, \; ..., \tag{3.55}$$

then $\cos(2\beta) = 1$ and the reflectivity for the system is then found to be independent of n_1 as (Born and Wolf 1980)

$$\mathcal{R} = \left(\frac{n_0 - n_2}{n_0 + n_2}\right). \tag{3.56}$$

The maxima and minima of $\mathcal{R}(\Delta z)$ are found by differentiation of Eq. (3.51) with respect to Δz and occur when $\Delta z = m\lambda_0/4$ ($m = 1, 2, 3, ...$). A second differentiation then provides the condition for a minimum of $\mathcal{R}$ when $d^2\mathcal{R}/d\Delta z^2 < 0$, showing that for a system with $n_1 > n_2$, the reflectivity $\mathcal{R}$ is minimized for $\Delta z = m\lambda_0/4$ ($m = 1, 3, 5..$), and in the case of $n_2 < n_3$ $\mathcal{R}$ is minimized when $\Delta z = m\lambda_0/4$ ($m = 2, 4, 6..$).

An idealized hypothetical case of a quarter-wave plate is obtained when the incident and transmitted media are characterized by vacuum with $n(\omega) = 1 \; \forall \; \omega$ and the permittivity of

54

the quarter-wave plate is purely real but dispersive. In that case, one may use the Debye model to describe $\epsilon_r(\omega)$ as

$$\frac{\epsilon_r(\omega)}{\epsilon_0} = \epsilon_\infty + \frac{\epsilon_{sr} - \epsilon_\infty}{1 + \omega^2\tau^2}, \tag{3.57}$$

with the parameters $\epsilon_s = 10$, $\epsilon_\infty = 1$, and $\tau = 1 \times 10^{-10}$s which provide sets the absorption depth $z_d = \alpha^{-1}(\omega_c) = 2.52$cm at $\omega_c = 1.26 \times 10^{10}$r/s if loss is included, while artificially setting $\epsilon_i(\omega) \equiv 0$. In the case considered, the reflected field from the back interface is in perfect destructive interference with the reflected field from the first interface due to the $\pi/2$ phase shift when $\Delta z = \lambda_0/4$ where $\lambda_0 = c/f = 15$cm is the vacuum wavelength for $f = 2$GHz. The frequency dependence of the Fresnel reflection coefficient r is shown in Fig. 3.6 where it is seen that r vanishes at the isolated frequency ω_c. However, due to dispersion the subsequent zeros of the reflection coefficient are not at the locations predicted by the monochromatic analysis, but in this case are up-shifted from them.
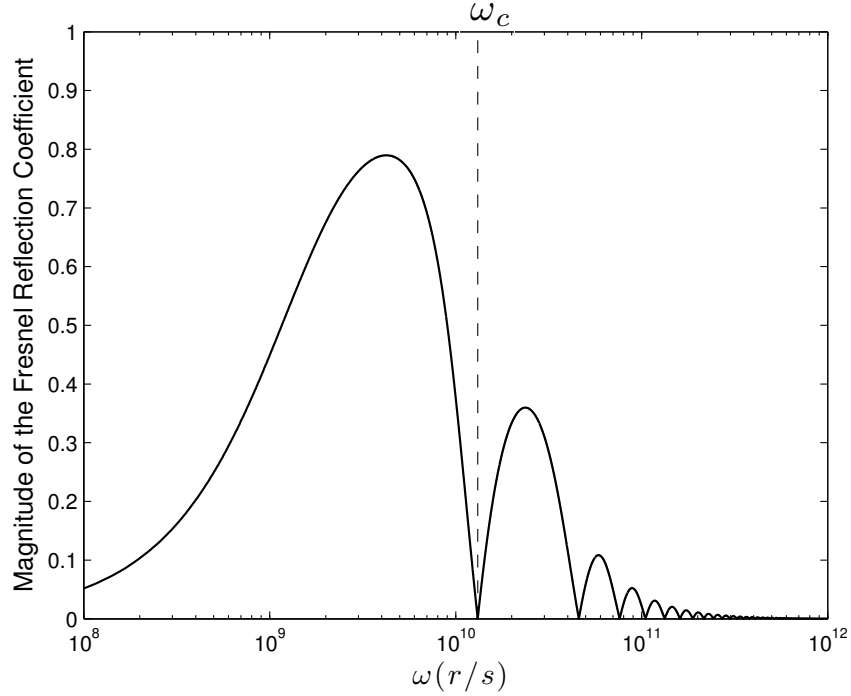
Figure 3.6: Magnitude $|r|$ of the frequency dependent Fresnel reflection coefficient at normal incidence for a $\lambda/4$ wave plate.

The magnitude of the Fresnel reflection coefficient for the specific frequency $\omega = 1.26 \times$

10^{10}r/s vanishes completely, thereby entirely extinguishing this component of the field in the steady state, continuous wave case, as shown in Fig. 3.7. The incident pulse $f(t) = u(t)\sin(\omega_c t)$ (solid curve) where $\omega_c = 1.26 \times 10^{10}$r/s, $u(t) = 0$ for $t < 0$ and $t > T$ and $u(t) = 1$ for $0 < t < T$. Notice that is rectangular envelop pulse can be represented as the difference between a pair of time delayed Heaviside step-function signals. The numerically determined reflected field, described by the solid curve in Fig. 3.7, is seen to have no steady state component, as expected from the usual continuous wave analysis of a quarter-wave plate (Born and Wolf 1980). The continuous wave analysis assumes a purely monochromatic incident field that is oscillating for all time. For a finite duration rectangular envelope wave-field, however, there are large leading and trailing edge transients evident in the reflected field depicted in Fig. 3.7.
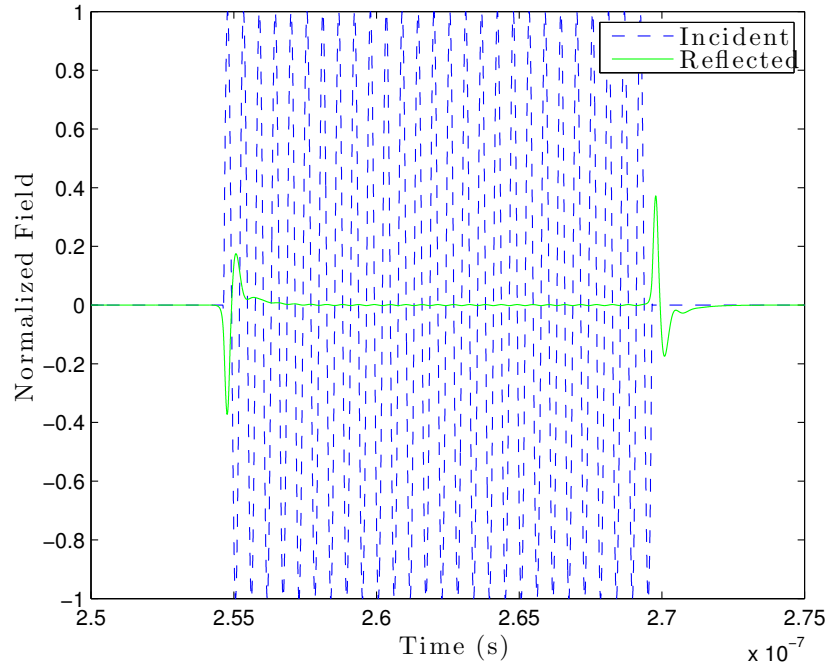
Figure 3.7: Incident (dashed) and reflected (solid) pulses from a fictitious non-absorbing, dispersive dielectric layer with incident and substrate mediums being vacuum.

When the associated dispersive loss is included by allowing the permittivity of the dielectric layer to be complex, the refractive index then being complex as well, the quarter

wave layer no longer provides a complete extinction of any frequency near the carrier ω_c as it did in the idealized case previously treated. Even when the incident and transmitted media are both vacuum, there is no frequency component in the bandwidth of interest whose Fresnel reflection coefficient vanishes. The effects of a dielectric whose loss cannot be ignored is then seen to fundamentally alter the continuous wave analysis of the quarter wave plate for perfect destructive interference.

Since the Debye model of orientational polarization overestimates the loss factor for high frequencies, use of this dispersion model will underestimate the magnitude of the Fresnel reflection coefficient (dashed curve) at high frequencies, as illustrated in Fig. 3.8. With the loss being improperly over-estimated by the Debye model, it then appears that the lossy layer absorbs more energy at higher frequencies than would be expected. This is corrected by using the Rocard-Powles extension (McConnel 1980) to the Debye model, as described by the solid curve depicted in Fig. 3.8.
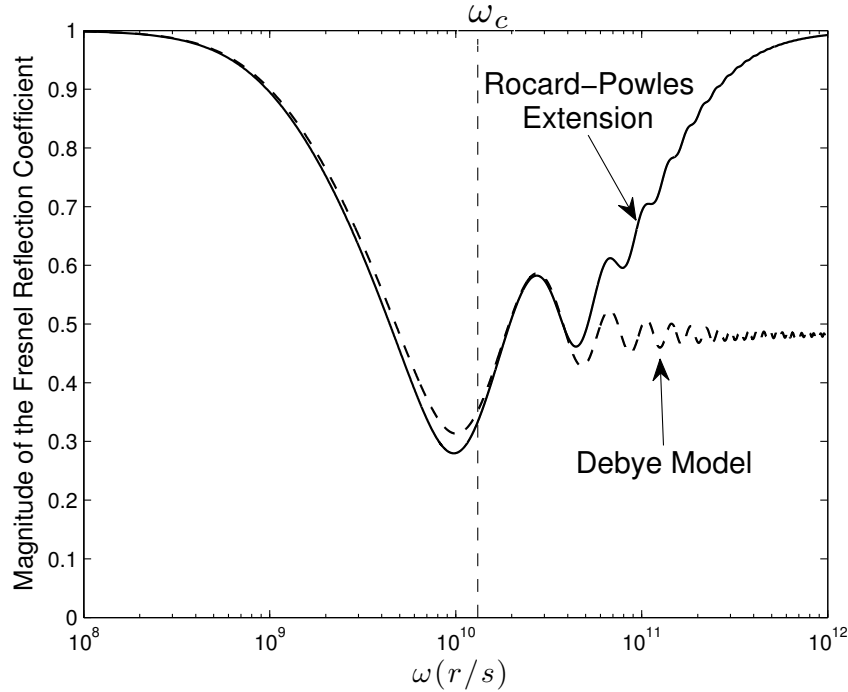
Figure 3.8: Resultant frequency dependent Fresnel coefficients for the Debye-model (dashed curve) and its Rocard-Powles extension (solid curve).

When the transmitted media is replaced by a good conductor, in this case modeled as aluminum with static conductivity $\sigma_0 = 2.82 \times 10^8$ S/m, all of the energy is reflected back into the dielectric layer since no field can be sustained within the conductor. Again, if loss was neglected throughout the system, all of the incident energy would be reflected back into the incident medium since there wouldn't be any transmission into the substrate nor would there be any loss in the system. By properly modeling the dispersive dielectric layer as having causally related dispersive loss in the neighborhood of the carrier frequency ω_c by including the full Rocard-Powles-Debye dispersion model given in Eq. (2.54), viz.

$$\frac{\epsilon(\omega)}{\epsilon_0} = \epsilon_\infty + \frac{\epsilon_{sr} - \epsilon_\infty}{(1 - \imath\omega\tau)(1 - \imath\omega\tau_f)}, \tag{3.58}$$

good, but not total, extinction is achieved for a narrow frequency band about the carrier frequency $\omega_c = 1.26 \times 10^{10}$r/s, as illustrated Fig. 3.8. Notice that the minimum in this block-band filter is down-shifted from its design point at ω_c. The numerically determined reflected pulse, illustrated in Fig. 3.9, is seen to possess both transient and steady state components.

3.4 Propagation Through Stratified Media

The asymptotic description of ultrawideband dispersive pulse propagation is obtained from the exact Fourier-Laplace integral representation of the propagated linearly polarized plane wave field (Sommerfeld 1914; Brillouin 1914; Brillouin 1960)

$$E(z,t) = \frac{1}{2\pi} \int_{ia-\infty}^{ia+\infty} \tilde{f}(\omega) e^{\frac{z}{c}\phi(\omega,\theta)} d\omega, \tag{3.59}$$

for $z \geq 0$. Here a is a number larger than the abscissa of absolute convergence (Stratton 1941) for the spectrum $\tilde{f}(\omega) = \int_{-\infty}^{\infty} f(t) e^{i\omega t} dt$ of the initial plane wave pulse $E(0,t) = f(t)$ at $z = 0$. The temporal Fourier spectrum $\tilde{E}(z,\omega)$ of the wave field $E(z,t)$ satisfies the Helmholtz equation $\left(\nabla^2 + \tilde{k}^2(\omega)\right) \tilde{E}(z,\omega) = 0$ with *complex wave number* $\tilde{k}(\omega) = \beta(\omega) + i\alpha(\omega) = (\omega/c)n(\omega)$ in the temporally dispersive medium with *complex index of refraction*
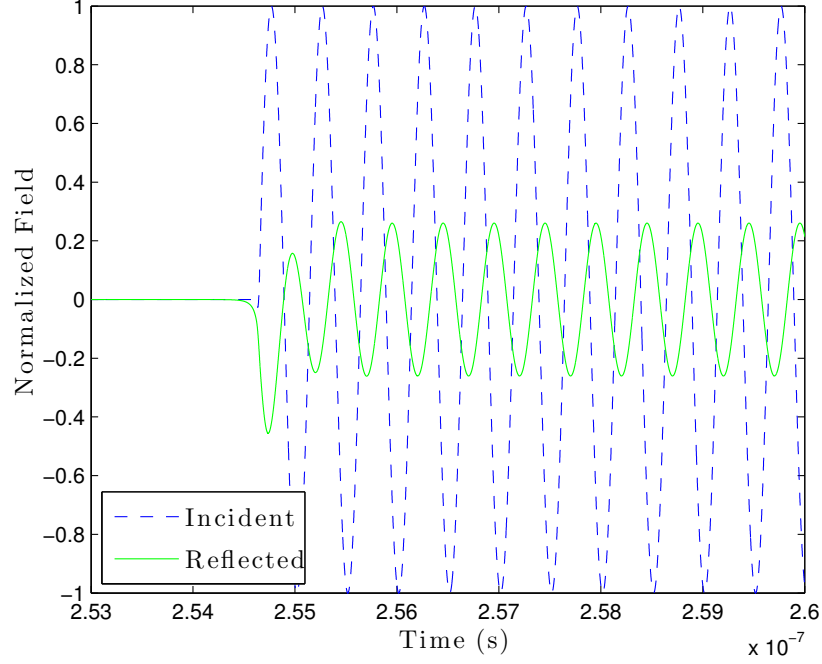
Figure 3.9: Incident (dashed) and reflected field (solid) from $\lambda/4$ RAM on PEC.

$n(\omega) = n_r(\omega) + in_i(\omega)$ whose real $n_r(\omega) \equiv \Re\{n(\omega)\}$ and imaginary $n_i(\omega) \equiv \Im\{n(\omega)\}$ parts are related through the Kramers-Kronig relations. Here $\beta(\omega) \equiv \Re\left\{\tilde{k}(\omega)\right\}$ is the *propagation (or phase) factor*, $\alpha(\omega) \equiv \Im\left\{\tilde{k}(\omega)\right\}$ is the *attenuation factor*, and

$$\phi(\omega, \theta) \equiv i\frac{c}{z}\left[\tilde{k}(\omega)z - \omega t\right] = i\omega\left[n(\omega) - \theta\right] \tag{3.60}$$

is the complex phase function with $\theta \equiv ct/z$ a nondimensional space-time parameter defined for all $z > 0$.

For $\theta \geq 1$, the propagated wave field due to an ultrawideband signal in a Rocard-Powles-Debye model dielectric may be expressed either as a superposition of component fields as $E(z, t) = E_B(z, t) + E_c(z, t)$, or as a linear combination of fields of this form. Here $E_B(z, t)$ is the Brillouin precursor describing the low-frequency response, and $E_c(z, t)$ is the pole contribution describing the signal contribution (if any). Of particular significance here is that the peak amplitude of the Brillouin precursor $E_B(z, t)$ experiences zero exponential decay with propagation distance $z > 0$, decreasing algebraically as $z^{-1/2}$ in the dispersive,

absorptive medium (Oughstun 2005).

In addition to having a proper description of reflection and transmission at a lossy interface, as well as through a multilayer system of dispersive media, a complete and accurate description of biological tissues is necessary to model this interaction. The energy of the propagated field depends upon both the transmission across each material interface as well as through each dispersive, attenuative layer (labeled $j = 1, 2, ..., N$), where each medium is described by its complex refractive index $n_j(\omega)$. This numerical simulation consists of three stacked biological tissues ($N = 3$) representing skin, fat and muscle with each interface assumed to be planar and infinite in the transverse direction. Each tissue is modeled as a homogeneous, isotropic, linear, dispersive lossy dielectric whose frequency dependence follows a multiple relaxation-time Rocard-Powles-Debye model over a wideband frequency range extending from static to 10GHz.

Because each of the materials are described by a complex dielectric permittivity, the Fresnel reflection and transmission coefficients for all cases presented will be complex, effecting both the amplitude and phase of the incident plane wave. It is common in most literature to make the angle of refraction θ_2 with respect to the normal complex-valued as described by Snell's law (Descartes 1644)

$$\sin^{-1}\left(\frac{n_1 \sin\theta_1}{n_2}\right) = \theta_2, \tag{3.61}$$

where θ_1 is the deviation from normal for the incident field, and n_1 and n_2 are the refractive indices for the incident and transmitted mediums, respectively, which in general are complex functions as shown in §3.2. However, as described by Roy (Roy 2003) this result looses physical meaning when θ_2 becomes a complex quantity. In addition, Snell's law has been extended to stratified media for both the periodic and aperiodic case (Born and Wolf 1980) and can be represented in a similar matrix used here for the complex frequency dependent Fresnel coefficients.

3.4.1 A Heuristic Example

As an example, consider a single dispersive dielectric layer $(N = 3)$ where the incident and substrate layers are both vacuum, and the middle layer is triply-distilled water with thickness $\Delta z = 12$cm. The frequency dispersion of triply-distilled water below 500GHz is accurately represented as a double relaxation time Rocard-Powles-Debye model described in Eq. (2.59). The numerical example treated here examines the transmitted and reflected wave fields due to an incident single cycle rectangular envelope pulse $f(t) = u(t)\sin{(2\pi f_c t)}$ with $f_c = 1$GHz, where $u(t) = 0$ for $t < 0$ and $t > T$ and $u(t) = 1$ for $0 < t < T$. Again, notice that a rectangular envelope pulse can be represented as the difference between a pair of time delayed Heaviside step-function signals. With this pulse normally incident on this multilayer system, a transmitted pulse train is observed at the output in medium 3, as shown in Fig. 3.10. Notice that each subsequent pulse amplitude is attenuated by two mechanisms, the first being due to reflection of energy back into the incident medium and the second being caused by the dielectric loss of the water layer. The broadening of each pulse is due to the frequency dispersion within the layer of water. The reflected pulse train (dashed curve) is illustrated in Fig. 3.11.

3.4.2 Multilayer System

When the number of layers is increased $(N > 3)$ so that there is more than one layer of finite thickness, the dynamics of the multiple reflections and transmissions in the system become more complex. As an example, consider the $N = 4$ system where the first medium is vacuum, the second medium is skin with thickness $\Delta z_2 = 5$mm, the third is fat with thickness $\Delta z_3 = \frac{1}{4}\lambda \sim 3.1$cm, and the semi-infinite substrate material is muscle, as illustrated in Fig. 3.2, where the propagation direction is orthogonal to the orientation of the muscle fibers. The same input rectangular envelope pulse used in the previous example is normally incident on this multilayered system and is shown along with the series of output pulses at the back interface in Fig. 3.12. Here the output pulses are continuously connected in time
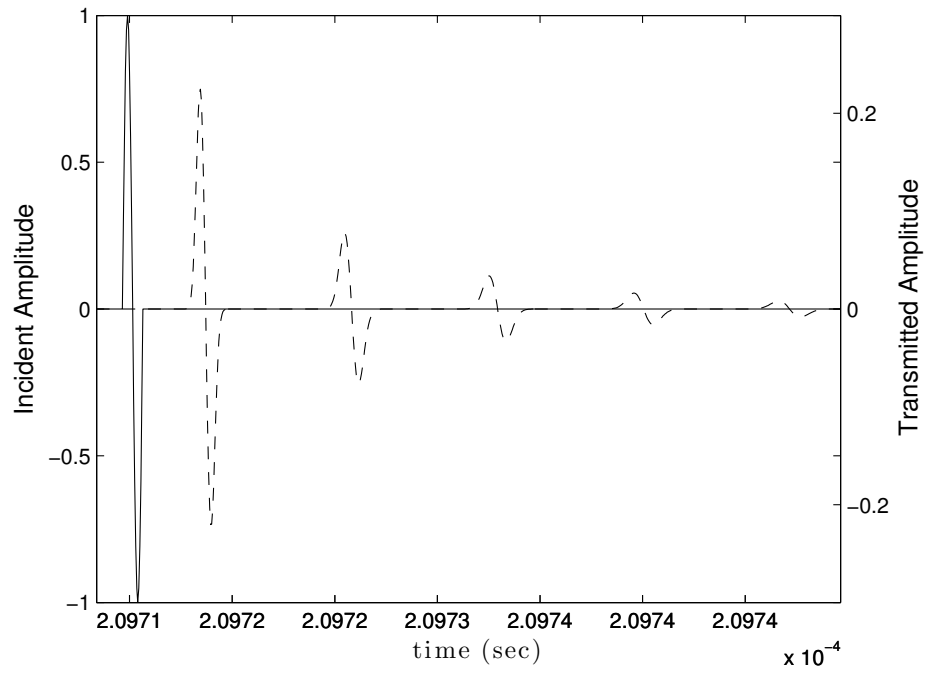
Figure 3.10: Incident single-cycle pulse (solid curve) and transmitted pulses (dashed curve) at the back interface.
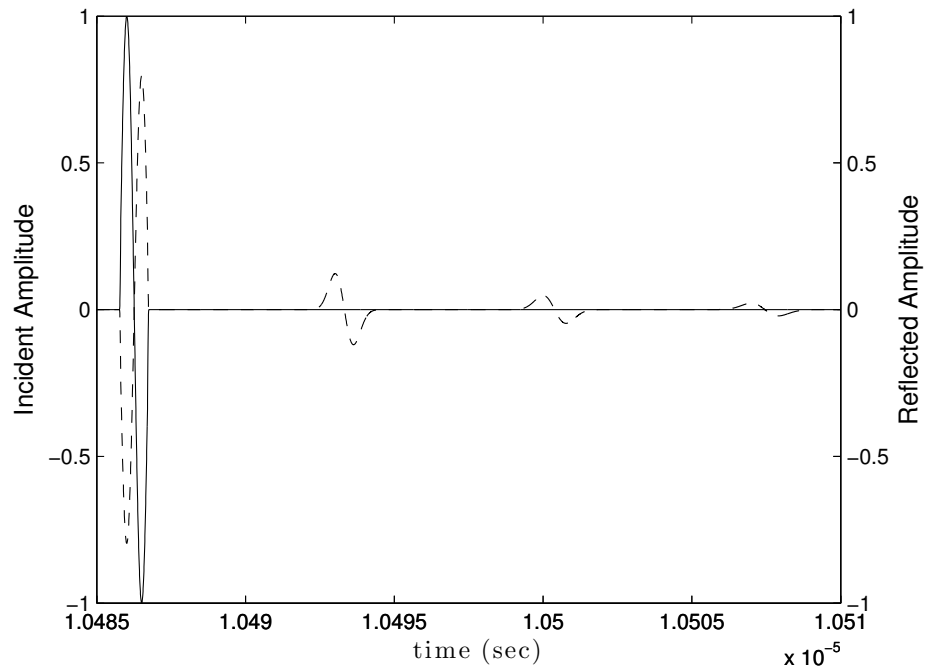
Figure 3.11: Incident single-cycle pulse (solid curve) and reflected pulses (dashed curve) at the initial interface.

because the thickness of any one layer, excluding the substrate, is shorter than a wavelength.
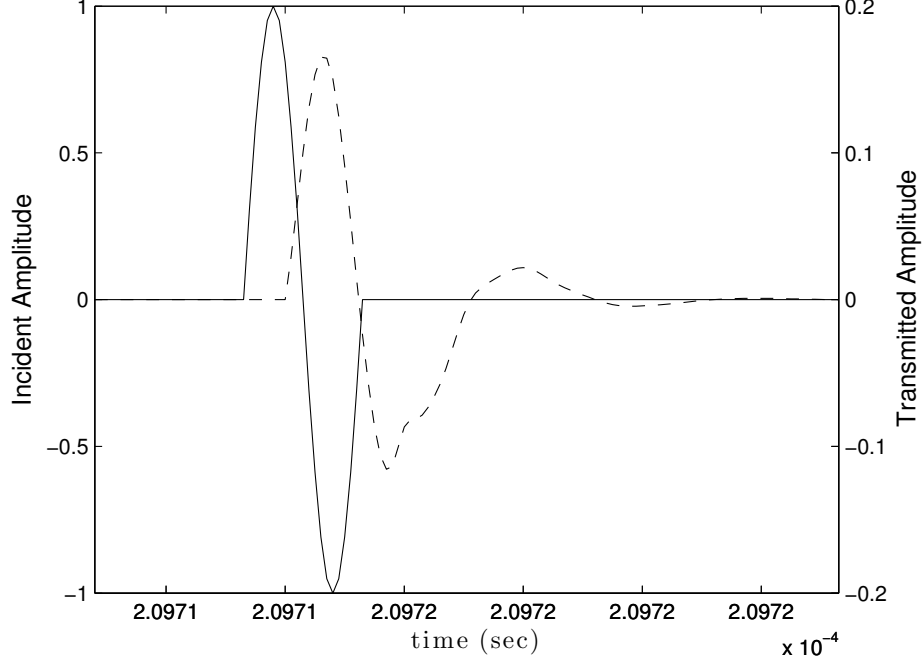
Figure 3.12: Incident single-cycle pulse (solid curve) and superposed transmitted pulses (dashed curve) at the back interface.

This transmitted pulse is then propagated in the muscle substrate material where the pulse is seen to dynamically evolve due to the frequency dependent phase and attenuation factors. The peak amplitude of the transmitted pulse at the back interface is reduced to 16.5% of the incident pulse amplitude. According to Beer's law, this pulse should then be attenuated by the factor $e^{-5} \sim 0.0067$ to a peak amplitude of $\sim 1.1 \times 10^{-3}$ at five absorption depths $[z/z_d = 5$, where $z_d = \alpha(\omega_c)^{-1} \sim 4.6\text{cm}]$ Fig 3.13 illustrates the multilayer system and the plane where the *measurement* is made. However, because of the nonexponential decay of the Brillouin precursor (Oughstun 2005), the propagated pulse, illustrated in Fig. 3.14, has a peak amplitude that is more than an order of magnitude larger.

A comparison of the numerically determined peak amplitude attenuation of this pulse at $z/z_d = 1, 2, ..., 10$ is made with the exponential attenuation described by Beer's law in

63
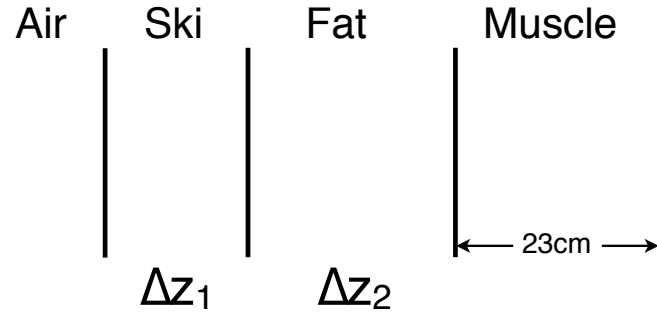
Figure 3.13: Biological multilayer with the *measurement* plane (dashed line) shown.
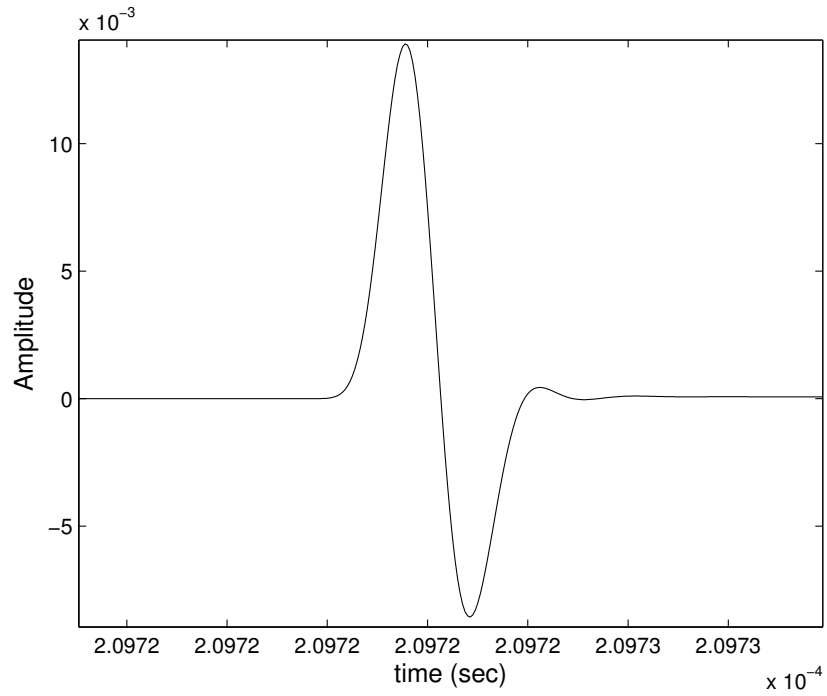
Figure 3.14: Transmitted pulse propagated 5 absorption depths ($\Delta z = 23$cm) into muscle.

64

Fig. 3.15. The numerical results exhibit the algebraic, nonexponential decay that is a characteristic of the Brillouin precursor evolution. Another feature of the Brillouin precursor is the change in its *effective oscillation frequency* with propagation distance, as the propagation distance approaches infinity the effective oscillation frequency of the precursor field approaches 0Hz. This is a characteristic of attenuative, dispersive media, signifying that biological tissues can demodulate radio and microwave frequency fields.
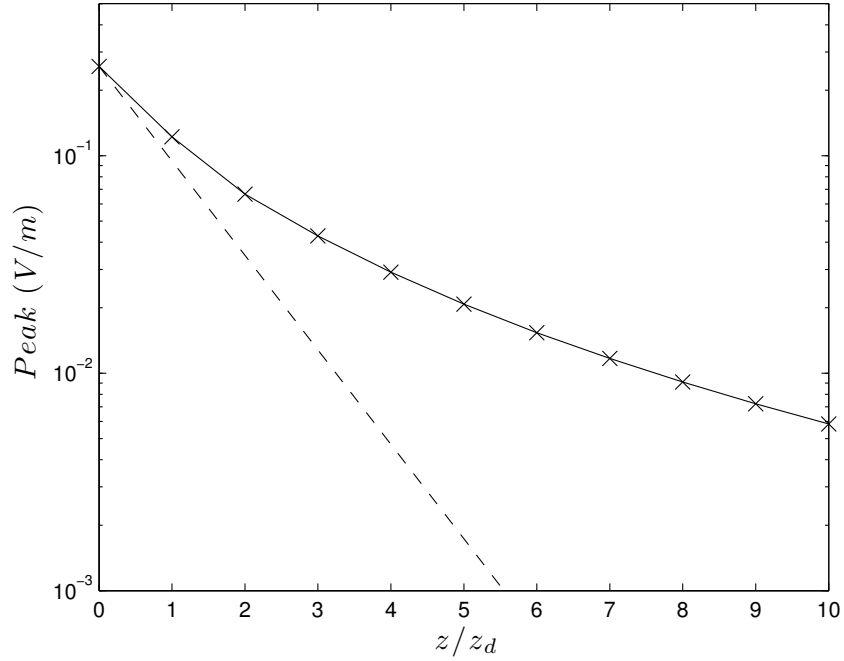
Figure 3.15: Numerically determined peak amplitude decay of a single cycle, rectangular envelope pulse (solid curve) with the corresponding Beer's law exponential decay (dashed curve) in substrate muscle, and where 'x' indicates a discrete data point from the simulation.

3.5   Conclusion

This formalism provides the necessary theoretical description required to properly analyze the interaction of an ultrawideband electromagnetic pulse with a layered, lossy, dispersive system. The canonical case of a quarter-wave plate has been analyzed where the antireflection film's loss is maximized at the carrier frequency and consequently the material is highly

dispersive in that frequency band. The effects of loss and dispersion on the quarter-wave plate analysis have been demonstrated numerically and show that complete extinction of the field is not achieved as it is in the classical nondispersive, nonabsorbtive analysis. The changes an ultrawideband electromagnetic pulse experiences as it is propagated through a layered system of simulated biological tissues have been described. Each layer is described as being homogeneous, isotropic and locally linear with temporal dispersion exhibiting orientational polarization described as a semi conducting Debye-type dielectric. The transmitted pulse in the biological substrate of muscle is found to contain multiple pulses due to the internal series reflections of the multilayer stack. All reflection coefficients presented here at the initial interface $z = 0$, and all transmission coefficients are for the plane $z = z_{N-1}$ given in Eq. (3.42). The resultant transmitted ultrawideband pulse does not decay exponentially as suggested by Beer's law, but rather algebraically, a characteristic of the Brillouin precursor that begins its formation in the dispersive, attenuative multilayer stack.

Chapter 4

Scattering, Breakdown and
Excitation of the Spherical Cell

4.1 Introduction

The analysis of an ultrawideband pulse incident on an anatomically realistic system of
layered biological tissues has been presented in previous chapters. That analysis provides a
correct description of the amount of the incident energy that can be transmitted through
the layered dispersive system into the biological substrate. Embedded in the substrate of
muscle is an idealized biological, spherical cell embedded in the substrate muscle whose
dispersive material properties are taken to be that of water. The numerical response of the
cell to the pulsed field is represented by the Fitzhugh-Nagumo model including both the
fast and slow response from the incident injected field.

The analysis presented here is concerned with transient phenomena associated with
pulsed fields in microwave and radio-frequency domains and its coupling at the cellular
level. This chapter aims to address the sparsity of research investigating the biological
interactions of *high-peak-low-average power* pulses as pointed out by Foster (Foster 2000).
Particularly of interest are pulses with rapid turn on times that exceed the relaxation times

of the biological tissues. When this criteria is met, precursor fields will be formed and carry energy further into the tissue than expected from the continuous wave case as described by Beer's law (Oughstun 2005).

The interactions of the propagated plane wave field with the spherical scatterer are carried out through the application of Rayleigh scattering, which is valid when the radius of the spherical cell is much less than the wavelength of the incident plane wave. The spherical cell is assigned the dispersive properties of water in order to determine the portion of energy injected across the cellular membrane. It is then this perturbation to the cellular membrane that is used with the Fitzhugh-Nagumo model for the excitable neuron show in Fig. 4.1 to investigate excitation. From the computations presented, the external field strengths required from excitation or breakdown of the cellular membrane are determined.
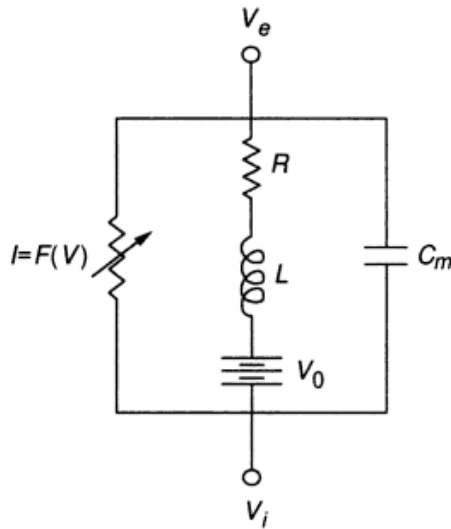
Figure 4.1: Fitzhugh-Nagumo model for the excitable neuron.

4.2 Scattering and Propagation In Tissues

In order to accurately describe the coupling of an ultrawideband pulse external to the body to internal tissues the pulse is passed through a system where the layers of skin and fat

are of finite thickness, respectively $\Delta z_1 = 5$mm and $\Delta z_2 = 20$mm, which are positioned on a semi-infinite substrate of muscle. Because of the finite thickness of the skin and muscle layer and their apparent macroscopic discontinuous changes in material parameters, repeated reflections are seen exiting the stack into the muscle as shown in Fig. 4.2, with 15% amplitude being transmitted through the multilayer stack, with the transmitted pulse containing multiple pulses continuously connected in time.
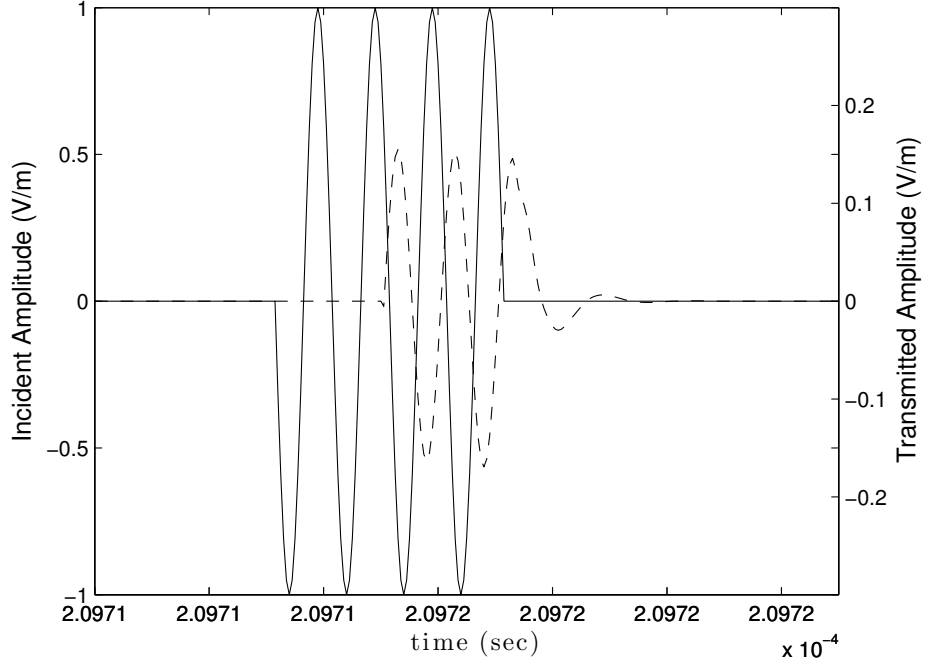
Figure 4.2: Incident (solid curve, left axis) and transmitted (dashed curve, right axis) pulse from the layered system.

After the transmitted pulse has been propagated a distance of $2z_d \sim 20$cm into muscle, where $z_d \equiv \alpha(\omega_c)^{-1}$, the frequency dependent phase $\beta(\omega)$ and attenuation $\alpha(\omega)$ factors fundamentally change the shape of the pulse with propagation distance. The resulting pulse is shown in Fig. 4.3 with the leading and trailing edge Brillouin precursors clearly evident in this propagated pulse. It is also obvious from this figure that the main signal component is attenuating at a much greater rate (with respect to distance) than the precursor fields.
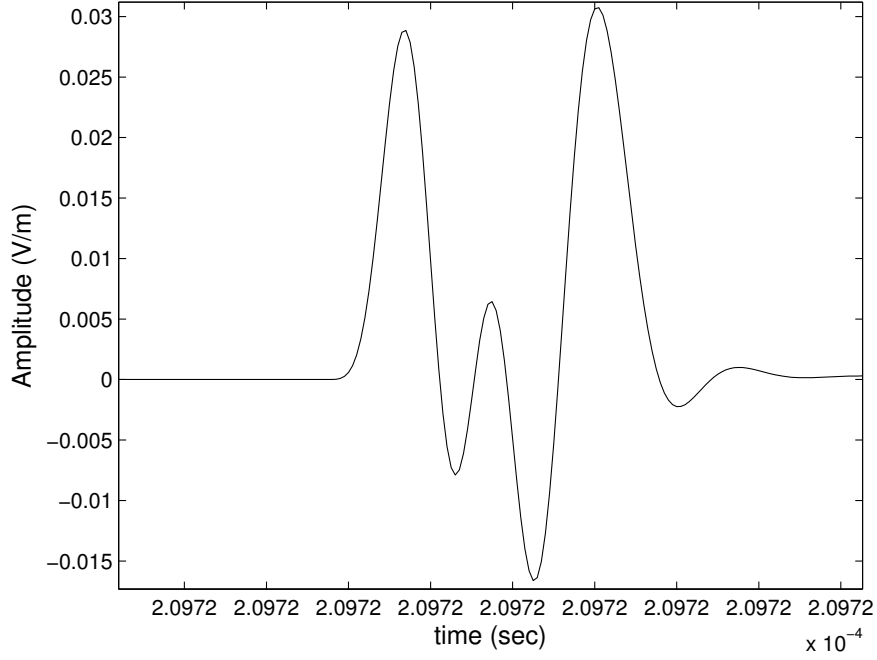
Figure 4.3: Pulse propagated $2z_d$ into muscle after being passed through the system shown in Fig. 3.2.

4.3 Scattering From the Cell

For the case of a biological cell, the wavelength λ of the incident electric field will be much larger than the radius of the spherical cell a. With this physical realization the entire exterior of the sphere will be at the same electric potential at every point in time. In this case the scattering from the sphere is described by Rayleigh scattering.

In Rayleigh scattering (Kerker 1969) the electric field inside the sphere $\tilde{\mathbf{E}}_i\left(\mathbf{r},\omega\right)$ is uniform and parallel to the external field $\tilde{\mathbf{E}}_o\left(\mathbf{r},\omega\right)$ with its amplitude modified as

$$\tilde{\mathbf{E}}_i\left(\mathbf{r},\omega\right) = \frac{3\epsilon_2(\omega)}{\epsilon_1(\omega) + 2\epsilon_2(\omega)}\tilde{\mathbf{E}}_o\left(\mathbf{r},\omega\right) \tag{4.1}$$

where $\epsilon_1(\omega)$ and $\epsilon_2(\omega)$ are the frequency dependent complex dielectric permittivities of the sphere and external medium, respectively. In the external medium two fields are superimposed, the first of which is the incident field $\tilde{\mathbf{E}}_0\left(\mathbf{r},\omega\right)$ which would exist even in the absence of the scattering sphere. The second field $\tilde{\mathbf{E}}_s\left(\mathbf{r},\omega\right)$ is the field which results from scatter-

ing due to the cell. This second field is that of a dipole being radiated from the spherical scatterer oriented parallel to the incident field. The dipole moment of this field is given by

$$\mathbf{p} = \epsilon_2(\omega) a^3 \frac{\epsilon_1(\omega) - \epsilon_2(\omega)}{\epsilon_1(\omega) + 2\epsilon_2(\omega)} \tilde{\mathbf{E}}_0 (\mathbf{r}, \omega). \tag{4.2}$$

The dipole field generated by the scattered is shown in Fig. 4.4 where the lines show the electric field lines and the contour fill shows the equipotential surfaces.
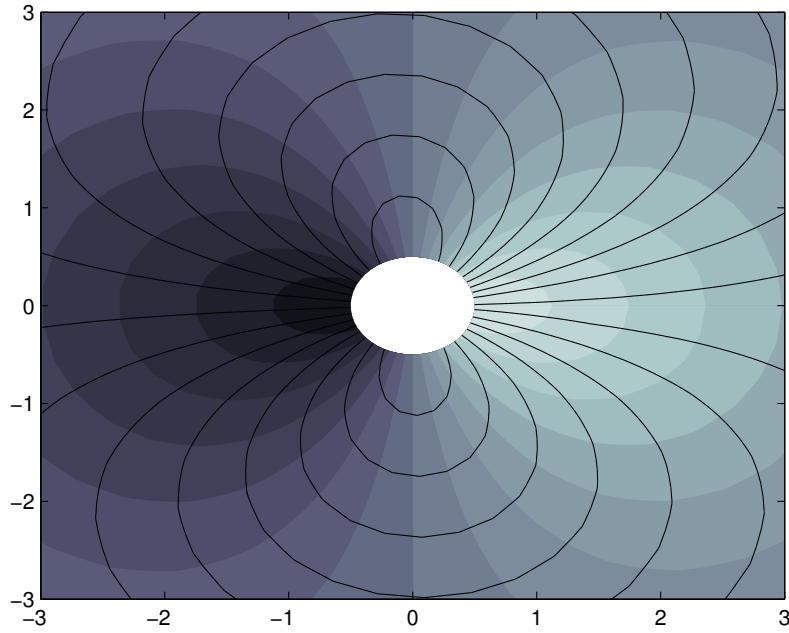
Figure 4.4: Dipole field generated by the spherical cell showing equipotential surfaces (shaded regions) and electric field lines (solid curves).

The *static zone* of the dipole radiation field is defined as $kr << 1$ so that $r << \lambda/2\pi$. In the static zone the equations for the electric and magnetic fields reduce to

$$\mathbf{E}(\mathbf{r}, t) \simeq -\frac{1}{4\pi\epsilon_0} \frac{p}{r^3} \left(2\cos\theta \hat{r} + \sin\theta \hat{\theta} \right) \cos(\omega t) \tag{4.3}$$

$$\mathbf{B}(\mathbf{r}, t) \simeq 0, \tag{4.4}$$

where p is the strength of the dipole moment. In the static zone the field is that due to that of an electrostatic dipole that varies with an $e^{\imath \omega t}$ time dependence as shown in Fig. 4.4.

71

Away from the spherical cell the scattered field has little contribution to the field in the external medium, due to its $1/r^3$ dependence (see Appendix D). The result of this condition is that sufficiently far away from the scatterer the electric field in the external medium will be that of the unperturbed incident field. The induced membrane potential is shown in Fig. 4.5 from the incident pulse described in Fig. 4.2. To achieve membrane breakdown, the membrane potential V_m is required to be on the order of $0.1-1$V for the incident, unity pulse presented here. The membrane potential is $9-10$ orders of magnitude below this threshold. For the model presented here it would require an incident pulse of 1×10^9V/m external to the body before cellular breakdown would be expected. The Precision Acquisition Vehicle Entry Phase Array Warning System (PAVE PAWS) radiates at published power densities upto 1.4μW/cm^2 which correspond to electrical field strengths on the order of 10^7V/m [(Barnes 2005) pp. 40].
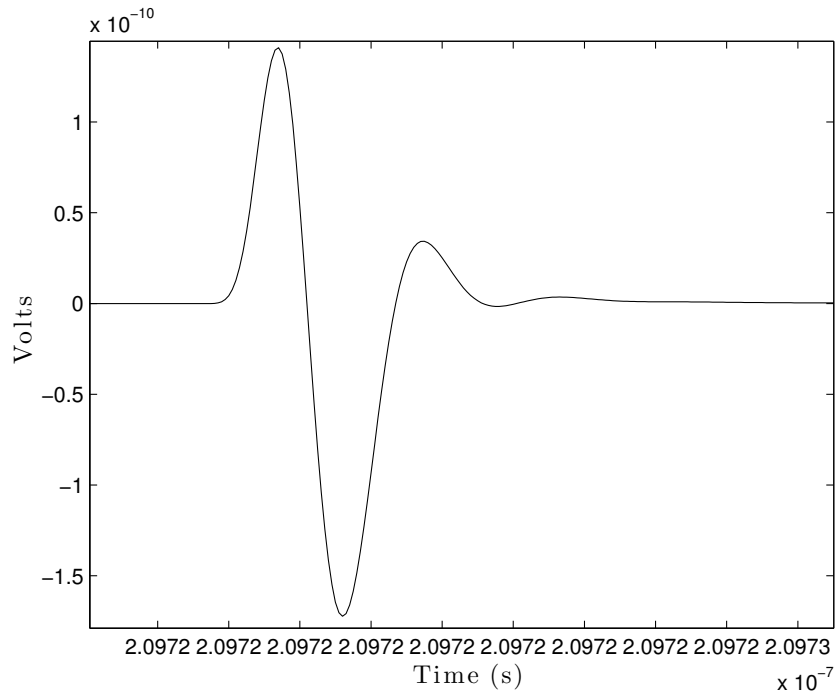
Figure 4.5: Induced change in membrane potential.

4.4 Excitation

The nonlinear circuit shown in Fig. 4.1 represents an excitable cell such as a neuron and is a simplified, two variable model of the Hodgkin-Huxley type with a fast variable V and a slow variable W. The slow variable W represents the current flowing through the resistor, inductor and battery and is called the *recovery current*, and the fast variable V_m is the membrane voltage. This two variable model is convenient for phase plane analysis.

There are three canonical responses from the Fitzhugh-Nagumo model, the first being when the input current I or membrane voltage V_m perturbation is below the necessary threshold in which no action potential is created by the dynamics as depicted in Fig. 4.6. The second case is when there is a single impulse that exceeds the cell's membrane threshold forcing a single action potential to be formed as depicted in Fig. 4.7. The final canonical response of this system is when the input is of sufficient strength to cause periodic spiking behaviors as shown in Fig. 4.8.
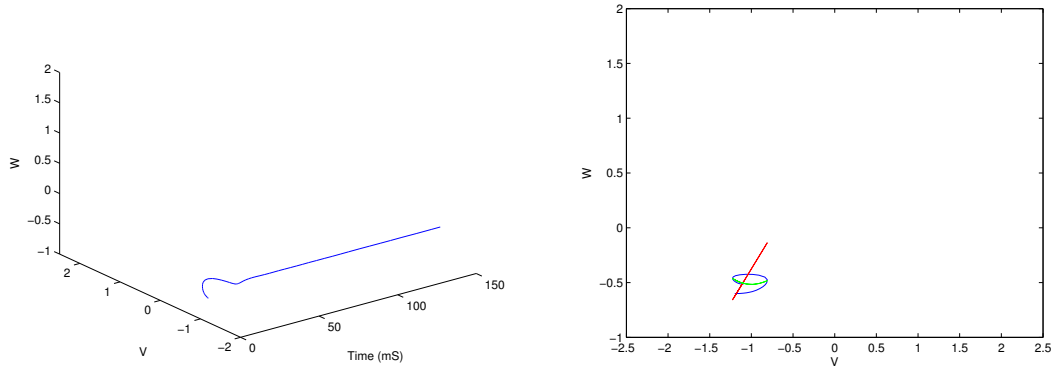
(a) Membrane potential and recovery current.   (b) Recovery potential vs membrane voltage.

Figure 4.6: Subthreshold example of the Fitzhugh-Nagumo model for $I = 0.16\mu$A.

Figures 4.6(a), 4.7(a), and 4.8(a) show a three dimensional representation of the recovery current W plotted against the membrane potential V in time t. The phase plane plots are shown in Figs. 4.6(b), 4.7(b), and 4.8(b). The diagonal line represents the W-nullcline obtained from the condition $\dot{W} = 0$ and the cubic shaped curve is the V-nullcline obtained
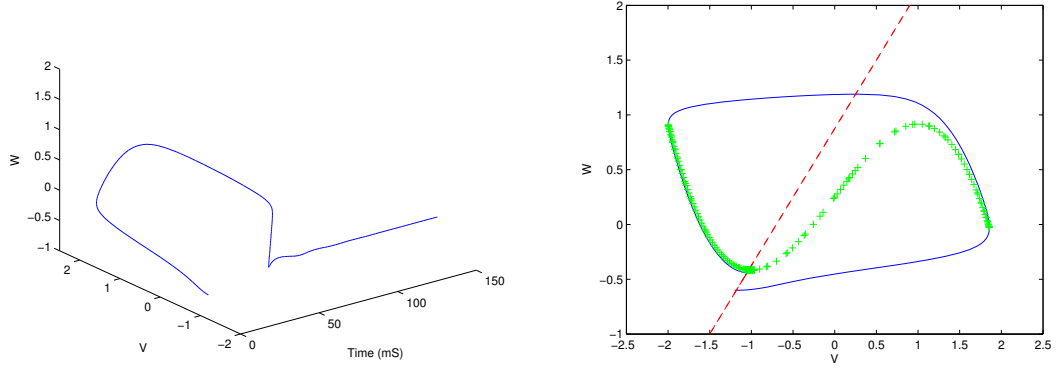
(a) Membrane potential and recovery current.　　　(b) Recovery potential vs membrane voltage.

Figure 4.7: Suprathreshold example of the Fitzhugh-Nagumo model for $I = 0.2\mu$A.
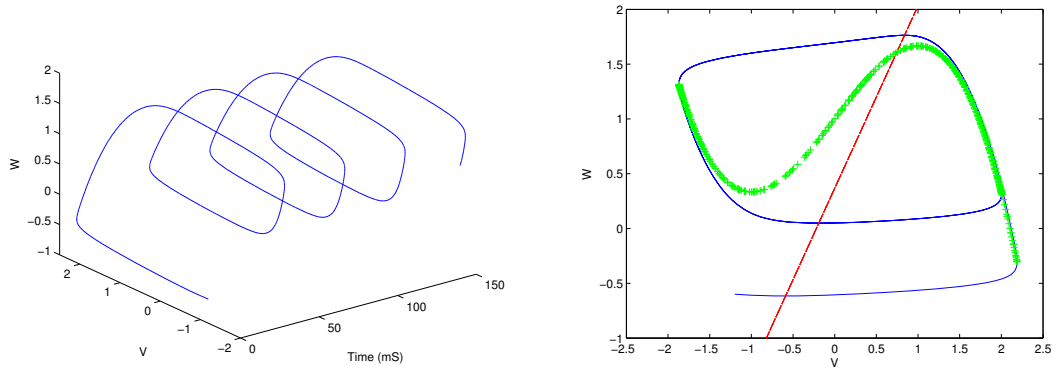
(a) Membrane potential and recovery current.　　　(b) Recovery potential vs membrane voltage.

Figure 4.8: Spiking example of the Fitzhugh-Nagumo model for $I = 1.2\mu$A.

from the condition $\dot{V} = 0$. The intersection of these nullclines $\dot{W} = \dot{V} = 0$ is the equilibrium point of the nonlinear, dynamical system and can be unstable, as shown in the case of the periodic spiking response. The time domain plots of the non-dimensional (see Eqs.(4.9)–(4.10)) membrane voltage V_m and recovery current W are shown for the subthreshold, superthreshold and spiking cases in Figs. 4.9–4.11, respectively.

Through the application of Kirchhoff's laws Nagumo's circuit is represented as

$$C_m \frac{d}{dt}V_m + F(V) + i = -I_0, \tag{4.5}$$

$$L\frac{d}{dt}i + Ri = V - V_0, \tag{4.6}$$

74
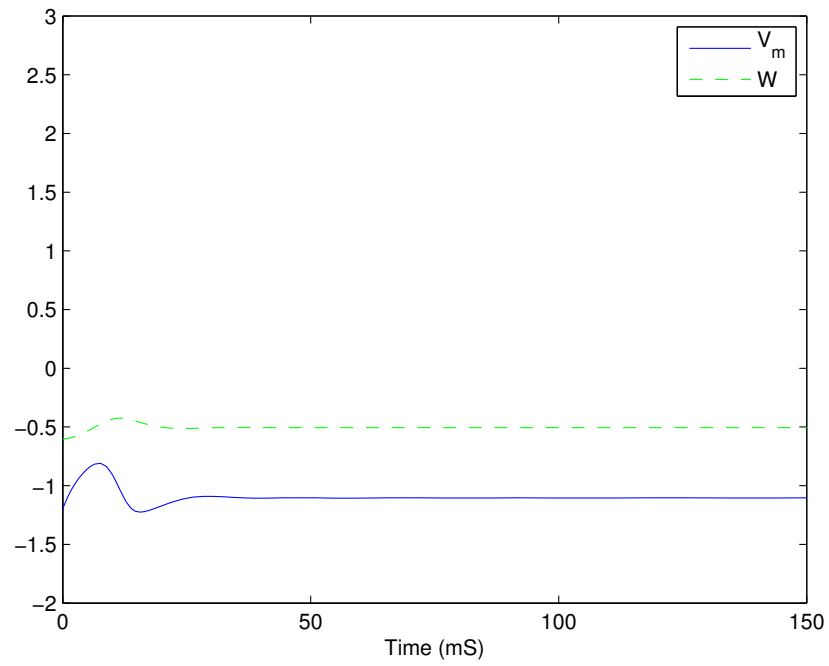
Figure 4.9: Membrane voltage (solid curve) and recovery current (dashed curve) for sub-threshold stimulus.
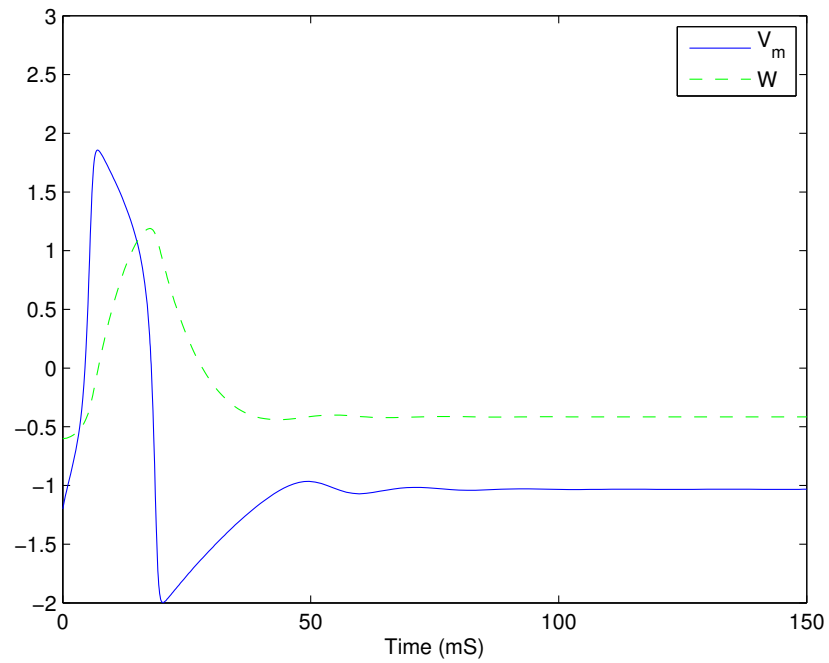
Figure 4.10: Membrane voltage (solid curve) and recovery current (dashed curve) for superthreshold stimulus.
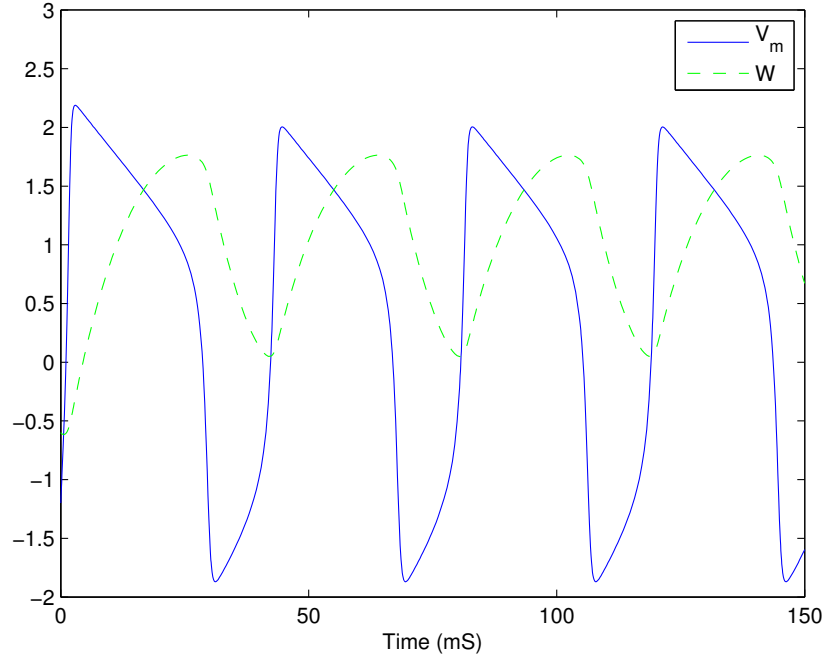
Figure 4.11: Membrane voltage (solid curve) and recovery current (dashed curve) for stimulus sufficiently strong to cause spiking.

where $C_m = 0.01\mu F$ is the membrane capacitance, $F(V)$ is the cubic non-linear term represented by the tunnel diode, I_0 is the injected current, L is representative of the membrane inductance, i is the current flowing through the RL branch and V_0 is the membrane resting potential. Upon solving the system of nonlinear equations

$$\dot{W} = \frac{1}{L}(-V_m + RW - V_0), \tag{4.7}$$

$$\dot{V}_m = \frac{1}{C}(V_m - V_m^3/3 - W + I), \tag{4.8}$$

where the the current voltage relationship of the tunnel diode $f(V) = V - V^3/3$ is substituted. The DC voltage V_0 is representative of the resting potential for the cell as described by the Nernst potential. In literature is common for this set of equations to be non-dimensionalized as

$$\dot{W} = \phi(-V_m + bW + a), \tag{4.9}$$

$$\dot{V}_m = V_m - V_m^3/3 - W + I, \tag{4.10}$$

where $\phi = 0.08$, $b = 0.8$ and $a = 0.7$.

The membrane resting potential is given by

$$V_0 = \frac{RT}{zF} \ln \left(\frac{[X]_o}{[X]_i} \right), \tag{4.11}$$

in volts where $R = 8.31\text{J}/(\text{mol K})$ is the ideal gas constant, $T = 298\text{K}$ is the temperature in Kelvin ($RT/F \sim 25.69\text{mV}$ at room temperature), z is the valance of the ion species, $F = 9.65 \times 10^4\text{C/mol}$ is Faraday's constant , $[X]_o$ is the external concentration of the ion species, and $[X]_i$ is the internal concentration of the ion species. In the case considered there are three unique ion species, Na^+, K^+, and Ca^-, whose Nernst potentials combine linearly for the total resting membrane potential $V_0 \sim -70\text{mV}$.

The necessary voltage threshold for the model presented here is $V_{treshold} \sim -55\text{mV}$ requiring an increase in the membrane potential $V_m = V_0 + 15\text{mV}$. This is an order of magnitude below what would be required to cause membrane breakdown. This would still require a pulsed field on the order of $E \sim 10^9\text{V/m}$ external to the layered tissues in order to externally initiate an action potential as illustrated in Fig. 4.7. However, even at sub-threshold membrane perturbations, the cell's voltage gated ion channels are still being manipulated as depicted in Fig. 4.6. It is this low level, athermal interaction that needs to be studied in further detail to completely understand the full coupling and influence non-ionizing radiation fields have on cellular dynamics.

4.5 Conclusions

The analysis presented in this chapter utilized current quantitative physiology techniques together with electromagnetic scattering theory to provide magnitude of order estimates for the electromagnetic energy that can be delivered from an external source into an anatomic system. The field strengths required to cause membrane break down in a passive cell or excitation in an active cell are orders of magnitude beyond what is seen in common exposures. However, it has been demonstrated here that even at levels below the critical value at which

catastrophic failures occur within the body, there remain intimate interactions influencing a biological cell's voltage gated ion channels. The true physiological interactions are beyond the scope of this dissertation but should be analyzed numerically and experimentally in the future. Current standards such as IEEE C95.1 are based on heating through specific absorption rate which can misrepresent the factor of safety these standards offer as illustrated in Fig. 4.12.

The plot in Fig. 5.18(a) illustrates the C95.1 standard as the solid curve and the power output from PAVE-PAWS system is marked with an 'x', demonstrating a factor of safety of 100. The plot in Fig. 5.18(b) illustrates the numerical determined critical field values solid curve and the field strength used by PAVE-PAWS dashed curve which shows a factor of safety of 10. The apparent safety margin shown in Fig. 5.18(a) is inherent in the steady-state approximations used during the creation of the IEEE C95.1 standard. The reduced factor of safety illustrated in Fig. 5.18(b) demonstrates the significance of transient field components as they have been demonstrated here to carry more energy further into the modeled biological tissues than is suggested by the classical steady state analysis.
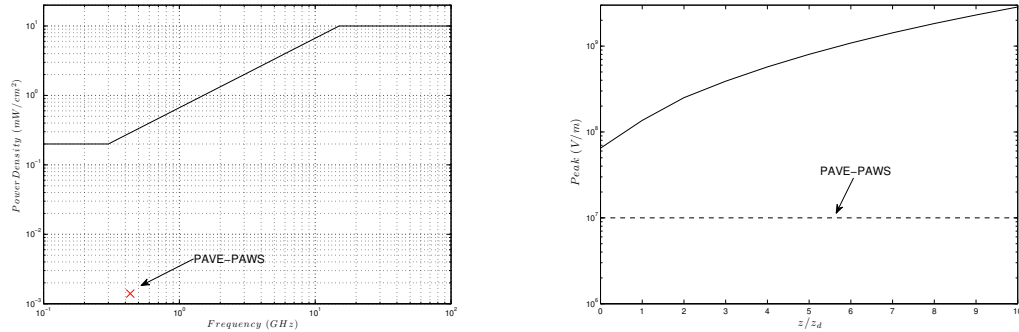
(a) IEEE C95.1 (solid curve) with PAVE-PAWS (x). (b) Critical values (solid curve) with PAVE-PAWS (dashed curve) $z_d \sim 11$cm for $f_c = 435$MHz.

Figure 4.12: Comparison of PAVE-PAWS power density with IEEE C95.1 and numerically determined critical field values with PAVE-PAWS field value.

The Federal Communications Commission (FCC) defines fractional bandwidth as

$$f_b \equiv 2\frac{f_h - f_l}{f_h + f_l}, \tag{4.12}$$

where f_h is the -10dB upper limit and f_l is the -10dB lower limit of the energy bandwidth. According to this technical report, a pulse is ultrawideband if the fractional bandwidth $f_b > 0.25$ or occupies 1.5GHz or more of spectrum space (Commission et al. 2002). The fractional bandwidth of five pulses, of differing temporal duration were calculated for a carrier $f_c = 435$MHz wher the turn on/off time was 10% of the carrier frequency period and N_{osc} is the number of pulses under the rectangular envelope.

N_{osc}	f_b
1	1.62
2	0.51
5	0.30
7	0.21
15	0.11

Table 4.1: Fractional bandwidth f_b as a function of pulse duration N_{osc} at 435MHz.

For the fractional bandwidths presented in Table 4.1, the necessary external field values to cause catastrophic failure to the cell, as presented in this numerical model, embedded at varying distances in muscle are illustrated in Fig. 4.13. According to the FCC definition, pulses at the carrier frequency $f_c = 435$MHz, with a 10% turn on/off time, lasting less than 7 oscillations are ultrawideband. However, the influence of the bandwidth, on the critical field value is minimal, except for the extreme, ultrashort case of 1 oscillation. Additionally, because of the asymptotic nature of the Brillouin precursor its formation and resulting impact on critical field values increases with propagation distance.
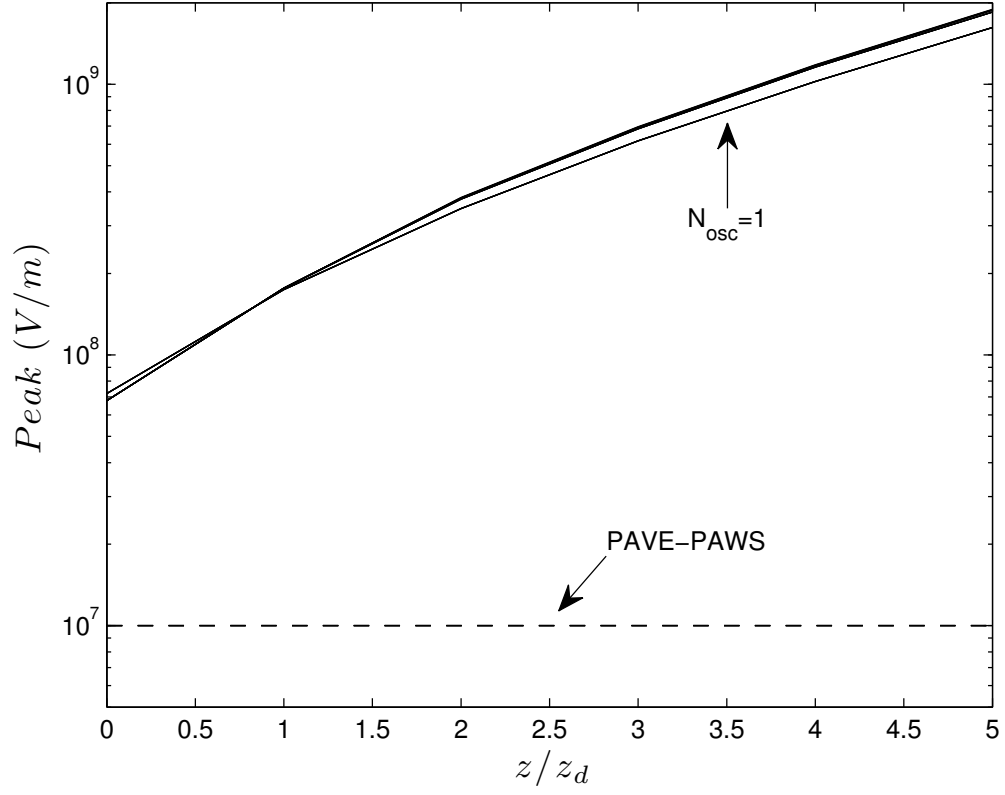
Figure 4.13: Comparison of critical field strength for varying bandwidth pulses (solid curves) with PAVE-PAWS field included for reference (dashed line).

Chapter 5

Extensions, Conclusions and Future Work

5.1 Extension: Optical Precursors in Nonlinear Pulse Dynamics

Under certain conditions, ultrashort pulse dynamics in a linear dispersive medium with absorption result in the appearance of optical precursors that dominate the pulse evolution for large propagation distances. The effects of a nonlinear medium response on this precursor formation is considered using the split-step Fourier method. Comparison of the nonlinear pulse evolution when the full dispersion is used to that when a quadratic Taylor series approximation of the wave number is used shows that the group velocity approximation misses the precursor fields entirely. This work is carried out in the optical domain, at frequencies much greater than previously discussed in this dissertation. The nonlinear Kerr effect as presented here is much more prevalent at optical frequencies compared to microwave or radio frequencies.

5.1.1 Introduction

The asymptotic description of ultrawideband dispersive pulse propagation in a Lorentz model dielectric has its origin in the classic research by Sommerfeld (Sommerfeld 1914) and Brillouin (Brillouin 1914; Brillouin 1960) based on Debye's steepest descent method (Debye 1909). This seminal work established the physical phenomena of forerunners, or precursor fields (Stratton 1941), that were originally associated with the evolution of a Heaviside step-function signal. This description is derived from the exact Fourier-Laplace integral representation of the propagated linearly polarized plane wave field (Oughstun and Sherman 1994; Oughstun 2006b; Oughstun 2009b)

$$E(z,t) = \frac{1}{2\pi} \int_{ia-\infty}^{ia+\infty} \tilde{f}(\omega) e^{\frac{z}{c}\phi(\omega,\theta)} d\omega, \tag{5.1}$$

for $z \geq 0$ with fixed a larger than the abscissa of absolute convergence (Stratton 1941; Oughstun and Sherman 1994; Oughstun 2006b; Oughstun 2009b) for the spectrum $\tilde{f}(\omega) = \int_{-\infty}^{\infty} f(t) e^{i\omega t} dt$ of the initial plane wave pulse $E(0,t) = f(t)$ at $z = 0$. The temporal Fourier spectrum $\tilde{E}(z,\omega)$ of the optical wave field $E(z,t)$ satisfies the Helmholtz equation

$$\left(\nabla^2 + \tilde{k}^2(\omega) \right) \tilde{E}(z,\omega) = 0 \tag{5.2}$$

with complex wave number $\tilde{k}(\omega) = \beta(\omega) + i\alpha(\omega) = (\omega/c)n(\omega)$ in the temporally dispersive medium with complex index of refraction $n(\omega) = n_r(\omega) + in_i(\omega)$ whose real $n_r(\omega) \equiv \Re\{n(\omega)\}$ and imaginary $n_i(\omega) \equiv \Im\{n(\omega)\}$ parts are related through the Kramers-Kronig relations (Oughstun 2006b). Here $\beta(\omega) \equiv \Re\left\{\tilde{k}(\omega)\right\}$ is the propagation (or phase) factor and $\alpha(\omega) \equiv \Im\left\{\tilde{k}(\omega)\right\}$ the attenuation factor for plane wave propagation in the dispersive attenuative medium. In addition,

$$\phi(\omega,\theta) \equiv i\frac{c}{z}\left[\tilde{k}(\omega)z - \omega t\right] = i\omega\left[n(\omega) - \theta\right] \tag{5.3}$$

with $\theta \equiv ct/z$ a nondimensional space-time parameter defined for all $z > 0$.

Based upon this exact integral representation, the modern asymptotic theory (Oughstun and Sherman 1988; Cartwright and Oughstun 2007) provides a uniform asymptotic

description of dispersive pulse dynamics in a single-resonance Lorentz model dielectric with causal, complex index of refraction given by (Oughstun 2006b)

$$n(\omega) = \left(1 - \frac{\omega_p^2}{\omega^2 - \omega_0^2 + 2i\delta\omega} \right)^{1/2}, \tag{5.4}$$

with resonance frequency ω_0, damping δ, and plasma frequency ω_p. The absorption band, which corresponds to the region of anomalous dispersion, then extends from $\sim \sqrt{\omega_0^2 - \delta^2}$ to $\sim \sqrt{\omega_1^2 - \delta^2}$, where $\omega_1 \equiv \sqrt{\omega_0^2 + \omega_p^2}$. Sommerfeld's relativistic causality theorem then holds (Sommerfeld 1914; Oughstun and Sherman 1994; Oughstun 2009b; Oughstun and Sherman 1988), which states that if $E(0, t) = 0$ for all $t < 0$, then $E(z, t) = 0$ for all $\theta < 1$ with $z > 0$.

For $\theta \geq 1$, the propagated wave field due to an ultrawideband signal in a single-resonance Lorentz model dielectric may be expressed either as a superposition of component fields as

$$E(z, t) = E_S(z, t) + E_B(z, t) + E_c(z, t), \tag{5.5}$$

or as a linear combination of fields of this form (Oughstun 2009b). Here $E_S(z, t)$ is the first forerunner (Sommerfeld 1914; Brillouin 1914; Brillouin 1960) or Sommerfeld precursor describing the high-frequency ($|\omega| \geq \omega_1$) response of the dispersive medium, $E_B(z, t)$ is the second forerunner (Brillouin 1914; Brillouin 1960) or Brillouin precursor describing the low-frequency ($|\omega| \leq \omega_0$) response, and $E_c(z, t)$ is the pole contribution describing the signal contribution (if any). The observed pulse distortion for a Heaviside step function signal is then seen to be due to both the precursor fields and their interference with the signal contribution. For a gaussian envelope pulse, the dynamical pulse evolution is comprised of just the precursor fields (Oughstun 2009b; Oughstun and Balictsis 1996) because its spectrum $\tilde{E}_G(0, \omega)$ is an entire function of complex ω. Of particular importance here is that the peak amplitude of the Brillouin precursor $E_B(z, t)$ experiences zero exponential decay with propagation distance $z > 0$, decreasing algebraically as $z^{-1/2}$ in the dispersive, absorptive medium for $\delta > 0$ bounded away from zero (Oughstun and Sherman 1994; Oughstun 2009b; Oughstun and Sherman 1988; Cartwright and Oughstun 2007) .

By comparison, the group velocity description of dispersive pulse propagation was formulated by Havelock (Havelock 1908; Havelock 1914) based upon Kelvin's stationary phase method (Kelvin 1887). In this approach, the wave number $k(\omega)$, assumed there to be real-valued, is expanded in a Taylor series about some wave number value k_0 that the spectrum of the wave group is clustered about, where (Havelock 1914) "the range of integration is supposed to be small and the amplitude, phase and velocity of the members of the group are assumed to be continuous, slowly varying, functions" of the wave number. Notice that Havelock's group method (Havelock 1908; Havelock 1914) is a significant departure from Kelvin's stationary phase method (Kelvin 1887), where k_0 is the stationary phase point of the wavenumber $k(\omega)$. This apparently subtle change in the value of k_0 results in significant consequences on the accuracy of the resulting group velocity description based on this method (Oughstun 2009b; Oughstun and Xiao 1997; Xiao and Oughstun 1999).

The accuracy of the quadratic Taylor series approximation of the complex wave number

$$\tilde{k}(\omega) \approx \tilde{k}(\omega_c) + \tilde{k}'(\omega_c)(\omega - \omega_c) + (1/2)\tilde{k}''(\omega_c)(\omega - \omega_c)^2, \tag{5.6}$$

where $\tilde{k}'(\omega) \equiv \partial \tilde{k}(\omega)/\partial \omega$ and $\tilde{k}''(\omega) \equiv \partial^2 \tilde{k}(\omega)/\partial \omega^2$, is illustrated in Fig. 1 with $\omega_c = 1.0 \times 10^{15} r/s$ for a moderately dispersive resonance line at $\omega_0 = 2.4 \times 10^{15} r/s$ with $\omega_p/\omega_0 \simeq 0.00127$ and $\delta/\omega_0 = 0.025.$, the upper plot describing the scaled real part $(c/\omega)[\beta(\omega) - \beta(\omega_c)]$ and the lower plot the imaginary part $\alpha(\omega)$ of $\tilde{k}(\omega)$. Although $\beta(\omega)$ is accurately modeled over a finite frequency interval below resonance (because $\omega_c < \omega_0$) in this case, diverging from the actual behavior both when ω increases sufficiently above or below the medium resonance frequency ω_0, $\alpha(\omega)$ is overestimated for all frequencies above and below the carrier frequency ω_c. Because of this, the frequency dependence of $\alpha(\omega)$ is typically neglected in the group velocity approximation where $\alpha(\omega) \approx \alpha(\omega_c)$.

As a consequence of these error sources, which are fundamental to the group method, the accuracy of the group velocity approximation rapidly decreases in the ultrawideband signal, ultrashort pulse limit as the pulse rise- or fall-time decreases below the characteristic relaxation time of the medium resonance (Oughstun 2009b; Oughstun and Xiao 1997; Xiao
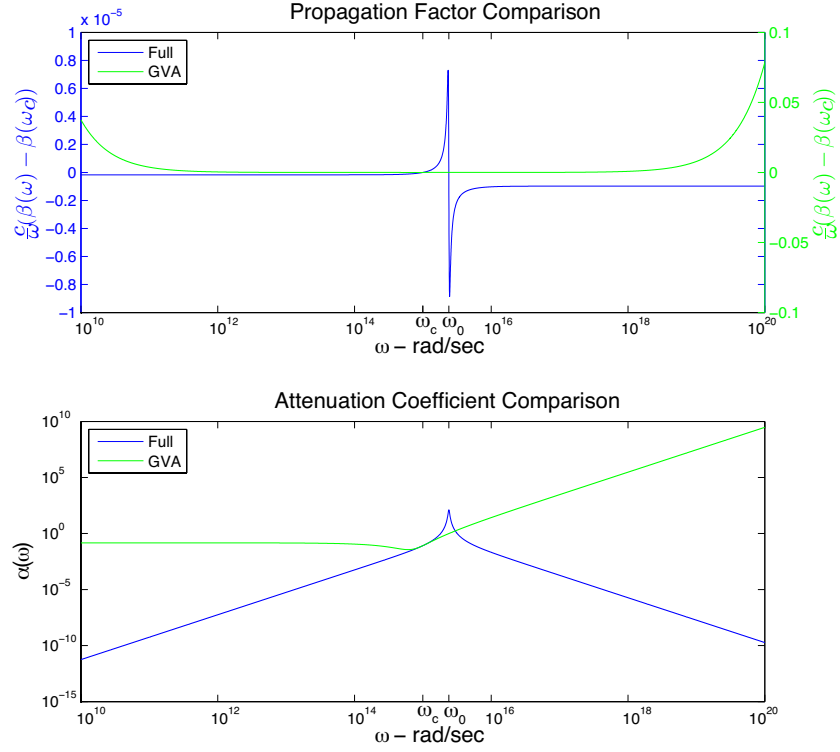
Figure 5.1: Exact (blue curves) and quadratic Taylor series approximation (green curves) of the scaled propagation factor $(c/\omega)\beta(\omega)$ (upper plot) and the attenuation coefficient $\alpha(\omega)$ of the complex wave number for a single resonance Lorentz model dielectric with $\omega_0 = 2.4 \times 10^{15} r/s$, $\delta = 6.0 \times 10^{13} r/s$, $\omega_p = 3.05 \times 10^{12} r/s$.

and Oughstun 1999). This result is now extended to the nonlinear regime where the relative importance of the precursor fields has so far been neglected.

5.1.2 Formulation of the Nonlinear Problem

The formulation of the nonlinear dispersive pulse propagation problem begins with the inhomogeneous scalar wave equation (see §11.3 of (Oughstun 2009b) and §1.3 of (Agrawal 1989))

$$\nabla^2 E((\mathbf{r}, t)) - \frac{1}{c^2} \frac{\partial^2 E((\mathbf{r}, t))}{\partial t^2} = \frac{4\pi}{c^2} \frac{\partial^2 P((\mathbf{r}, t))}{\partial t^2} \tag{5.7}$$

for a linearly polarized pulse in a simple dispersive medium characterized by the constitutive relation $D((\mathbf{r}, t)) = E((\mathbf{r}, t)) + 4\pi P((\mathbf{r}, t))$. With substitution of the complex phasor representation $E_{\omega_c}((\mathbf{r}, t)) \equiv A((\mathbf{r}, t)) e^{i(\varphi((\mathbf{r},t)) - \omega_c t)}$, where $E((\mathbf{r}, t)) = \Re\{E_{\omega_c}((\mathbf{r}, t))\}$, the linear material polarization response is found as (Oughstun 2009b) $P_{\omega_c}((\mathbf{r}, t)) = \chi_e(\omega_c) A((\mathbf{r}, t)) e^{i(\varphi((\mathbf{r},t)) - \omega_c t)}$, where $P((\mathbf{r}, t)) = \Re\{P_{\omega_c}((\mathbf{r}, t))\}$ and $\chi_e(\omega)$ denotes the electric susceptibility, and the wave equation (5.7) becomes

$$\nabla^2 E_{\omega_c}((\mathbf{r}, t)) - \frac{n^2(\omega_c)}{c^2} \frac{\partial^2 E_{\omega_c}((\mathbf{r}, t))}{\partial t^2} = 0. \tag{5.8}$$

With the inclusion of a cubic nonlinearity (Agrawal 1989), this wave equation may be generalized as

$$\nabla^2 E_{\omega_c}((\mathbf{r}, t)) - \frac{n^2(\omega_c)}{c^2} \frac{\partial^2 E_{\omega_c}((\mathbf{r}, t))}{\partial t^2} + \gamma \left| E_{\omega_c}((\mathbf{r}, t)) \right|^2 E_{\omega_c}((\mathbf{r}, t)) = 0, \tag{5.9}$$

where γ is the nonlinear-index coefficient.

This nonlinear dispersive wave equation may be solved numerically using the split-step Fourier method introduced by Hardin and Tappert (Hardin and Tappert 1973) in 1973 by separating it into linear (dispersive and attenuating) and nonlinear parts as

$$\nabla^2 E_{\omega_c}((\mathbf{r}, t)) - \frac{n^2(\omega_c)}{c^2} \frac{\partial^2 E_{\omega_c}((\mathbf{r}, t))}{\partial t^2} = 0. \tag{5.10}$$

and

$$\nabla^2 E_{NL}((\mathbf{r}, t)) + \gamma \left| E_{NL}((\mathbf{r}, t)) \right|^2 E_{NL}((\mathbf{r}, t)) = 0, \tag{5.11}$$

respectively. The linear part (5.10) can then be transformed back into Eq. (5.7) and from there into the Helmholtz equation [cf. Eq. (5.2)]

$$\left(\nabla^2 + \tilde{k}^2(\omega)\right) \tilde{E}_D((\mathbf{r}, \omega)) = 0, \tag{5.12}$$

where the subscript D indicates that this describes the linear dispersive part of the wave field. The pair of wave equations (5.11) and (5.12) then describe nonlinear dispersive pulse propagation, including diffraction effects, without the usual approximations associated with the group velocity method. An analogous formulation has been presented by Laine and Friberg (Laine and Friberg 2000).

Attention is now restricted to plane wave propagation in the positive z-direction through the nonlinear dispersive material. Equations (5.11) and (5.12) then admit the solutions

$$E_{NL}(z + h, t) = e^{\imath \sqrt{\gamma}|E_{NL}(z,t)|h} E_{NL}(z, t), \tag{5.13}$$

and

$$\tilde{E}_D(z + h, \omega) = e^{-\imath \tilde{k}(\omega)h} \tilde{E}_D(z, \omega), \tag{5.14}$$

respectively, where h is the numerical step size taken in the split-step method. The step size is taken here as $h = z_d/5$, where $z_d = c/(\omega_c n_i(\omega_c))$, with $n_i(\omega_c) = \Im\{n(\omega_c)\}$, is the e^{-1} absorption depth, where $z_d \simeq 12.18m$ for the material parameters used in this paper with $\gamma = 1$.

In each numerical simulation presented here, the pulse was propagated 5 absorption depths in order to fully display the influence of the precursor fields on the nonlinear pulse dynamics. In this numerical simulation, Eq. (5.14) is first applied to the pulse spectrum at $z = z_j$ and the result is then transformed to give $E(z_j + h, t)$. This linear propagation step is then followed by a nonlinear propagation step over the distance $h/2$ through Eq. (5.13), as suggested by Agarwal (Agrawal 1989) in order to improve accuracy of the split-step Fourier method. Notice that after the application of the nonlinear operator in Eq. (5.14), the real part of the resultant field is taken in order to to assure physical results.

5.1.3 Heaviside Step-Function Signal Evolution

Consider first a comparison of the dynamical field evolution of a Heaviside unit-step function modulated signal $E_H(0, t) = u_H(t) \sin(\omega_c t)$ with $u_H(t) = 0$ for $t < 0$ and $u_H(t) = 1$ for $t > 0$ in the linear and cubic nonlinear cases, illustrated in Fig. 5.2 at five absorption depths ($z = 5z_d$ with $z_d \equiv \alpha^{-1}(\omega_c)$ for the linear material). The linear result is precisely
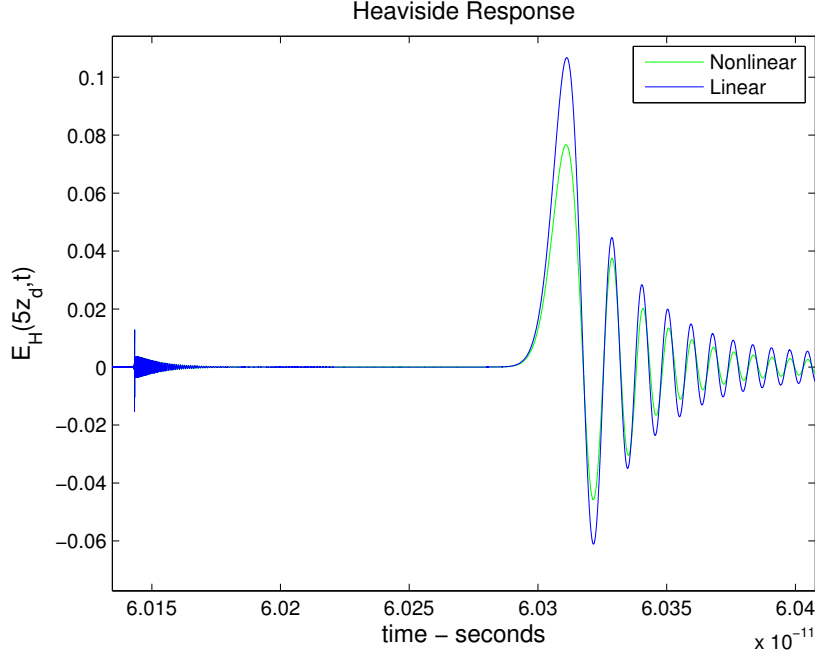
Figure 5.2: Heaviside step-function signal response of the dispersive material at 5 absorption depths with (green curve) and without (blue curve) the cubic nonlinearity included.

that described by the modern asymptotic theory (Oughstun 2009b; Cartwright and Oughstun 2007) and, as the conditions of Sommerfeld's relativistic causality theorem are satisfied in the linear case, $E_H(z, t) = 0$ for all superluminal space-time points $\theta < 1$ with $z > 0$. The propagated wave field then arrives at the luminal space-time point $\theta = 1$ with the onset of the Sommerfeld precursor $E_{HS}(z, t)$, followed by the slower Brillouin precursor $E_{HB}(z, t)$ whose peak amplitude point travels at the velocity $v_B = c/\theta_0 = c/n(0)$, decaying only as $z^{-1/2}$, which is then followed by the main signal $A_{Hc}(z, t)$. The nonlinear signal evolution is remarkably similar, vanishing for superluminal space-time points $\theta < 1$, the propagated

88

wave field arriving at $\theta = 1$ with the onset of a Sommerfeld precursor that is essentially identical with that in the linear case. This is then followed by a Brillouin precursor whose peak amplitude is $\sim 82\%$ of that in the linear case with a nearly identical oscillation frequency. Notice that the cubic nonlinearity generates a small amplitude frequency component at $3\omega_c$ into the propagated wave field as the signal arrival at $\omega = \omega_c$ is approached. The propagated signal spectrum presented in Fig. 5.3 shows that the cubic nonlinearity generates frequency components at the odd harmonics $3\omega_c, 5\omega_c, 7\omega_c, \ldots$ of the carrier frequency as well as filling in the linear spectral loss in the absorption band about ω_0. This odd-harmonic structure is missing when the quadratic wave number approximation in Eq. (5.6) is employed.
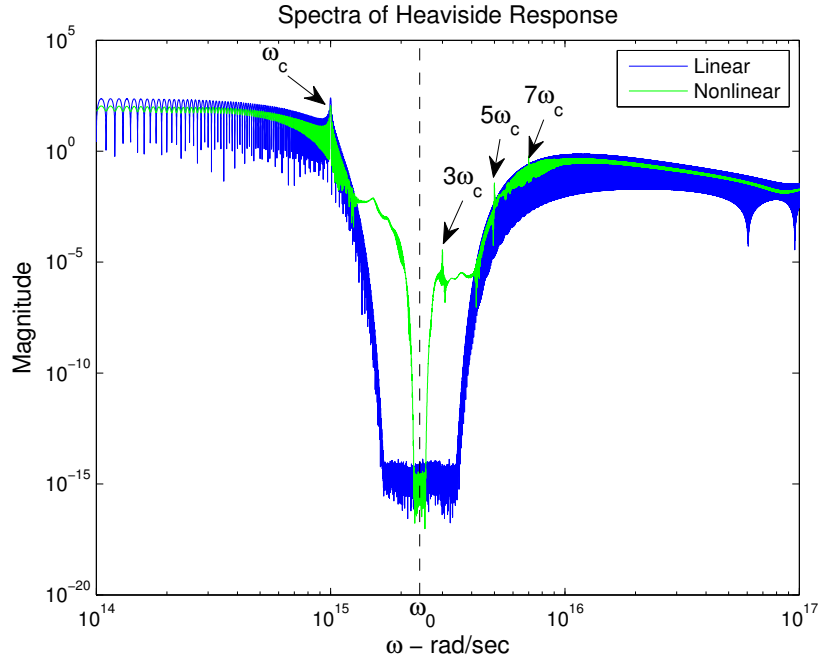
Figure 5.3: Propagated spectra of the Heaviside step function signal illustrated in Fig. 5.2 for the linear (solid blue curve) and nonlinear (solid green curve) dispersion cases.

5.1.4   Gaussian Envelope Pulse Evolution

The second type of input signal considered here is the gaussian envelope modulated signal

$$E_g(0,t) = \exp\left(-\frac{(t-\tau/2)^2}{\tau_0^2}\right)\cos(\omega_c t), \qquad (5.15)$$

where a cosine carrier is used so that the maxima of the envelope and signal coincide. Here $2\tau_0$ denotes the temporal width of the gaussian envelope at the e^{-1} amplitude points. In the numerical examples presented here, the initial pulse width $2\tau_0$ was varied from $\frac{1}{2}T_c$ to $100T_c$, where $T_c \equiv 2\pi/\omega_c$ is the oscillation period of the carrier wave. For the below resonance carrier frequency $\omega_c = 1 \times 10^{15} r/s$, this corresponds to initial pulse widths ranging from the ultrashort $\frac{1}{2}T_c \simeq 3.14fs$ to the narrowband $100T_c \simeq 628fs$. The spectral magnitude $|\tilde{u}(\omega)|$ for each of these two extreme cases is illustrated in Fig. 5.4 in reference to the linear material phase dispersion. For comparison, the dashed curve in the figure describes the magnitude of the scaled Heaviside step function signal spectrum $|\omega - \omega_c|^{-1}$. Notice that the ultrashort $\frac{1}{2}T_c$ pulse spectrum (violet shaded region in Fig. 5.4) is ultrawideband in comparison to the material dispersion, whereas the ultrashort $3T_c$ pulse spectrum (red shaded region) is wideband below resonance and the narrowband pulse spectrum (blue shaded region in Fig. 5.4) is quasimonochromatic. The Sommerfeld and Brillouin precursor fields that are characteristic of the full material dispersion will clearly dominate the field evolution in the ultrawideband but not in the narrowband case. Because the intermediate wideband case fills the spectral region below the material resonance, only the low-frequency Brillouin precursor will be present in that case.

It is expected that the precursor fields will begin to become negligible in the total pulse evolution when the maximum slope of the initial pulse envelope function

$$u(t) = e^{(-t^2/\tau_0^2)} \tag{5.16}$$

is on the order of or greater than the medium relaxation time $T_r \sim \delta^{-1}$ (Oughstun 2009b). The first and second time derivatives of this function are given respectively by

$$u'(t) = \frac{-2t}{\tau_0^2} e^{(-t^2/\tau_0^2)}, \quad u''(t) = -\frac{2}{\tau_0^2} e^{(-t^2/\tau_0^2)} \left(\frac{2t^2}{\tau_0^2} - 1 \right). \tag{5.17}$$

The inflection point of $u'(t)$ is given by the appropriate zero of $u''(t)$, which has zeroes given by $t = \pm\tau_0/(2)^{1/2}$. Substitution of the negative root, which corresponds to the maximum,
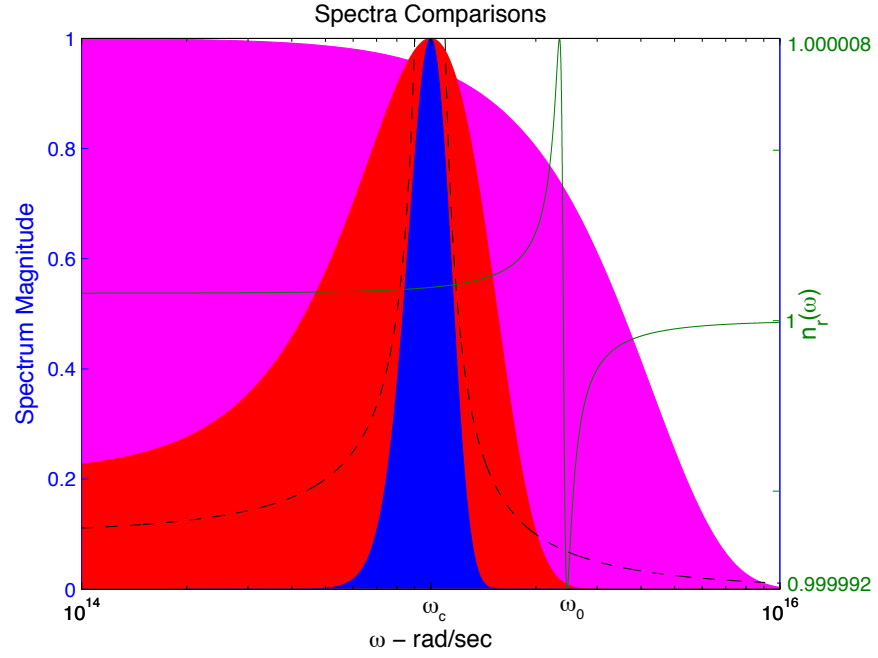
Figure 5.4: Comparison of the spectral magnitude $|\tilde{u}(\omega)|$ of the gaussian pulse envelope for the ultrawideband $2\tau_0 \simeq 3.14fs$ (magenta), the wideband $2\tau_0 \simeq 18.8fs$ (red), and the narrowband $2\tau_0 \simeq 628fs$ (blue) pulse cases. The linear material phase dispersion (green curve) and ultrawideband spectrum $|\omega - \omega_c|^{-1}$ (dashed curve) plots are included for reference.

into the expression for $u'(t)$ and equating the result to δ then yields the critical value

$$\tau_c = \delta^{-1}\sqrt{2/e} \approx 1.43 \times 10^{-14}s, \qquad (5.18)$$

which corresponds to a minimum $N_{osc} = 4.6$ for $\omega_c = 1 \times 10^{15} r/s$. Below this critical value, either one or both of the precursor fields will be fully realized in the propagated wave field, depending on the value of the pulse carrier frequency ω_c in comparison to the medium resonance frequency ω_0. On the other hand, as τ_0 is increased above τ_c, the observed pulse distortion will approach that described by the group velocity approximation, as is now shown.

A comparison of the computed linear and nonlinear pulse structure due to an input 3 oscillation gaussian pulse $(2\tau_0 \simeq 18.8fs)$ is presented in Fig. 5.5 at 5 absorption depths $(z = 5z_d)$ into the dispersive medium whose linear frequency dispersion is illustrated in Fig. 5.1, the full dispersion response being employed in both cases. Because the pulse carrier frequency ω_c is sufficiently below the material resonance frequency ω_0 so that there is negligible spectral energy above ω_1, as seen in Fig. 5.4, the high-frequency Sommerfeld precursor is essentially absent from the propagated pulse, the pulse structure then being dominated by the Brillouin precursor (Oughstun and Balictsis 1996); as the initial pulse width $2\tau_0$ is decreased below a single oscillation, however, and the initial pulse spectrum becomes increasingly ultrawideband, the Sommerfeld precursor becomes increasingly dominant in the propagated field structure (see Fig. 5.6). Comparison of the propagated linear and nonlinear pulse shapes presented in Fig. 5.5 shows that the nonlinearity primarily decreases the amplitude of the gaussian Brillouin precursor evolution, the peak amplitude being decreased to $\sim 82\%$ of its linear value, the same amount obtained for the step function signal.

The sequence of figures presented in Figs. 5.6–5.12 provides a comparison of the nonlinear gaussian pulse evolution at 5 absorption depths as the initial pulse width $2\tau_0$ is increased from the ultrawideband to the quasimonochromatic spectral extremes when the full and approximate [see Eq. (5.6)] dispersion relations are employed in the numerical propagation

92
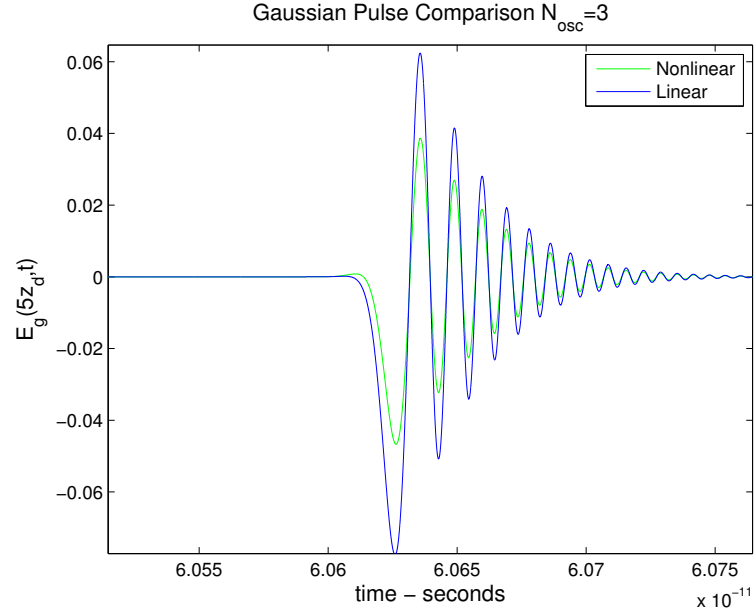
Figure 5.5: Comparison of the propagated linear (blue curve) and nonlinear (green curve) gaussian pulses at 5 absorption depths ($z = 5z_d$) in a single resonance Lorentz-model dielectric with below resonance carrier frequency $\omega_c = 0.41\bar{6}\omega_0$.
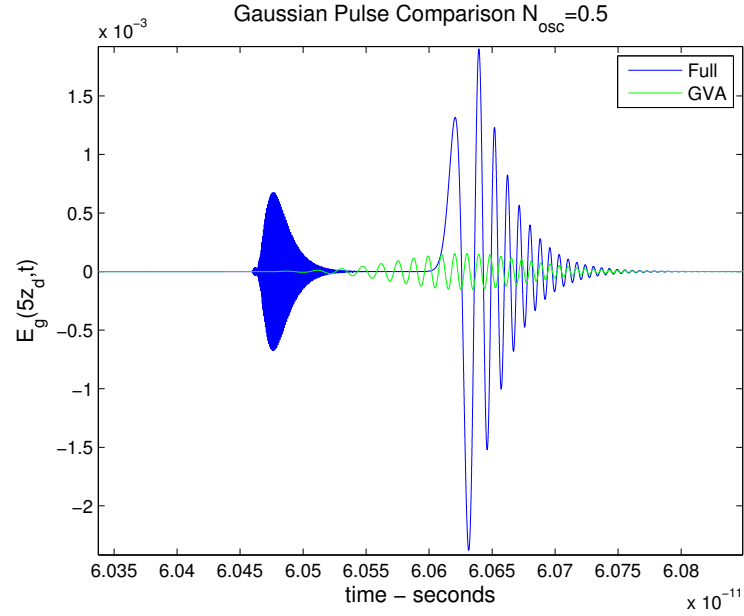
Figure 5.6: Comparison of the nonlinear gaussian pulse distortion using the full (blue curve) and quadratic approximation (green curve) of the linear material dispersion at 5 absorption depths for the $N_{osc} = 0.5$ gaussian envelope case ($2\tau_0 \simeq 3.14fs$) with $\tau_0/\tau_c \simeq 0.11$.
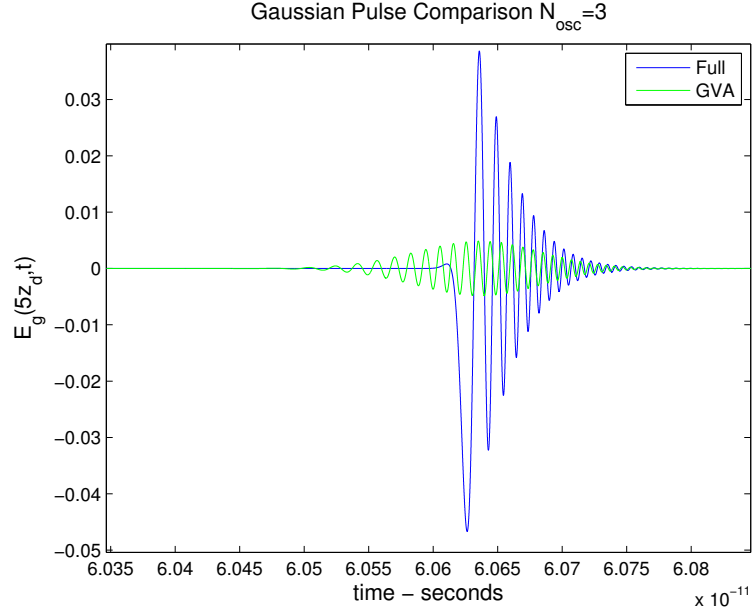
Figure 5.7: Comparison of the nonlinear gaussian pulse distortion using the full (blue curve) and quadratic approximation (green curve) of the linear material dispersion at 5 absorption depths for the $N_{osc} = 3$ gaussian envelope case ($2\tau_0 \simeq 18.8 fs$) with $\tau_0/\tau_c \simeq 0.66$.
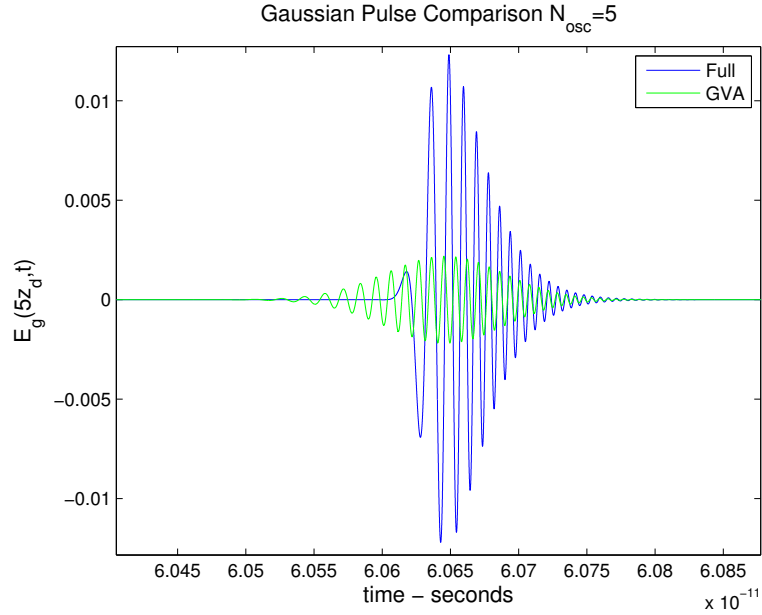
Figure 5.8: Comparison of the nonlinear gaussian pulse distortion using the full (blue curve) and quadratic approximation (green curve) of the linear material dispersion at 5 absorption depths for the $N_{osc} = 5$ gaussian envelope case ($2\tau_0 \simeq 31.4 fs$) with $\tau_0/\tau_c \simeq 1.10$.
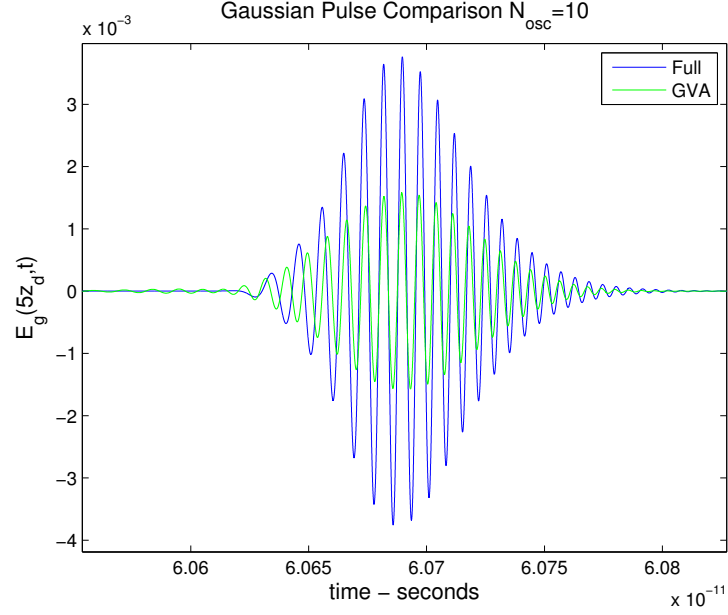
Figure 5.9: Comparison of the nonlinear gaussian pulse distortion using the full (blue curve) and quadratic approximation (green curve) of the linear material dispersion at 5 absorption depths for the $N_{osc} = 10$ gaussian envelope case $(2\tau_0 \simeq 62.8fs)$ with $\tau_0/\tau_c \simeq 2.20$.
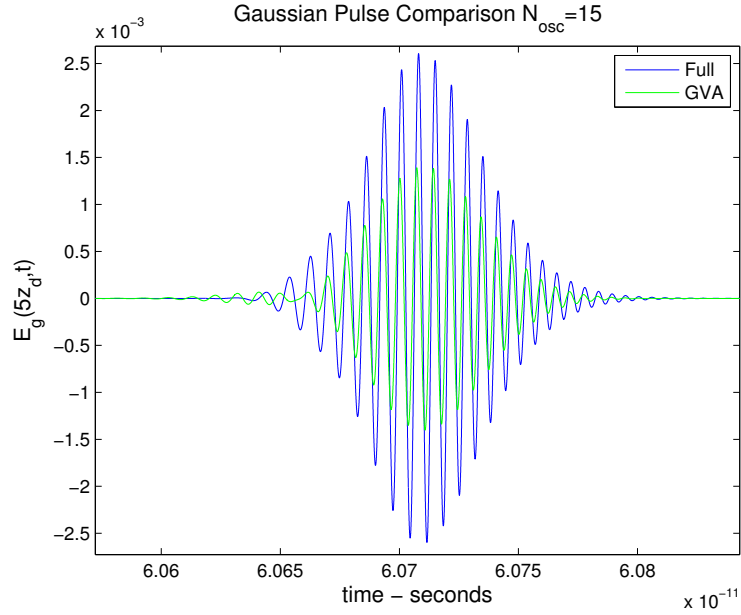
Figure 5.10: Comparison of the nonlinear gaussian pulse distortion using the full (blue curve) and quadratic approximation (green curve) of the linear material dispersion at 5 absorption depths for the $N_{osc} = 15$ gaussian envelope case $(2\tau_0 \simeq 94.3fs)$ with $\tau_0/\tau_c \simeq 3.30$.
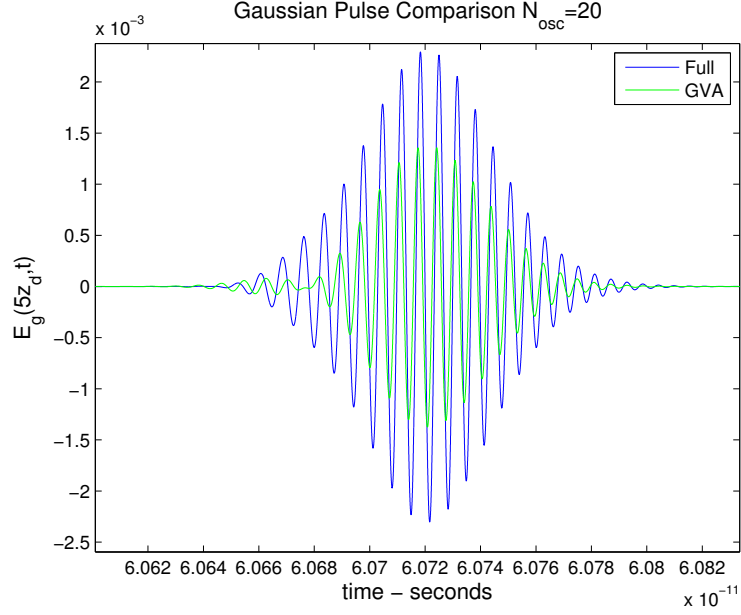
Figure 5.11: Comparison of the nonlinear gaussian pulse distortion using the full (blue curve) and quadratic approximation (green curve) of the linear material dispersion at 5 absorption depths for the $N_{osc} = 20$ gaussian envelope case ($2\tau_0 \simeq 125.7fs$) with $\tau_0/\tau_c \simeq 4.39$.
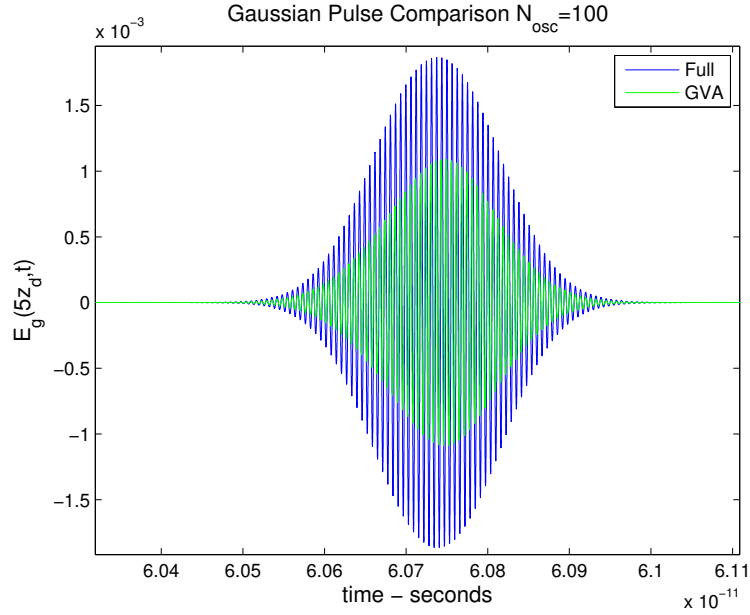
Figure 5.12: Comparison of the nonlinear gaussian pulse distortion using the full (blue curve) and quadratic approximation (green curve) of the linear material dispersion at 5 absorption depths for the $N_{osc} = 100$ gaussian envelope case ($2\tau_0 \simeq 628.3fs$) with $\tau_0/\tau_c \simeq 22.0$.
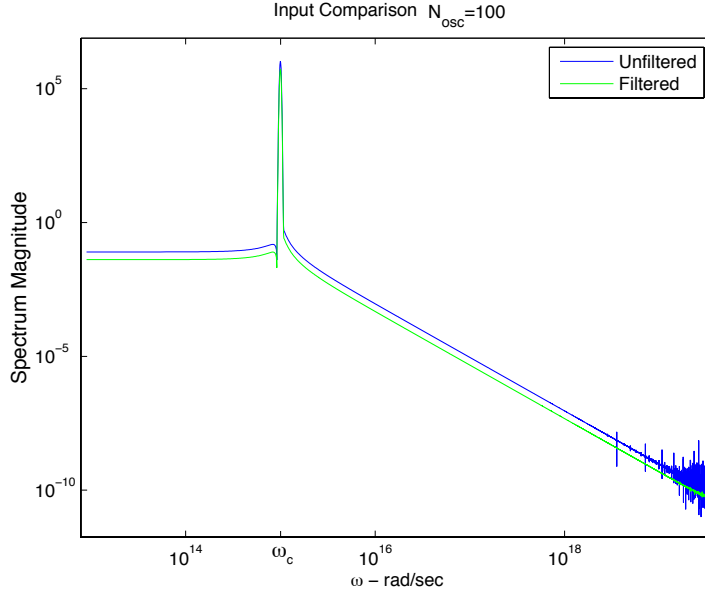
Figure 5.13: Filtered and unfiltered spectra for the initial 100 oscillation gaussian envelope pulse.

model. For the ultrawideband $3.14fs$ pulse case illustrated in Fig. 5.6, the propagated gaussian pulse has separated into an above resonance gaussian Sommerfeld precursor and a below resonance gaussian Brillouin precursor component, as described in (Oughstun and Balictsis 1996). Notice that the group velocity approximation accurately describes just the trailing edge of the gaussian Brillouin precursor component, its peak amplitude being $\sim 10\%$ of the actual peak amplitude value.

As the initial pulse width $2\tau_0$ is increased with the carrier frequency ω_c fixed below resonance, the Sommerfeld precursor component becomes negligible in comparison to the Brillouin precursor component (the opposite will be found when the pulse carrier frequency is situated sufficiently far above resonance), as seen in Fig. 5.7 for the $18.8fs$ pulse case and Fig. 5.8 for the $31.4fs$ pulse case. In both cases, the quadratic group velocity approximation only describes the trailing edge of the Brillouin precursor component with any accuracy. At this point when the critical pulse width value τ_c is exceeded, a gradual transition from the wideband, precursor dominated behavior to the narrowband quasimonochromatic behavior is observed, as evidenced in Figs. 5.9–5.12.

97

In Figs. 5.10–5.12 as the initial pulse spectrum becomes increasingly quasimonochromatic, the group velocity description provides a reasonable approximation to the actual pulse shape, the major two errors appearing in the underestimated pulse amplitude due to the overestimated material attenuation in the quadratic approximation given in Eq. (5.6) and the slight phase shift appearing at the leading edge of the pulse. Finally, notice that special care had to be taken in modeling the 100 oscillation gaussian pulse case (Fig. 5.12) as high frequency numerical noise in the initial pulse spectrum was amplified by the cubic nonlinearity to produce a secondary pulse. This numerical error source was eliminated here by filtering the initial pulse spectrum to eliminate this noise, as illustrated in Fig. 5.13.

A comparison of the nonlinear space-time evolution of the envelope of the 3 oscillation gaussian pulse with initial pulse width $2\tau_0 \simeq 18.8 fs$ using the full material dispersion and the quadratic approximation of this dispersion is presented in Figs. 5.14 and 5.15, respectively. The evolution of the wideband pulse into a gaussian Brillouin precursor with minimal attenuation is clearly evident in Fig. 5.14 (full dispersion model) while it is noticeably absent in Fig. 5.15 (quadratic approximation of the dielectric dispersion). In both cases there is a sharp drop in the pulse amplitude as the propagation distance increases to a single absorption depth. This is then followed by a transition to the precursor dominated field evolution in the full dispersion case illustrated in Fig. 5.14, where the peak amplitude decay switches from a supra-exponential to a sub-exponential decay, as illustrated by the blue curve in Fig. 5.16. Notice that the peak amplitude decay for the group velocity approximation, indicated by the green curve in Fig. 5.16, remains below the Beer's law limit of pure exponential decay limit (indicated by the dashed black curve in the figure) over the propagation distance domain $z/z_d \in [0, 5]$ considered in the numerical study presented here. The $z^{-1/2}$ algebraic decay that is a characteristic of the Brillouin precursor in the linear case (Oughstun and Sherman 1994; Oughstun 2009b) is greatly exceeded in the nonlinear case, the numerically determined slope p of the full dispersion curve in Fig. 5.16, which describes the z^{-p} peak amplitude decay, decreasing from $p \sim 0.9$ at $z/z_d \sim 0.5$ to $p \sim 0.05$

at $z/z_d \sim 5$. Again, this is due to the cubic nonlinearity which also significantly effects the peak amplitude decay in the group velocity approximation as z/z_d increases above unity.
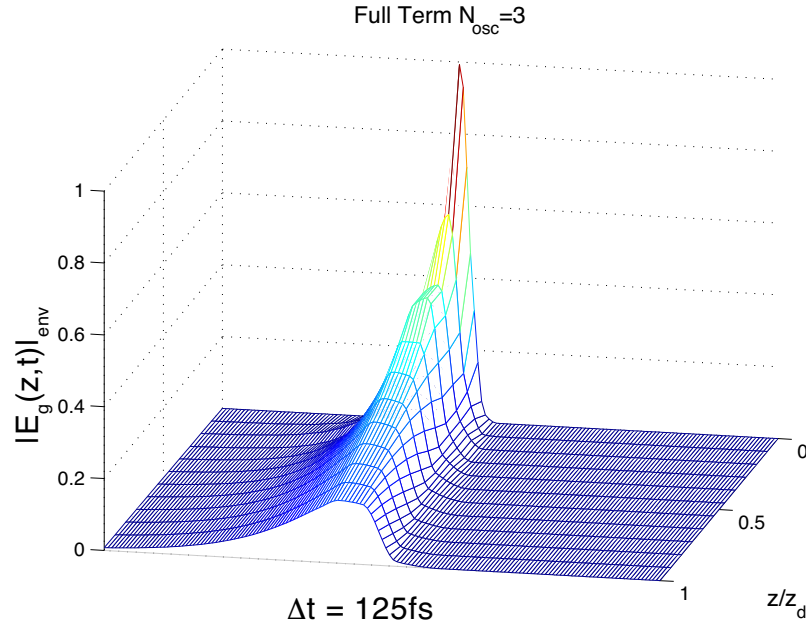
Figure 5.14: Nonlinear space-time evolution of the envelope of a 3 oscillation gaussian pulse with initial pulse width $2\tau_0 \simeq 18.8fs$ using the full material dispersion.

5.1.5 Conclusion

The detailed numerical results presented here have served to establish the following conclusions:

- the precursor fields that are a characteristic of the linear material dispersion persist in the nonlinear case;

- these precursor fields dominate gaussian pulse evolution when the initial pulse width $2\tau_0$ is on the order of or less than the critical pulse width $2\tau_c$, where $\tau_c \sim \delta^{-1}$ is the relaxation time of the medium response [see Eq. (5.18)];

- as found in the linear case for the gaussian envelope pulse (Oughstun and Balictsis 1996), these precursor fields result in the propagated pulse breaking up into above

99
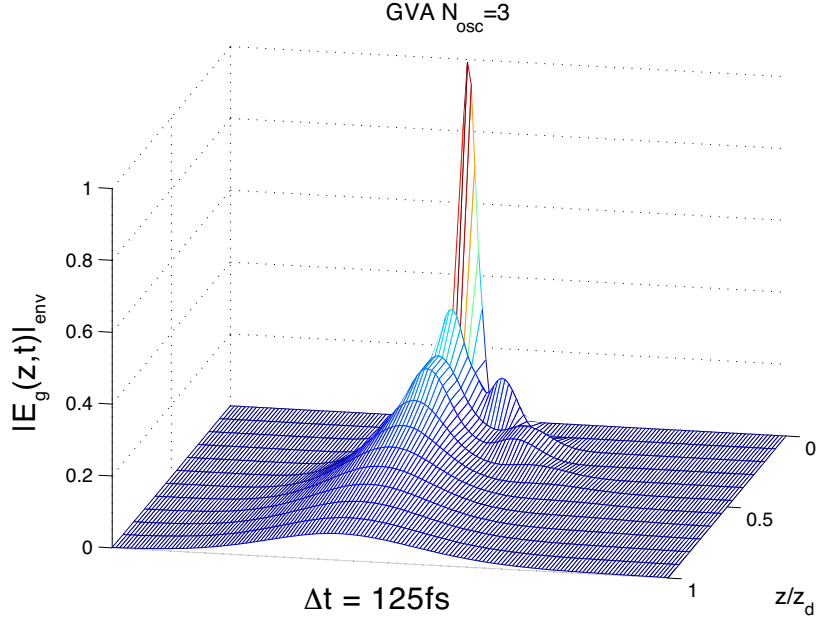
Figure 5.15: Nonlinear space-time evolution of the envelope of a 3 oscillation gaussian pulse with initial pulse width $2\tau_0 \simeq 18.8fs$ using the quadratic approximation of the linear material dispersion.
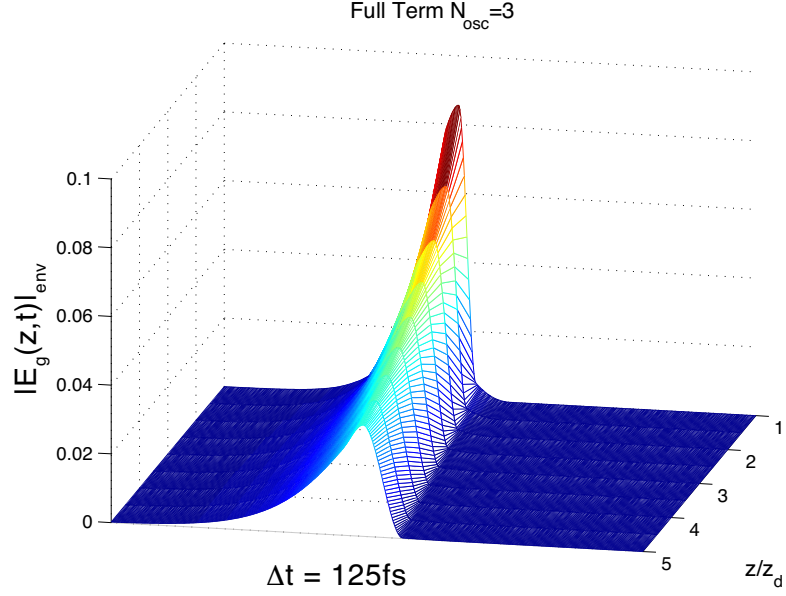
Figure 5.16: Peak amplitude decay of a 3 oscillation gaussian pulse with initial pulse width $2\tau_0 \simeq 18.8fs$ using the full material dispersion (blue curve) and using the quadratic approximation of the linear material dispersion (green curve). The black dashed line describes the Beer's law exponential decay limit e^{-z/z_d} for comparison.

(Sommerfeld precursor) and below (Brillouin precursor) resonance subpulses when the initial pulse width is sufficiently small such that $2\tau_0 \ll 2\tau_c$;

- the characteristic $z^{-1/2}$ peak amplitude decay of the gaussian Brillouin precursor in the linear case is amplified by the cubic nonlinearity;

- the group velocity description fails to accurately describe gaussian pulse evolution when the initial pulse width $2\tau_0$ is on the order of or less than the critical pulse width $2\tau_c$;

- in addition, because the group velocity approximation overestimates the linear material attenuation away from the pulse carrier frequency ω_c, the odd-order harmonics introduced by the cubic nonlinearity are absent in the group velocity description of the pulse evolution.

It is expected that the precursor fields will strongly influence the predicted pulse dispersion for other types of nonlinearity in the ultrashort/ultrawideband pulse regime.

5.2 Conclusions

The current IEEE C95.1 standard provides non-ionizing radiation limits for microwave frequencies and is concerned solely with the thermal heating of tissues. These limits are obtained from steady state analysis based on specific absorption rate calculations, which describes the power absorbed within a given mass of tissue. As outlined in Chapter 1 several independent researchers have voiced concern over the biological influence from athermal interactions provided by electric fields. The work presented in this dissertation is primarily concerned with transient phenomena associated with ultrawideband pulses common in modern radar systems, such as the Precisions Acquisition Vehicle Entry Phased Array Warning System (PAVE PAWS) used by the United States Air Force.

In order to accurately describe energy flow into biological materials a description of their dispersive electrical characteristics, over the band of relevant frequencies, is required. In this

research, the biological materials of skin, fat and muscle are modeled as a semi-conducting Rocard-Powles-Debye dielectrics as given in Eq. (2.56), viz.

$$\frac{\epsilon_c(\omega)}{\epsilon_0} = \epsilon_\infty + \sum_{j=1}^{N} \frac{a_j}{(1 - \imath\omega\tau_j)(1 - \imath\omega\tau_{fj})} + \imath\frac{\sigma_0}{\omega\epsilon_0}. \tag{5.19}$$

These biological tissues are shown to be highly dispersive and lossy with multiple relaxation times as described in Tables 2.2–2.4 for skin, fat and muscle, respectively. The dispersion of the biological tissues skin, fat and muscle are illustrated in Figs. 2.2–2.4, respectively.

The analysis presented in Chapter 3 provides a succinct representation for computing the frequency dependent Fresnel coefficients for a system of N homogeneous, isotropic, locally linear, attenuative, temporally dispersive layers. Previously published research on multi-layer systems neglected dispersion and attenuation within the layers and is classically applied for steady state analysis . The matrix formulation provided in Eq. (3.36) viz.

$$\mathcal{M}(\omega) = \mathcal{D}_0^{-1} \left[\prod_{j=1}^{N-1} \mathcal{D}_j \mathcal{P}_j \mathcal{D}_j^{-1} \right] \mathcal{D}_N, \tag{5.20}$$

where $\mathcal{D}_j$ and $\mathcal{P}_j$ are given in Eqs. (3.33) and (3.34), respectively, allows for dispersion and attenuation in each of the N layers. This extension to include the innate material behaviors of dispersion and loss, as presented here, is necessary in order to use causal models for the description of the layers. Modeling each layer with a causal model is required when simulating propagation of ultrawideband pulses as they ensure causality is preserved. Another key contribution of this work is the numerical demonstration that Brillouin precursor fields will be generated, provided that the turn on/off time of the pulse is less than the relaxation time of the substrate material, even after the incident pulse is passed through an attenuative multi-layer system. This formulation also provides straightforward calculation of the complex, frequency dependent Fresnel reflection coefficient as $r = m_{21}/m_{11}$ and transmission coefficient as $t = 1/m_{11}$. An illustration of the frequency dependent Fresnel coefficients are shown in Fig. 3.3 and shown here. Again, notice the passband in the system around $f \sim 600\text{MHz}$ which is in the neighborhood of the PAVE-PAWS carrier frequency $f_c = 435\text{MHz}$.
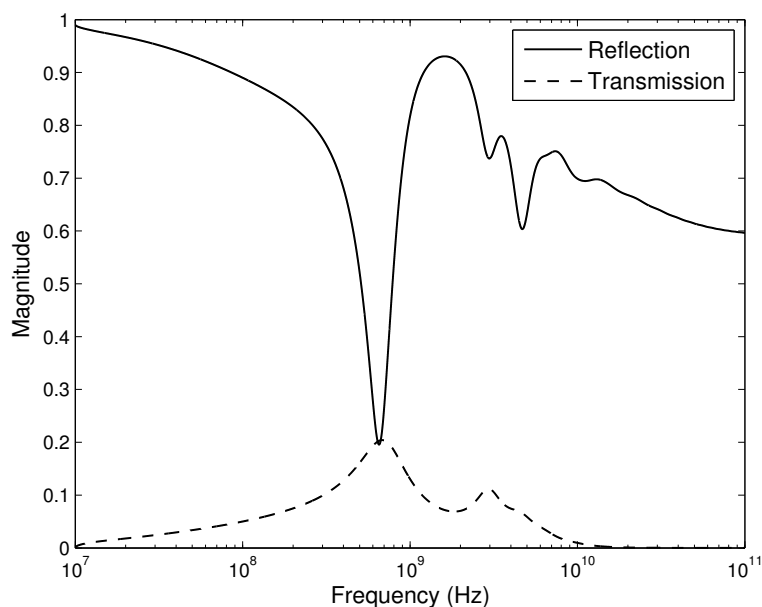
Figure 5.17: Frequency dependence of the complex Fresnel reflection (solid) and transmission (dashed) coefficients for a layered biological system of skin (Δz_1 = 5mm), fat ($\Delta z_2 = 20$mm) and semi-infinite substrate muscle.

The framework presented in Chapter 3 is requisite to analyze transient pulse components from ultrawideband electric fields. As discussed in the introduction, physiological significant response from cellular membranes can be invoked by transients from applied electrical stimuli. The key contributions of Chapter 4 show what portion of an electric field incident upon an idealized, spherical cell, whose dispersive dielectric properties are assumed to be that of water, is injected across the cellular membrane. The analysis and numerical demonstrations of Chapter 4 show that the peak field membrane potentials occur in the transient components, the Brillouin precursor, of the field. Classical steady state analysis does not account for these field components, which are of significant amplitude relative to the main signal contribution. While the Brillouin precursor's oscillation frequency is below that of the carrier frequency, biological experimentation is required to determine if a field of these frequencies can cause membrane breakdown or cellular signaling when applied for such a short duration. In the numerical calculations presented here it is assumed that these fields are physiologically significant. A comparison of the field strengths required to cause

catastrophic athermal failures of a cell are shown in Fig. 4.12 as illustrated here.
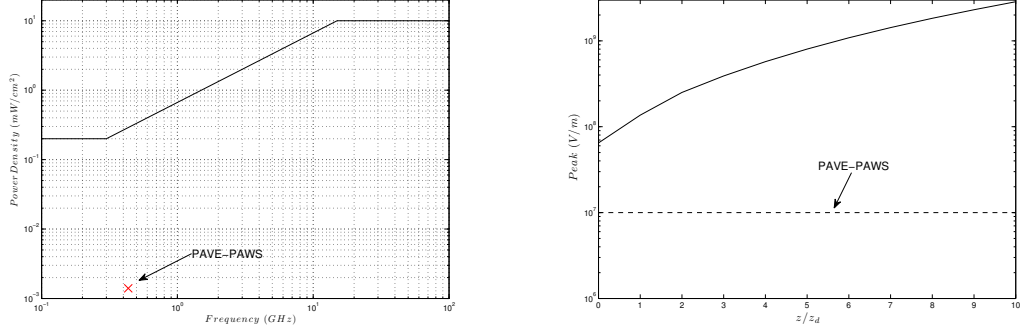
(a) IEEE C95.1 (solid curve) with PAVE-PAWS (x). (b) Critical values (solid curve) with PAVE-PAWS

(dashed curve) $z_d \sim 11$cm for $f_c = 435$MHz.

Figure 5.18: Comparison of PAVE-PAWS power density with IEEE C95.1 and numerically determined critical field values with PAVE-PAWS field value.

5.3 Future Work

Necessary analysis is provided in Chapter 3 for computing the complex, frequency dependent Fresnel coefficients for a system of N planarly layered, dispersive, attenuative dielectric slabs. A necessary extension of this work is for the inclusion of more advanced geometries allowing to capture resonance effects of a layered cavity, such as the human body. It is expected that this analysis would show increased field amplitudes within the cavity for frequencies in the neighborhood of its resonance. This extension would also allow for analysis of layered, radar absorbing type materials covering aircraft and other types of vehicles.

The largest opportunity this work has uncovered is the necessity to examine the biological mechanisms that these numerical models are based on. Questions regarding the high frequency behavior of the cell membrane need to be addressed. The polar molecules that act as the voltage gated ion channels have some natural response time, which a stimulus' duration would need to exceed in order for excitation to occur. A lower bound on this response time needs to be determined experimentally in order to put a high frequency limit on these models. If the circuit equivalent models presented here are characteristic of true

cell biology this would suggest that sufficiently high frequencies the cell membrane no longer blocks ionic current flow, allowing unrestricted passage of extracellular ions into the cell.

The work considering nonlinearities in dispersive media for the microwave domain (Albanese, Penn, and Medina 1993) is limited and should be extended using the detailed numerical analysis presented here. This work would allow for analysis of microwave and radio frequency interactions with biological tissues when the field strengths are sufficiently strong to invoke a nonlinear response in the tissues in frequency domains where orientational polarization dominates ($f \leq 300\text{GHz}$). This would be most readily accomplished by using the numerical technique presented here, but within a medium described by a single relaxation time Rocard-Powles-Debye model dielectric at an appropriate carrier frequency $f_c < 300\text{GHz}$.

Appendix A

Reflection and Transmission of Pulsed Electromagnetic Fields through Multilayered Biological Media

This appendix is a conference paper (Palombini and Oughstun 2011), based on the work presented in Chapter 3, as it appears in the Proceedings of the IEEE International Conference of Electromagnetics in Advanced Applications (ICEAA), 2011.

Reflection and Transmission of Pulsed Electromagnetic Fields through Multilayered Biological Media

C. L. Palombini[*]   K.E. Oughstun[†]

Abstract — The reflection and transmission of ultrawideband electromagnetic pulses through multilayered biological media consisting of three biological tissue layers representing skin, fat and muscle is analyzed. The frequency dependent reflection and transmission coefficients of the multilayer stack are computed using the transfer matrix method. Each of the three tissues is modeled as a homogeneous, isotropic, linear, dispersive, attenuative, dielectric with frequency dispersion described by a multiple relaxation Rocard-Powles-Debye model fit to experimental data.

1 INTRODUCTION

The interaction of non-ionizing radiation with biological tissue remains a problem of great concern as much remains to be understood about the athermal effects of such interactions. It is largely believed that non-ionizing radiation is harmless below exposure levels where heating first occurs [1]. However, this conclusion assumes a continuous, monochromatic signal without any mention of either transient phenomena or pulsed fields that are typically associated with radar and mobile communications. Pulsed fields and their associated transient phenomena are of central importance in the proper analysis of the biological response to applied external fields since the action potential threshold response in cellular signaling is dependent on the rise time of the incident field [2]. In addition, it has been shown that exposure to such stimuli can cause both molecular effects as well as phenotypic effects that are a visible manifestation of genetics [3].

The recently published study conducted by The National Research Council of the National Academy of Sciences has explored possible health effects of pulsed, low-level phased-array radio frequency energy exposure due to the PAVE PAWS radar system located at Cape Cod Air Force Station in Massachusetts. The study raises several important questions regarding the possible health effects of such non-ionizing radiation, describing physical mechanisms for radio frequency effects on biological systems. However, what the report fails to address is the reflectivity and transmissivity for layered biological materials. Preliminary results based on empirical data suggest penetration depths much greater than that previously described by simple theoretical results.

The specific absorption rate threshold set by the Federal Communications Commission on hand-held mobile phones is $1.6 W/kg$, as measured over any one gram of tissue. Recently published research [4] showed that mobile communication devices operating within these radiofrequency limits increase glucose metabolism in the region of the brain closest to the antenna but admits that "the finding is of unknown clinical significance". This then raises concern about the efficacy of this safety standard when applied to ultrawideband (uwb) pulsed fields.

This communication formulates a mathematically rigorous, physically correct description of the propagation of pulsed electromagnetic fields into realistic biological tissues in order to investigate the possible indirect molecular effects such fields have on cellular signaling. The first step in this formulation is a systematic description of the interaction a plane wave encounters at a boundary between a lossless nondispersive medium and a lossy dispersive medium as well as when both media are lossy and dispersive. Recent work [5] provides some explanation of how a uniform plane wave in a lossless media incident on a boundary with a lossy media results in the transmission of a nonuniform plane wave in the second media. However, this work does not mention dispersive media and does not include insight as to how pulsed energy is reflected and transmitted at these interfaces.

In addition to having a proper description of reflection and transmission at a lossy interface, complete and accurate descriptions of biological tissues are necessary to model this interaction. The energy of the propagated field depends upon both the transmission across each material interface, as well as through each dispersive, attenuative layer (labeled $j = 1, 2, ..., N$) where each medium is described by its complex refractive index $n_j(\omega)$. This numerical simulation consists of three stacked biological tissues ($N = 3$) representing skin, fat and muscle with each interface assumed to be planar

---
[*]School of Engineering, University of Vermont, Burlington, VT 05405, USA, e-mail: `cpalombi@uvm.edu`

[†]School of Engineering, University of Vermont, Burlington, VT 05405, USA, e-mail: `oughstun@cems.uvm.edu`

and infinite in the transverse direction. Each tissue is modeled as a homogeneous, isotropic, linear, dispersive lossy dielectric whose frequency dependence follows a multiple relaxation-time Rocard-Powles-Debye model over a wideband frequency range extending from static to $10 GHz$.

Finally, it is now known that when electromagnetic signals that are ultrawideband with respect to the material dispersion propagate through a dispersive medium, electromagnetic precursors emerge in the propagated signal [6]. Of particular importance is the fact that increased energy transmission occurs due to this precursor field formation. Such pulses may then be used for biological imaging and therapy and are the impetus for this research.

2 SEMI CONDUCTING MATERIAL DISPERSION

Biological materials are typically semiconducting with a frequency dependent dielectric permittivity $\epsilon(\omega)$ and electric conductivity $\sigma(\omega)$. These two aspects combine in electromagnetic theory to form the complex permittivity,

$$\epsilon_c(\omega) \equiv \epsilon(\omega) + \imath \frac{\sigma(\omega)}{\omega}, \quad (1)$$

where $\epsilon(\omega) = \epsilon'(\omega) + \imath\epsilon''(\omega)$ and $\sigma(\omega) = \sigma'(\omega) + \imath\sigma''(\omega)$. Upon combining real and imaginary parts of $\epsilon(\omega)$ and $\sigma(\omega)$, the complex permittivity may be expressed as

$$\epsilon_c(\omega) = \left(\epsilon'(\omega) - \frac{\sigma''(\omega)}{\omega} \right) + \imath \left(\epsilon''(\omega) + \frac{\sigma'(\omega)}{\omega} \right). \quad (2)$$

This form of the complex permittivity is appropriate for analyzing empirical data where all of the measured loss is (improperly) assumed to be conductive [7] with an effective conductivity $\sigma_{eff}(\omega) = \sigma'(\omega) + \omega\epsilon''(\omega)$ and effective permittivity $\epsilon_{eff}(\omega) = \epsilon'(\omega) - \sigma''(\omega)/\omega$.

The classical Debye model of orientational polarization dispersion has a nonvanishing absorption coefficient at high frequencies and as such is a first-order model which leads to errors when modeling realistic media. As a consequence, the Debye model is extended here to the Rocard-Powles-Debye model [8] that provide an improved description of experimental data. With the complex Rocard-Powles-Debye model of the relative dielectric permittivity the relative complex dielectric permittivity is given by

$$\frac{\epsilon_c(\omega)}{\epsilon_0} = \epsilon_\infty + \sum_{j=1}^{N} \frac{a_j}{(1 - \imath\omega\tau_j)(1 - \imath\omega\tau_{fj})} + \imath \frac{\sigma_0}{\epsilon_0\omega}. \quad (3)$$

Here ϵ_∞ is the high frequency limit of the relative permittivity of the model, $\epsilon_0 \approx 8.854 \times 10^{-12} F/m$ is the permittivity of free space, τ_j is the jth relaxation time, τ_{fj} is the associated j^{th} friction time, a_j is strength of the jth relaxation mode and $\sigma_0 \equiv \sigma(0)$ is the static conductivity of the lossy medium.

2.1 Skin

The best-fit Rocard-Powles-Debyle model for skin is composed of four relaxation modes ($N = 4$). The high frequency permittivity for dry skin is found to be $\epsilon_\infty = 15$ and the static conductivity to be $\sigma_0 = 3 \times 10^{-5} S/m$; the remaining model parameters are given in Table 1. Notice that the $j = 1$ and $j = 3$ modes provide the dominant structure of the frequency dispersion mode fit illustrated in Fig. 1.

j	a_j	τ_j (sec)	τ_{fj} (sec)
1	600	1×10^{-6}	1×10^{-14}
2	75	1×10^{-4}	1×10^{-12}
3	550	1×10^{-8}	1×10^{-12}
4	28	1×10^{-10}	1×10^{-13}

Table 1: Model parameters for dry skin.
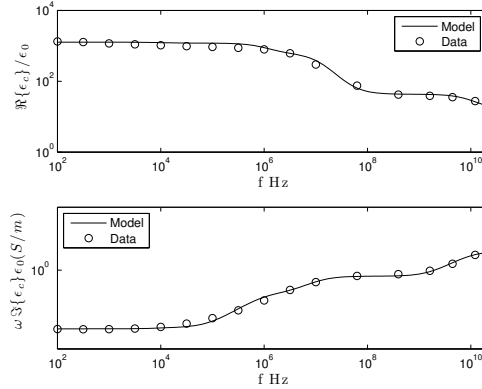
Figure 1: Rocard-Powles-Debye model fit (solid curve) to the empirical data (circles) for dry skin.

2.2 Fat

The best-fit Rocard-Powles-Debyle model for fat is composed of seven relaxation modes ($N = 7$). The higher number of terms that are required to describe the frequency dispersion of this biological medium is due to the relatively small value of the Debye relaxation time combined with several faster relaxation times exhibited in the data. The high frequency permittivity for fat was found

to be $\epsilon_\infty = 3$ and the static conductivity to be $\sigma_0 = 1 \times 10^{-3} S/m$; the remaining model parameters are given in Table 2. The frequency dispersion model for fat is illustrated in Fig. 2.

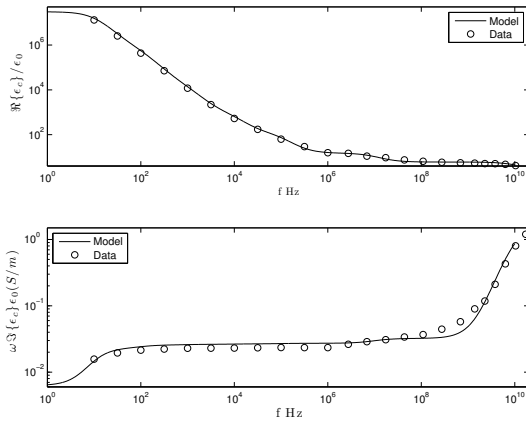| j	a_j	τ_j (sec)	τ_{fj} (sec)
1	3×10^7	1×10^{-1}	1×10^{-15}
2	5×10^5	1×10^{-2}	1×10^{-10}
3	1×10^4	1×10^{-3}	1×10^{-10}
4	7×10^2	1×10^{-4}	1×10^{-20}
5	100	1×10^{-5}	1×10^{-15}
6	9	1×10^{-7}	1×10^{-15}
7	3	1×10^{-10}	1×10^{-15}

Table 2: Model parameters for fat.

Figure 2: Rocard-Powles-Debye model fit (solid curve) to the empirical data (circles) for fat.

2.3 Muscle

The best-fit Rocard-Powles-Debyle model for muscle is composed of four relaxation modes ($N = 4$). The high frequency permittivity for fat was found to be $\epsilon_\infty = 28.3$ and the static conductivity to be $\sigma_0 = 3 \times 10^{-2} S/m$; the remaining model parameters are described in Table 3. The frequency dispersion model for muscle is illustrated in Fig. 3.

j	a_j	τ_j (sec)	τ_{fj} (sec)
1	2.05×10^7	6×10^{-3}	1×10^{-15}
2	1.5×10^4	9×10^{-6}	1×10^{-10}
3	7×10^3	1.5×10^{-6}	1×10^{-10}
4	45	1×10^{-10}	1×10^{-20}

Table 3: Model parameters for muscle transverse to fibers.
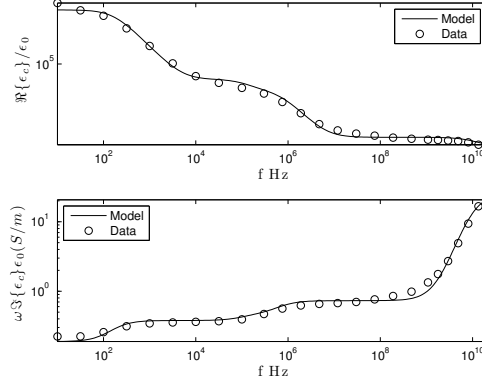
Figure 3: Rocard-Powles-Debye model fit (solid curve) to the empirical data (circles) for muscle transverse to fibers.

3 SCATTERING

The transfer matrix method [9] is used here for the description of reflection from and transmission through a system of stacked layers. It has been shown that this approach is equivalent to the Fresnel formulation leading to the Airy formula but is less cumbersome to deal with when there is more than one sandwiched layer [10].

The analysis begins with the electromagnetic boundary conditions for the tangential components of the fields, given by

$$\hat{\mathbf{n}} \times \left(\tilde{\mathbf{E}}_{j+1}(\mathbf{r}, \omega) - \tilde{\mathbf{E}}_j(\mathbf{r}, \omega) \right) = 0, \qquad (4)$$

$$\hat{\mathbf{n}} \times \left(\tilde{\mathbf{H}}_{j+1}(\mathbf{r}, \omega) - \tilde{\mathbf{H}}_j(\mathbf{r}, \omega) \right) = \tilde{\mathbf{J}}_s(\mathbf{r}, \omega), \qquad (5)$$

across a planar interface with unit normal vector $\hat{\mathbf{n}}$ directed from the incident to the transmitted medium and unit tangential vector $\hat{\nu}$ to the interface. The coupled equations for the electric field vectors are then given by

$$\left(\tilde{\mathbf{E}}_j + \tilde{\mathbf{E}}'_j \right) \cdot \hat{\nu} = \left(\tilde{\mathbf{E}}_{j+1} + \tilde{\mathbf{E}}'_{j+1} \right) \cdot \hat{\nu} \qquad (6)$$

$$\left(\tilde{\mathbf{E}}_j - \tilde{\mathbf{E}}'_j \right) \cdot \hat{\nu} n_j = \left(\tilde{\mathbf{E}}_{j+1} - \tilde{\mathbf{E}}'_{j+1} \right) \cdot \hat{\nu} n_{j+1} + \tilde{\mathbf{J}}_s \quad (7)$$

where $\tilde{\mathbf{E}}_j$ and $\tilde{\mathbf{E}}'_j$ denote the right and left moving waves in the jth layer, respectively. The surface current density is confined to a transition layer of thickness Δl which spans each interface and extends an equal distance into each medium. Over this transition layer the frequency dependent conductivity is varied with some interpolating function in order to continuously connect the layers.

These boundary conditions can be compactly represented in a dynamical matrix as

$$\mathbf{D}_j = \begin{pmatrix} 1 & 1 \\ \sigma_{eff} + n_j & \sigma_{eff} - n_j \end{pmatrix}, \qquad (8)$$

multiplied by the vector $\left[\tilde{\mathbf{E}}_j \ \tilde{\mathbf{E}}'_j \right]^T$ for each layer such that

$$\mathbf{D}_j \begin{bmatrix} \tilde{\mathbf{E}}_j \\ \tilde{\mathbf{E}}'_j \end{bmatrix} = \mathbf{D}_{j+1} \begin{bmatrix} \tilde{\mathbf{E}}_{j+1} \\ \tilde{\mathbf{E}}'_{j+1} \end{bmatrix}. \qquad (9)$$

In addition, a propagation matrix, $\mathbf{P}_j$, is defined for each layer of finite thickness Δz_j as

$$\mathbf{P}_j = \begin{pmatrix} e^{i\Delta z_j \tilde{\mathbf{k}}_j(\omega)} & 0 \\ 0 & e^{-i\Delta z_j \tilde{\mathbf{k}}_j(\omega)} \end{pmatrix}. \qquad (10)$$

The transfer matrix, $\mathbf{M}$, for the whole system is then given by,

$$\mathbf{M} = \mathbf{D}_0^{-1} \left[\prod_{j=1}^{N-1} \mathbf{D}_j \mathbf{P}_j \mathbf{D}_j^{-1} \right] \mathbf{D}_N, \qquad (11)$$

where $\mathbf{D}_0$ is taken to be free space and $\mathbf{D}_N$ is the substrate material, in this case muscle, and will have no left moving wave. This transfer matrix also provides the Fresnel reflection and transmission coefficients as $r = \frac{m_{21}}{m_{11}}$ and $t = \frac{1}{m_{11}}$, respectively, whose frequency dependence is illustrated in Fig. 4.
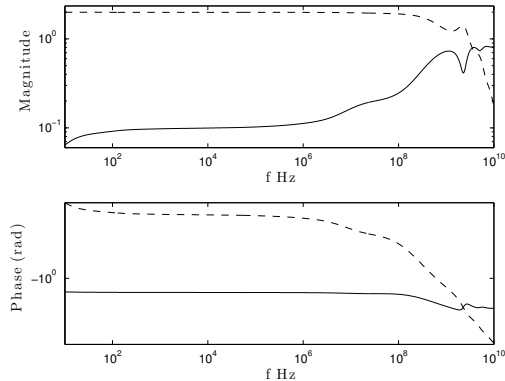
Figure 4: Magnitude (upper) and phase (lower) of the complex Fresnel reflection (solid) and transmission (dashed) coefficients.

4   CONCLUSION

This formalism provides the necessary theoretical description required to properly analyze interaction of an ultrawidebound electromagnetic pulse with a layered, lossy, dispersive biological system.

References

[1] R. Adair, "Biophysical limits on athermal effects of rf and microwave radiation," *Bioelectromagnetics*, vol. 24, no. 1, pp. 39–48, 2003.

[2] K. Cole, "Ions, potentials and the nerve impulse. in" electrochemistry in biology and medicine"(t. shedlovsky, ed.)," 1955.

[3] F. Barnes, *An Assessment of Potential Health Effects from Exposure to PAVE PAWS Low-level Phased-array Radiofrequency Energy.* National Academies Press, 2005.

[4] N. Volkow, D. Tomasi, G. Wang, P. Vaska, J. Fowler, F. Telang, D. Alexoff, J. Logan, and C. Wong, "Effects of cell phone radiofrequency signal exposure on brain glucose metabolism," *JAMA: The Journal of the American Medical Association*, vol. 305, no. 8, p. 808, 2011.

[5] J. Roy, "New results for the effective propagation constants of nonuniform plane waves at the planar interface of two lossy media," *Antennas and Propagation, IEEE Transactions on*, vol. 51, no. 6, pp. 1206–1215, 2003.

[6] K. Oughstun, "Dynamical evolution of the Brillouin precursor in Rocard-Powles-Debye model dielectrics," *Antennas and Propagation, IEEE Transactions on*, vol. 53, no. 5, pp. 1582–1590, 2005.

[7] S. Gabriel, R. Lau, and C. Gabriel, "The dielectric properties of biological tissues: Ii. measurements in the frequency range 10 hz to 20 ghz," *Physics in Medicine and Biology*, vol. 41, p. 2251, 1996.

[8] K. Oughstun, *Electromagnetic and Optical Pulse Propagation 1: Temporal Pulse Dynamics in Dispersive, Attenuative Media.* Springer, 2006.

[9] P. Yeh, *Optical waves in layered media.* Wiley Online Library, 1988.

[10] P. Pereyra and A. Robledo-Martinez, "On the equivalence of the summation and transfer-matrix methods in wave propagation through multilayers of lossless and lossy media," *European Journal of Physics*, vol. 30, p. 393, 2009.

Appendix B

Precursor Fields Reflected From Low Observables

The included abstract has been accepted at the 2012 IEEE International Symposium on Antennas and Propagation and USNC-URSI National Radio Science Meeting and is based on a combination of work presented here in Chapters 2 and 3.

Precursor Fields Reflected From Low Observables

Chris L. Palombini and Kurt E. Oughstun*
The University of Vermont, Burlington, VT, 05405,
http://www.uvm.edu

The effects of material dispersion on the reflected electromagnetic wavefield due to an incident ultrawideband pulse on a multilayer dielectric stack is presented for the particular case when the system contains a single layer of finite thickness Δz placed on top of a perfect electric conductor (PEC). The nonmagnetic ($\mu = \mu_0$), nonconducting ($\sigma = 0$) dielectric layer is assumed to be highly absorptive and dispersive as might be found in a radar absorbing material (RAM) with complex permittivity $\epsilon(\omega)$ and complex refractive index $n(\omega) = (\epsilon(\omega)/\epsilon_0)^{1/2} = n_r(\omega)+\imath n_i(\omega)$ described by the Rocard-Powles extension of the Debye model of orientational polarization. The hypothetical radar absorbing material is designed to have an e^{-1} absorption depth $z_d \equiv c/(\omega_c n_i(\omega_c))$ equal to a wavelength $\lambda = (2\pi c)/(\omega n_r(\omega))$ at the carrier frequency $\omega_c = 2\pi f_c$, and the thickness of the layer Δz is nominally chosen at a quarter wavelength at the carrier frequency and varied up to a wavelength, where the incident and reflected pulses are in vacuum. Examples are presented for an incident rectangular enveloped pulse of time duration T that is chosen to be either ultrashort (a single cycle) or long (many cycles) in order to investigate the effects of destructive interference on the reflected steady-state component. The reflected signal is shown to contain multiple pulses from the repeated reflections inside the dielectric layer with the multiple reflected pulses connected in time since the layer's thickness is on the order of or less than a wavelength. The Brillouin precursor is known to dominate the signal as $2\Delta z$ increases above z_d and can be used to detect the low observable surface.

Appendix C

Derivation of Fresnel Coefficients for Lossy Materials

This analysis follows from (Canning 2011) and allows for the plane wave to be inhomogeneous. Starting with the boundary conditions for TM-polarization

$$\hat{\mathbf{n}} \times \left(\tilde{\mathbf{H}}_2 + \tilde{\mathbf{H}}_0 \right) = \hat{\mathbf{n}} \times \tilde{\mathbf{H}}_0, \tag{C.1}$$

$$\hat{\mathbf{n}} \cdot \left(\tilde{\mathbf{E}}_1 - (\tilde{\mathbf{E}}_0 + \tilde{\mathbf{E}}_2) \right) = \rho_s, \tag{C.2}$$

where $\tilde{\mathbf{E}}_0$ and $\tilde{\mathbf{H}}_0$ are the incident field vectors, $\tilde{\mathbf{E}}_2$ and $\tilde{\mathbf{H}}_2$ are the reflected electric field vectors, $\tilde{\mathbf{E}}_1$ and $\tilde{\mathbf{H}}_1$ are the electric field vectors, and $\hat{\mathbf{n}}$ is the unit normal vector directed from the incident to transmitted media. Again, these two boundary conditions respectively state that the tangential component of the magnetic field vector is continuous across an interface and that the normal component of the electric field vector is discontinuous across an interface with that discontinuity being proportional to any surface charge density ρ_s. The electric and magnetic field vectors are related through the complex impedance as

$$\tilde{\mathbf{H}} = \frac{\tilde{\mathbf{k}}}{\omega\mu} \hat{\mathbf{n}} \times \tilde{\mathbf{E}}, \tag{C.3}$$

where $\tilde{\mathbf{k}}$ is the complex wavenumber in that medium.

Using Eq. (C.3) the boundary condition in Eq. (C.2) may be re-written as

$$\hat{\mathbf{n}} \times \left(\hat{\mathbf{n}}_0 \times \tilde{\mathbf{E}}_0 + \hat{\mathbf{n}}_2 \times \tilde{\mathbf{E}}_2 \right) = \hat{\mathbf{n}} \times (\tilde{\mathbf{k}}_1 \times \tilde{\mathbf{E}}_1) \frac{1}{\mu_1}, \tag{C.4}$$

where $\hat{\mathbf{n}}_2$ is the unit normal in the direction of the reflected wave that is $\hat{\mathbf{n}}_2 = -\hat{\mathbf{n}}$. By application of the vector triple product

$$\mathbf{a} \times (\mathbf{b} \times \mathbf{c}) = (\mathbf{a} \cdot \mathbf{c})\mathbf{b} - (\mathbf{a} \cdot \mathbf{b})\mathbf{c}, \tag{C.5}$$

one gets the relations

$$\hat{\mathbf{n}} \cdot \tilde{\mathbf{E}}_i = \tilde{\mathbf{k}}_1 \cdot \tilde{\mathbf{E}}_1 = 0, \text{ for } i = 1, 2, 3, \tag{C.6}$$

and

$$\hat{\mathbf{n}}_0 \cdot \tilde{\mathbf{E}}_0 = \hat{\mathbf{n}}_2 \cdot \tilde{\mathbf{E}}_2 = 0. \tag{C.7}$$

Now Eq. (C.4) can be simplified to

$$\hat{\mathbf{n}} \times (\tilde{\mathbf{k}}_1 \times \tilde{\mathbf{E}}_1) \frac{1}{\mu_1} = \left[(\hat{\mathbf{n}} \cdot \tilde{\mathbf{E}}_1)\tilde{\mathbf{k}}_1 - (\hat{\mathbf{n}} \cdot \tilde{\mathbf{k}}_1)\tilde{\mathbf{E}}_1 \right] \frac{1}{\mu_1}. \tag{C.8}$$

It is at this point the significance of the lossy media is revealed the wavenumber $\tilde{\mathbf{k}}$ consists of two components and, in general, these components are in different directions as

$$\tilde{\mathbf{k}} = \Re\{\tilde{\mathbf{k}}\}\hat{\mathbf{n}}_1 + i\Im\{\tilde{\mathbf{k}}\}\hat{\mathbf{n}}. \tag{C.9}$$

It is now obvious how in a lossy medium the planes of constant phase and the planes of constant amplitude are in different directions, with the planes of constant amplitude always normal to the interface. Through the application of these relations the boundary condition becomes

$$\hat{\mathbf{n}} \times (\tilde{\mathbf{k}}_1 \times \tilde{\mathbf{E}}_1) \frac{1}{\mu_1} = - \left[\Re\{\tilde{\mathbf{k}}_1\} \cos\theta_1 + i\Im\{\tilde{\mathbf{k}}_1\} \right] \frac{\tilde{\mathbf{E}}_1}{\mu_1}, \tag{C.10}$$

where θ_1 is the deviation of the transmitted wave from $\hat{\mathbf{n}}$. This is reduced further by noting that $(\hat{\mathbf{n}} \cdot \hat{\mathbf{n}}_0) = \cos\theta_0$ to

$$\cos\theta_0(\tilde{\mathbf{E}}_0 - \tilde{\mathbf{E}}_2) = \frac{\mu_0}{\mu_1 \tilde{\mathbf{k}}_0} \left[\Re\{\tilde{\mathbf{k}}_1\} \cos\theta_1 + i\Im\{\tilde{\mathbf{k}}_1\} \right] \tilde{\mathbf{E}}_1, \tag{C.11}$$

114

which is the correct form of the relationship [(Stratton 1941) pg. 492 Eq. (13)]. In the absence of any surface charge $\rho_s = 0$ the second boundary condition is

$$\tilde{\mathbf{E}}_0 + \tilde{\mathbf{E}}_2 = \tilde{\mathbf{E}}_1. \tag{C.12}$$

By simultaneously solving Eqs. (C.11)–(C.12) with the substitution of Eq. (C.12) into Eq. (C.11) provides

$$\frac{\mu_1 \tilde{\mathbf{k}}_0 \cos\theta_0 - \mu_0 \left[\Re\{\tilde{\mathbf{k}}_1\} \cos\theta_1 + \imath\Im\{\tilde{\mathbf{k}}_1\}\right]}{\mu_1 \tilde{\mathbf{k}}_0 \cos\theta_0 + \mu_0 \left[\Re\{\tilde{\mathbf{k}}_1\} \cos\theta_1 + \imath\Im\{\tilde{\mathbf{k}}_1\}\right]} = \frac{\tilde{\mathbf{E}}_2}{\tilde{\mathbf{E}}_0}, \tag{C.13}$$

showing that the left hand side of the equation is the Fresnel reflection coefficient for lossy media. Similar analysis follows to determine the Fresnel transmission coefficient by substituting $\tilde{\mathbf{E}}_1 - \tilde{\mathbf{E}}_0 = \tilde{\mathbf{E}}_2$ into Eq. (C.11) which provides

$$\frac{2\mu_1 \tilde{\mathbf{k}}_0 \cos\theta_0}{\mu_1 \tilde{\mathbf{k}}_0 \cos\theta_0 + \mu_0 \left[\Re\{\tilde{\mathbf{k}}_1\} \cos\theta_1 + \imath\Im\{\tilde{\mathbf{k}}_1\}\right]} = \frac{\tilde{\mathbf{E}}_1}{\tilde{\mathbf{E}}_0}, \tag{C.14}$$

where the left hand side is the Fresnel transmission coefficient for lossy media.

Appendix D

Microscopic Potentials and Radiation

D.1 The Hertz Potential

Under the Lorenz condition

$$\nabla \cdot \mathbf{a} + \epsilon_0 \mu_0 \frac{\partial}{\partial t} \phi = 0 \tag{D.1}$$

the vector and scalar potential fields can be expressed as

$$\nabla^2 \mathbf{a} - \frac{1}{c^2} \frac{\partial}{\partial t} \mathbf{a} = -\mu_0 \mathbf{j}, \tag{D.2}$$

$$\nabla^2 \phi - \frac{1}{c^2} \frac{\partial}{\partial t} \phi = -\frac{\rho}{\epsilon_0}, \tag{D.3}$$

where the microscopic current $\mathbf{j}$ and charge ρ densities satisfy the continuity equation

$$\nabla \cdot \mathbf{j} + \frac{\partial}{\partial t} \rho = 0. \tag{D.4}$$

It immediately follows that there exists a vector function $\mathbf{p}(\mathbf{r}, t)$ such that

$$\mathbf{j}(\mathbf{r}, t) = \frac{\partial}{\partial t} \mathbf{p}(\mathbf{r}, t), \tag{D.5}$$

$$\rho(\mathbf{r}, t) = -\nabla \cdot \mathbf{p}(\mathbf{r}, t), \tag{D.6}$$

in which case the continuity equation above is identically satisfied. The vector field represented by $\mathbf{p}(\mathbf{r}, t)$ is called the *electric moment*. The pair of wave equations shown in eq. (D.2)-(D.3) can then be expressed in terms of $\mathbf{p}(\mathbf{r}, t)$ as

$$\nabla^2 \mathbf{a} - \frac{1}{c^2} \frac{\partial}{\partial t} \mathbf{a} = -\mu_0 \frac{\partial}{\partial t} \mathbf{p}(\mathbf{r}, t), \tag{D.7}$$

$$\nabla^2 \phi - \frac{1}{c^2} \frac{\partial}{\partial t} \phi = -\frac{1}{\epsilon_0} \nabla \cdot \mathbf{p}(\mathbf{r}, t). \tag{D.8}$$

Assume now that the vector and scalar potentials are given by the respective relations

$$\mathbf{a}(\mathbf{r}, t) = \mu_0 \frac{\partial}{\partial t} \mathbf{\Pi}(\mathbf{r}, t), \tag{D.9}$$

$$\phi(\mathbf{r}, t) = -\frac{1}{\epsilon_0} \nabla \cdot \mathbf{\Pi}(\mathbf{r}, t), \tag{D.10}$$

which clearly satisfy the Lorenz condition eq. (D.1). The inhomogeneous wave equations shown in eq. (D.7)-(D.8) can be expressed in terms of the vector field $\mathbf{\Pi}(\mathbf{r}, t)$ as,

$$\frac{\partial}{\partial t} \left[\nabla^2 \mathbf{\Pi} - \frac{1}{c^2} \frac{\partial^2}{\partial t^2} \mathbf{\Pi} + \mathbf{p} \right] = 0, \tag{D.11}$$

$$\nabla \cdot \left[\nabla^2 \mathbf{\Pi} - \frac{1}{c^2} \frac{\partial^2}{\partial t^2} \mathbf{\Pi} + \mathbf{p} \right] = 0, \tag{D.12}$$

which are obviously satisfied if

$$\nabla^2 \mathbf{\Pi} - \frac{1}{c^2} \frac{\partial^2}{\partial t^2} \mathbf{\Pi} = -\mathbf{p}. \tag{D.13}$$

The vector field $\mathbf{\Pi}(\mathbf{r}, t)$ is called the *Hertz vector* or *Hertz potential* (Hertz 1889) for the electromagnetic field.

This analysis demonstrates that the Hertz vector $\mathbf{\Pi}(\mathbf{r}, t)$ determines an electromagnetic field though its vector and scalar potential functions, but it does not show how a specific electromagnetic field can be represented by the vector function $\mathbf{\Pi}(\mathbf{r}, t)$. For this to be shown the uniqueness of the vector field $\mathbf{\Pi}(\mathbf{r}, t)$ for a unique set of scalar and vector potentials must be proven. Let the initial condition of the scalar potential be $\phi_0(\mathbf{r}) \equiv \phi(\mathbf{r}, 0)$ and let $\mathbf{\Pi}_0(\mathbf{r})$ be any vector field that is dependent purely on position and independent of time such that $\nabla \cdot \mathbf{\Pi}_0 = -\epsilon_0 \phi_0$. The time dependent vector field can be defined from the time

independent vector field as

$$\mathbf{\Pi}'(\mathbf{r}, t) \equiv \mathbf{\Pi}_0(\mathbf{r}) + \frac{1}{\mu_0} \int_0^t \mathbf{a}(\mathbf{r}, t') dt', \tag{D.14}$$

so that

$$\mathbf{a}(\mathbf{r}, t) = \mu_0 \frac{\partial}{\partial t} \mathbf{\Pi}'(\mathbf{r}, t) \tag{D.15}$$

and by differentiation of eq. (D.14), and

$$\nabla \cdot \mathbf{\Pi}'(\mathbf{r}, t) = \nabla \cdot \mathbf{\Pi}_0(\mathbf{r}) + \frac{1}{\mu_0} \int_0^t \nabla \cdot \mathbf{a}(\mathbf{r}, t') dt' \tag{D.16}$$

$$= -\epsilon_0 \phi_0(\mathbf{r}) - \epsilon_0 \int_0^t \frac{\partial}{\partial t} \phi(\mathbf{r}, t') dt' \tag{D.17}$$

$$= \epsilon_0 \phi(\mathbf{r}, t), \tag{D.18}$$

where the Lorenz condition in eq. (D.1) has been used. Through direct substitution from the pair of relations appearing in eq. (D.7)-(D.8) one obtains,

$$\frac{\partial}{\partial t} \left[\nabla^2 \mathbf{\Pi}' \frac{1}{c^2} \frac{\partial^2}{\partial t^2} \mathbf{\Pi}' \right] = -\frac{\partial}{\partial t} \mathbf{p}, \tag{D.19}$$

$$\nabla \cdot \left[\nabla^2 \mathbf{\Pi}' \frac{1}{c^2} \frac{\partial^2}{\partial t^2} \mathbf{\Pi}' \right] = -\nabla \cdot \mathbf{p}, \tag{D.20}$$

and consequently

$$\nabla^2 \mathbf{\Pi}' - \frac{1}{c^2} \frac{\partial^2}{\partial t^2} \mathbf{\Pi}' + \mathbf{p} = \nabla \times \mathbf{\Xi}, \tag{D.21}$$

where $\mathbf{\Xi}(\mathbf{r})$ is a vector function solely dependent on position $\mathbf{r}$ and independent of time t. By letting

$$\mathbf{\Pi}'(\mathbf{r}, t) = \mathbf{\Pi}(\mathbf{r}, t) + \nabla \times \mathbf{\Psi}(\mathbf{r}), \tag{D.22}$$

where $\mathbf{\Psi}(\mathbf{r})$ is another vector function solely dependent on position $\mathbf{r}$ and independent of time t and satisfies

$$\nabla^2 \mathbf{\Psi}(\mathbf{r}) = \mathbf{\Xi}(\mathbf{r}) \tag{D.23}$$

as required by eq. (D.21).It is now obvious that the vector function $\mathbf{\Pi}'(\mathbf{r}, t)$ satisfies eq. (D.13) and since

$$\nabla \cdot \mathbf{\Pi}'(\mathbf{r}, t) = \nabla \cdot \mathbf{\Pi}(\mathbf{r}, t), \tag{D.24}$$

$$\frac{\partial}{\partial t} \mathbf{\Pi}'(\mathbf{r}, t) = \frac{\partial}{\partial t} \mathbf{\Pi}(\mathbf{r}, t), \tag{D.25}$$

118

This has shown that for a given electromagnetic field one can always determine the vector $\mathbf{\Pi}(\mathbf{r}, t)$ such that

$$\mathbf{e}(\mathbf{r}, t) = \frac{1}{\epsilon_0} \nabla (\nabla \cdot \mathbf{\Pi}(\mathbf{r}, t)) - \mu_0 \frac{\partial^2}{\partial t^2} \mathbf{\Pi}(\mathbf{r}, t), \tag{D.26}$$

$$\mathbf{b}(\mathbf{r}, t) = \mu_0 \nabla \times \frac{\partial}{\partial t} \mathbf{\Pi}(\mathbf{r}, t), \tag{D.27}$$

where $\mathbf{\Pi}(\mathbf{r}, t)$ necessarily satisfies the inhomogeneous wave equation in eq. (D.13) and is the Hertz vector or Hertz potential for the microscopic electromagnetic field.

The Hertz potential $\mathbf{\Pi}(\mathbf{r}, t)$ is not uniquely defined because the vector and scalar potentials $\{\mathbf{a}(\mathbf{r}, t), \phi(\mathbf{r}, t)\}$ are invariant under the gauge transformation

$$\mathbf{\Pi}(\mathbf{r}, t) \rightarrow \mathbf{\Pi}'(\mathbf{r}, t) = \mathbf{\Pi}(\mathbf{r}, t) + \nabla \times \mathbf{\Gamma}(\mathbf{r}), \tag{D.28}$$

where $\mathbf{\Gamma}(\mathbf{r})$ is an arbitrary vector function of position that is independent of time t. To add to the level of arbitrariness is that fact that vector and scalar potentials themselves are not uniquely determined in the chosen Lorenz gauge because of the restricted gauge transformation. As a consequence of this the microscopic electromagnetic field vectors are invariant under the more general gauge transformation (Nisbet 1955)

$$\mathbf{\Pi}(\mathbf{r}, t) \rightarrow \mathbf{\Pi}'(\mathbf{r}, t) = \mathbf{\Pi}(\mathbf{r}, t) + \nabla \times \mathbf{\Gamma}(\mathbf{r}) - \frac{1}{c} \frac{\partial}{\partial t} \mathbf{\Lambda}(\mathbf{r}, t) - \nabla \lambda(\mathbf{r}, t), \tag{D.29}$$

where $\mathbf{\Gamma}(\mathbf{r}), \mathbf{\Lambda}(\mathbf{r}, t)$, and $\lambda(\mathbf{r}, t)$ are arbitrary functions. Under this transformation the vector and scalar potentials undergo the gauge transformation

$$\mathbf{a}(\mathbf{r}, t) \rightarrow \mathbf{a}'(\mathbf{r}, t) = \mathbf{a}(\mathbf{r}, t) - \frac{\mu_0}{c} \frac{\partial^2}{\partial t^2} \mathbf{\Lambda}(\mathbf{r}, t) - \mu_0 \nabla \frac{\partial}{\partial t} \lambda(\mathbf{r}, t), \tag{D.30}$$

$$\phi(\mathbf{r}, t) \rightarrow \phi'(\mathbf{r}, t) = \phi(\mathbf{r}, t) + \frac{1}{\epsilon_0 c} \nabla \cdot \frac{\partial^2}{\partial t^2} \mathbf{\Lambda}(\mathbf{r}, t) + \frac{1}{\epsilon_0} \nabla^2 \lambda(\mathbf{r}, t). \tag{D.31}$$

The Lorenz condition eq. (D.1) is satisified by the transformed pair of potentials $\{\mathbf{a}'(\mathbf{r}, t), \phi'(\mathbf{r}, t)\}$ if it is originally satisfied by the pair $\{\mathbf{a}(\mathbf{r}, t), \phi(\mathbf{r}, t)\}$, because

$$\nabla \cdot \mathbf{a}' \epsilon_0 \mu_0 \frac{\partial}{\partial t} \phi' = \nabla \mathbf{a} + \epsilon_0 \mu_0 \frac{\partial}{\partial t} \phi - \frac{\mu_0}{c} \left(\nabla \cdot \frac{\partial^2}{\partial t^2} \mathbf{\Lambda} - \frac{\partial^2}{\partial t^2} \nabla \cdot \mathbf{\Lambda} \right) - \mu_0 \left(\nabla^2 \frac{\partial}{\partial t} \lambda - \frac{\partial}{\partial t} \nabla^2 \lambda \right)$$

$$\tag{D.32}$$

$$= 0. \tag{D.33}$$

Comparison of this equation with the expressions given in eqs. (D.30)-(D.31) the gauge function $\psi(\mathbf{r}, t)$ is seen to satisfy the pair of relations

$$\nabla \psi = -\mu_0 \left(\frac{1}{c} \frac{\partial}{\partial t} \mathbf{\Lambda} + \nabla \frac{\partial}{\partial t} \lambda \right), \tag{D.34}$$

$$\frac{\partial}{\partial t} \psi = -\frac{1}{\epsilon_0} \left(\frac{1}{c} \nabla \cdot \frac{\partial}{\partial t} \mathbf{\Lambda} + \nabla^2 \lambda \right), \tag{D.35}$$

from which it is readily seen that $\psi(\mathbf{r}, t)$ satisfies the homogeneous wave equation.

The coupling among the electric and magnetic field vectors, the scalar and vector potentials, and the Hertz vector under these various gauge transformations within the Lorenz gauge is illustrated in Fig. D.1 taken from (Oughstun 2006a) pp. 123. Because the gauge transformation for the Hertz potential leaves the scalar and vector potentials in the Lorenz gauge, it then results in a restricted gauge transformation for the scalar and vector potentials (Oughstun 2006a).
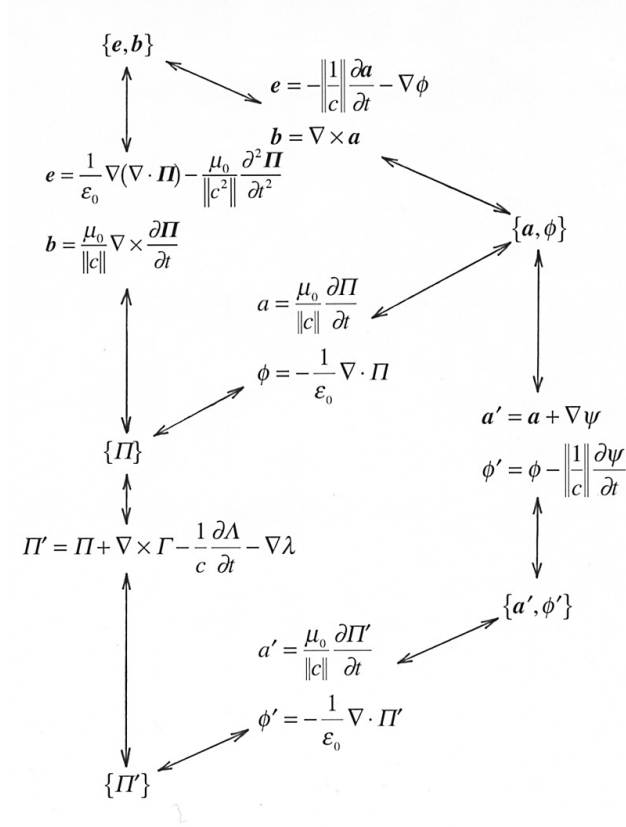
Figure D.1: Network structure between the Lorenz gauge and Hertz vector.

D.2   Radiation from an Elemental Hertzian Dipole

Consider the microscopic electromagnetic field produced by an elemental linear electric dipole situated at the fixed point $\mathbf{r} = \mathbf{r}_0$ and oscillating along a fixed direction specified by the unit vector $\hat{\mathbf{d}}$. Such an ideal point dipole is characterized by the electric moment

$$\mathbf{p}\,(\mathbf{r}, t) = p(t)\delta(\mathbf{r} - \mathbf{r}_0)\hat{\mathbf{d}}, \tag{D.36}$$

where $\delta(\mathbf{r})$ denotes the Dirack delta function. The particular solution of the inhomogeneous wave equation for the Hertz potential may be expressed in the form for the retarded potentials as

$$\mathbf{\Pi}\,(\mathbf{r}, t) = \frac{1}{4\pi} \int \frac{\mathbf{p}(\mathbf{r}', t - R/c)}{R} d^3 r', \tag{D.37}$$

so that, with the substitution from eq. (D.36), the Hertz vector for a point dipole is found as

$$\mathbf{\Pi}\,(\mathbf{r}, t) = \frac{1}{4\pi} p(t - R/c)\hat{\mathbf{d}}, \tag{D.38}$$

where $R = |\mathbf{r} - \mathbf{r}_0|$. The microscopic electric and magnetic field vectors are then given by eqs. (D.26)-(D.27) where

$$\nabla \cdot \left(\frac{1}{R} p(t - R/c)\hat{\mathbf{d}} \right) = p(t - R/c) \left(\nabla \frac{1}{R} \right) \cdot \hat{\mathbf{d}} + \frac{1}{R}(\nabla p(t - R/c)) \cdot \hat{\mathbf{d}} \tag{D.39}$$

$$= - \left(\frac{p(t - R/c)}{R^3} + \frac{1}{cR^2} \frac{\partial}{\partial t} p(t - R/c) \right) \left(\mathbf{R} \cdot \hat{\mathbf{d}} \right) \tag{D.40}$$

so that

$$4\pi \nabla(\nabla \cdot \mathbf{\Pi}) = \left\{ \frac{3}{R^5} p + \frac{3}{cR^4} \frac{\partial}{\partial t} p + \frac{1}{c^2 R^3} \frac{\partial^2}{\partial t^2} p \right\} (\hat{\mathbf{d}} \cdot \mathbf{R})\mathbf{R} - \left\{ \frac{1}{R^3} p + \frac{1}{cR^2} \frac{\partial}{\partial t} p \right\} \hat{\mathbf{d}}, \tag{D.41}$$

and

$$4\pi \nabla \times \mathbf{\Pi} = \left\{ \frac{1}{R^3} p + \frac{1}{cR^2} \frac{\partial}{\partial t} p \right\} (\hat{\mathbf{d}} \times \mathbf{R}), \tag{D.42}$$

where all the quantities on the right-hand side of the above equations are evaluated at the retarded time $t - R/c$. With these substitutions eqs. (D.26)-(D.27) become

$$\mathbf{e}\left(\mathbf{r}, t\right) = \frac{1}{4\pi\epsilon_0} \left\{ \frac{3}{R^5}p + \frac{3}{cR^4}\frac{\partial}{\partial t}p + \frac{1}{c^2 R^3}\frac{\partial^2}{\partial t^2}p \right\}(\hat{\mathbf{d}} \cdot \mathbf{R})\mathbf{R} - \frac{\mu_0}{4\pi c^2}\left\{ \frac{1}{R^3}p + \frac{1}{cR^2}\frac{\partial}{\partial t}p + \frac{1}{c^2 R \frac{\partial^2}{\partial t^2}p} \right\}\hat{\mathbf{d}}$$

(D.43)

$$\mathbf{b}\left(\mathbf{r}, t\right) = \frac{\mu_0}{4\pi} \left\{ \frac{1}{R^3}\frac{\partial}{\partial t}p + \frac{1}{cR^2}\frac{\partial^2}{\partial t^2}p \right\}(\hat{\mathbf{d}} \times R).$$

(D.44)

These are then the electromagnetic field vectors for an elemental Hertzian dipole, where $p = p(t - R/c)$ (Oughstun 2006a).

Bibliography

Adair, R. (2003). Biophysical limits on athermal effects of rf and microwave radiation. *Bioelectromagnetics 24*(1), 39–48.

Agrawal, G. (1989). *Nonlinear Fiber Optics*. Academic Press.

Albanese, R., J. Penn, and R. Medina (1993). Ultrashort pulse response in nonlinear dispersive media. *Ultra-Wideband, Short-Pulse Electromagnetics*, 259–264.

Barnes, F., e. a. (2005). An assessment of potential health effects from exposure to pave paws low-level phased-array radiofrequency energy. Technical report, National Academies.

Baum, C., L. Carin, and A. Stone (1997). *Ultra-Wideband, Short-Pulse Electromagnetics 3*. Plenum.

Bernstein, J. and A. Tschermak (1906). Untersuchungen zur thermodynamik der bioelektrischen ströme. *Pflügers Archiv European Journal of Physiology 112*(9), 439–521.

Bertoni, H., L. Carin, and L. Felsen (1993). *Ultra-Wideband, Short-Pulse Electromagnetics*. Plenum.

Bohren, C. and D. Huffman (1983). *Absorption and scattering of light by small particles*. Wiley.

Born, M. and E. Wolf (1980). *Principles of optics: electromagnetic theory of propagation, interference and diffraction of light* (6 ed.). Pergamon Press.

Brillouin, L. (1914). Uber die fortpflanzung des licht in disperdierenden medien. *Ann.Phys.(Leipzig) 44*(4), 177–202.

Brillouin, L. (1960). *Wave propagation and group velocity*, Volume 304. Academic Press New York.

Canning, F. (2011). Corrected fresnel coefficients for lossy materials. In *Antennas and Propagation (APSURSI), 2011 IEEE International Symposium on*, pp. 2123–2126. IEEE.

Cardis, E., I. Deltour, M. Vrijheid, E. Combalot, M. Moissonnier, H. Tardy, B. Armstrong, G. Giles, J. Brown, J. Siemiatycki, et al. (2010). Brain tumour risk in relation to mobile telephone use: results of the interphone international case-control study. *International Journal of Epidemiology 39*(3), 675–694.

Carin, L. and L. Felsen (1995). *Ultra-Wideband, Short-Pulse Electromagnetics 2*. Plenum.

Carpenter, D., C. Sage, et al. (2007). Bioinitiative report: a rationale for a biologically-based public exposure standard for electromagnetic fields (elf and rf).

Cartwright, N. and K. Oughstun (2007). Uniform asymptotics applied to ultrawideband pulse propagation. *Siam Review 49*(4), 628.

Chen, H. and H. Wang (1994). Current and sar induced in a human head model by the electromagnetic fields irradiated from a cellular phone. *Microwave Theory and Techniques, IEEE Transactions on 42*(12), 2249–2254.

Cole, K. (1955). Ions, potentials and the nerve impulse. in" electrochemistry in biology and medicine"(t. shedlovsky, ed.).

Commission, F. C. et al. (2002). First report and order, revision of part 15 of commissions rule regarding ultra-wideband transmission system fcc 02-48. Technical report, FCC.

Curtis, H. and K. Cole (1940). Membrane action potentials from the squid giant axon. *Journal of Cellular and Comparative Physiology 15*(2), 147–157.

Debye, P. (1909). Naherungsformeln fur die zylinderfunktionen fur gross werte des arguments und unbeschrankt verander liche werte des index. *Math. Ann. 67*, 535–558.

Debye, P. (1929). *Polar molecules*. Dover.

Descartes, R. (1644). Principia philosophiae, amsterdam 1644. *Pt 2*, 57–59.

Fitzhugh, R. (1960). Thresholds and plateaus in the hodgkin-huxley nerve equations. *The Journal of general physiology 43*(5), 867.

Fitzhugh, R. (1961). Impulses and physiological states in theoretical models of nerve membrane. *Biophysical Journal 1*(6), 445–466.

Fitzhugh, R. (1969). Mathematical models of excitation and propagation in nerve. *Biological engineering 1*, 1–85.

Foster, K. (2000). Thermal and nonthermal mechanisms of interaction of radio-frequency energy with biological systems. *IEEE Trans. Plasma Sci. 28*(1).

Gabriel, S., R. Lau, and C. Gabriel (1996). The dielectric properties of biological tissues: Ii. measurements in the frequency range 10 hz to 20 ghz. *Physics in Medicine and Biology 41*, 2251.

Hardin, R. and F. Tappert (1973). Applications of the split-step fourier method to the numerical solution of nonlinear and variable coefficient wave equation. *Siam Rev. Chronicles 15*(2), 423.

Havelock, T. (1908). The propagation of groups of waves in dispersive media, with application to waves on water produced by a travelling disturbance. *Proceedings of the Royal Society of London. Series A 81*(549), 398.

Havelock, T. (1914). *The Propagation of Disturbances in Dispersive Media*. Cambridge Univ Press.

Hertz, H. (1889). Die kräfte electrischer schwingungen, behandelt nach der maxwell'schen theorie. *Annalen der Physik 272*(1), 1–22.

Heyman, E., B. Mandelbaum, and J. Shiloh (1999). *Ultra-Wideband, Short-Pulse Electromagnetics 4*. Plenum.

Hodgkin, A. and A. Huxley (1952a). The components of membrane conductance in the giant axon of loligo. *The Journal of physiology 116*(4), 473.

Hodgkin, A. and A. Huxley (1952b). Currents carried by sodium and potassium ions through the membrane of the giant axon of loligo. *The Journal of physiology 116*(4), 449.

Hodgkin, A. and A. Huxley (1952c). The dual effect of membrane potential on sodium conductance in the giant axon of loligo. *The Journal of physiology 116*(4), 497.

Hodgkin, A. and A. Huxley (1952d). A quantitative description of membrane current and its application to conduction and excitation in nerve. *The Journal of physiology 117*(4), 500.

Hodgkin, A., A. Huxley, and B. Katz (1952). Measurement of current-voltage relations in the membrane of the giant axon of loligo. *The Journal of physiology 116*(4), 424.

Hu, B. (1989). Kramers-kronig in two lines. *American Journal of Physics 57*, 821–821.

Jackson, J. (1999). *Classical Electrodynamics*. Wiley.

Keener, J. and J. Sneyd (1998). Mathematical physiology, interdisciplinary applied mathematics 8.

Kelvin, L. (1887). On the waves produced by a single impulse in water of any depth, or in a dispersive medium. *Roy. Soc. XLII*(80).

Kerker, M. (1969). *The scattering of light and other electromagnetic radiation*. Academic Press.

Kramers, H. A. (1927). La diffusion de la lumiere par les atomes. In *Atti Cong. Intern. Fisica*, Volume Bologna: Nicolo Zonichelli, pp. 545–557.

Kronig, R. L. (1926). On the theory of dispersion of x-rays. *J. Opt. Soc. Am. & Rev. Sci.*

Instrum. *12*(6), 547–557.

Laine, T. and A. Friberg (2000). Self-guided waves and exact solutions of the nonlinear helmholtz equation. *J. Opt. Soc. Am. B 17*(5), 751–757.

Lorentz, H. (1906). *Theory of Electrons and its Applications to the Phenomena of Light and Radiant Heat.* New York.

Maisch, D. (2010). *Setting Exposure Standards for Telecommunications Frequency Electromagnetic Radiation.* Ph. D. thesis, University of Wollongong.

Marmont, G. (1949). Studies on the axon membrane. i. a new method. *Journal of Cellular and Comparative Physiology 34*(3), 351–382.

Maxwell, J. (1873). *A treatise on electricity and magnetism.* Clarendon Press.

McConnel, J. (1980). *Rotational Brownian motion and dielectric theory.* Academic.

Mokole, E., M. Kragalott, and K. Gerlach (2003). *Ultra-Wideband, Short-Pulse Electromagnetics 6.* Kluwer/Plenum.

Nagumo, J., S. Arimoto, and S. Yoshizawa (1962). An active pulse transmission line simulating nerve axon. *Proceedings of the IRE 50*(10), 2061–2070.

Nisbet, A. (1955). Hertzian electromagnetic potentials and associated gauge transformations. *Proceedings of the Royal Society of London. Series A. Mathematical and Physical Sciences 231*(1185), 250.

Nussenzveig, H. (1972). *Causality and the Dispersion Relations.* Academic Press.

Oughstun, K. (1991). Pulse propagation in a linear, causally dispersive medium. *IEEE Proc. 79*(10), 1394–1420.

Oughstun, K. (2005). Dynamical evolution of the brillouin precursor in rocard-powles-debye model dielectrics. *Antennas and Propagation, IEEE Transactions on 53*(5), 1582–1590.

Oughstun, K. (2006a). *Electromagnetic and optical pulse propagation*, Volume 1. Springer Verlag.

Oughstun, K. (2006b). *Electromagnetic and optical pulse propagation*, Volume 1. Springer Verlag.

Oughstun, K. (2009a). *Electromagnetic and Optical Pulse Propagation 2: Temporal Pulse Dynamics in Dispersive, Attenuative Media*, Volume 2. Springer Verlag.

Oughstun, K. (2009b). *Electromagnetic and Optical Pulse Propagation 2: Temporal Pulse Dynamics in Dispersive, Attenuative Media*, Volume 2. Springer Verlag.

Oughstun, K. and C. Balictsis (1996). Gaussian pulse propagation in a dispersive, absorbing dielectric. *Physical review letters 77*(11), 2210–2213.

Oughstun, K. and G. Sherman (1988). Propagation of electromagnetic pulses in a linear dispersive medium with absorption (the lorentz medium). *JOSA B 5*(4), 817–849.

Oughstun, K. and G. Sherman (1989). Uniform asymptotic describtion of electromagnetic pulse propagation in a linear dispersive medium with absorption (the lorenzt medium). *J. Opt. Soc. Am. A 6*(9), 1394–1420.

Oughstun, K. and G. Sherman (1990). Uniform asymptotic description of ultrashort rectangular optical pulse propagation in a linear, casually dispersive medium. *Phys. Rev. A 41*(11), 6090–6113.

Oughstun, K. and G. Sherman (1994). *Electromagnetic pulse propagation in causal dielectrics*. Springer-Verlag.

Oughstun, K. and H. Xiao (1997). Failure of the quasimonochromatic approximation for ultrashort pulse propagation in a dispersive, attenuative medium. *Phys. Rev. Letter 78*(4), 642–645.

Palombini, C. and K. Oughstun (2011). Reflection and transmission of pulsed electromagnetic fields through multilayered biological media. In *Electromagnetics in Advanced Applications (ICEAA), 2011 International Conference on*, pp. 283–286. IEEE.

Pereyra, P. and A. Robledo-Martinez (2009). On the equivalence of the summation and transfer-matrix methods in wave propagation through multilayers of lossless and lossy media. *European Journal of Physics 30*, 393.

Plemelj, J. (1908). Ein erganzungssatz zur cauchyschen integraldarstellung analytischer funktionen, randwerte betreffend, monatsh. f. *Math. u. Phys 19*, 205–210.

Powles, J. (1948). x. *Trans. Faraday. Soc. 44*, 802–806.

Rocard, M. (1933). x. *J. Phys. Radium. 4*, 247–250.

Röntgen, W. (1895). Uber eine neue art von strahlen. *Sitzungs-Berichte Phys.-med. Gesellschaft 9*, 132–141.

Roy, J. (2003). New results for the effective propagation constants of nonuniform plane waves at the planar interface of two lossy media. *Antennas and Propagation, IEEE Transactions on 51*(6), 1206–1215.

Salisbury, W. W. (1952). Absorpent body for electromagnetic waves. US Patent 2599944.

Slesin, L. (2002a, May/June). Brillouin precursors: Robert adair, albanese and oughstun. *Microwave News 22*(3), 13–14.

Slesin, L. (2002b, Jul./Aug.). Ieee says no to brillouin precursors. *Microwave News 22*(4), 16.

Slesin, L. (2002c, Mar/Apr). Introducing brillouin precursors: Microwave radiation runs deep. *Microwave News 22*(2), 10–12.

Smith, P. and S. Cloude (2002). *Ultra-Wideband, Short-Pulse Electromagnetics 5*. Kluwer/Plenum.

Sommerfeld, A. (1914). Uber die fortpflanzung des licht in disperdierenden medien. *Ann.Phys.(Leipzig) 44*(4), 177–202.

Stratton, J. (1941). *Electromagnetic theory*. McGraw-Hill.

Taylor, C. and D. Giri (1994). *High-power microwave systems and effects*. Taylor & Francis.

Titchmarsh, E. (1939). *Introduction to the theory of Fourier integrals*. London: Oxford University Press.

Toll, J. (1956). Causality and the dispersion relation: Logical foundations. *Phys. Rev. 104*(6), 1760–1770.

Volkow, N., D. Tomasi, G. Wang, P. Vaska, J. Fowler, F. Telang, D. Alexoff, J. Logan, and C. Wong (2011). Effects of cell phone radiofrequency signal exposure on brain glucose metabolism. *JAMA: The Journal of the American Medical Association 305*(8), 808.

Xiao, H. and K. Oughstun (1999). Failure of the group velocity description for ultrawideband pulse propagation in a double resonance lorentz model dielectric. *J. Opt. Soc. Am. B 16*(10), 1773–1785.

Yeh, P. (1988). *Optical waves in layered media*. Wiley.